LOW TEMPERATURE PHOTOLUMINESCENCE STUDY ON DEFECT CENTERS IN SILICON CARBIDE

by

Fei Yan

B.S. in Physics, Nanjing University, 2002

M.S. in Physics, University of Pittsburgh, 2004

Submitted to the Graduate Faculty of

Arts and Sciences in partial fulfillment

of the requirements for the degree of

Doctor of Philosophy

University of Pittsburgh

2009

UNIVERSITY OF PITTSBURGH

FACULTY OF ARTS AND SCIENCES

This dissertation was presented

by

Fei Yan

It was defended on

December 4, 2009

and approved by

Prof. W. J. Choyke, PhD, Dept. of Physics and Astronomy, University of Pittsburgh

Prof. R. P. Devaty, PhD, Dept. of Physics and Astronomy, University of Pittsburgh

Prof. X. L. Wu, PhD, Dept. of Physics and Astronomy, University of Pittsburgh

Prof. R. D. Coalson, PhD, Dept. of Physics and Astronomy, University of Pittsburgh

Prof. R. M. Feenstra, PhD, Department of Physics, Carnegie Mellon University

Dissertation Advisor: Prof. W. J. Choyke, PhD, Dept. of Physics and Astronomy

LOW TEMPERATURE PHOTOLUMINESCENCE STUDY ON DEFECT CENTERS IN SILICON CARBIDE

Fei Yan, PhD

University of Pittsburgh, 2009

This thesis reports the study of several intrinsic defect centers in SiC, mainly by optical characterization techniques. Different defect centers were created by either electron irradiation or ion implantation into n-type and p-type doped SiC following by annealing at different temperatures. Low temperature photoluminescence (LTPL) was used to study the optical properties of these defect centers. The no phonon lines from the dicarbon antisite defect center were observed with their phonon replicas. The stretch frequencies of the dicarbon dumbbell model are observed up to the fifth harmonic. The Morse Potential model was found to explain the anharmonicity quite well. First principles calculations were carried out by our collaborator Dr. A. Gali and show excellent agreement with the experiment and the Morse Potential results. It is clear that the dicarbon antisite defect is indeed responsible for the LTPL spectra. We also studied the evolution of the D_I deep defect centers at different annealing stages and attempted to find correlations between the D_I center in LTPL and the Z_1/Z_2 center at $E_C - 0.68$ eV or the HS1 center at $E_V + 0.35$ eV in deep level transient spectroscopy (DLTS). Our results indicate that in n-type 4H SiC there is no correlation between the Z_1/Z_2 center in DLTS and the L_1 peak of the D_I center seen in LTPL. In p-type 4H SiC we do not find a correlation between the HS1 DLTS peak and the LTPL L_1 peak of the D_I center. Consequently, we cannot find evidence for a 343 meV ground state postulated in the pseudodonor model.

TABLE OF CONTENTS

LIST OF TABLES

LIST OF FIGURES

PREFACE

I would like to thank Prof. W. J. Choyke for his guidance and support throughout my Ph.D. career. I also wish to thank Prof. R. P. Devaty for the fruitful discussions on my research. I wish to thank Prof. R. M. Feenstra, Prof. X. L. Wu and Prof. R. Coalson for serving on my Ph.D. committee.

I wish to thank Dr. S. Bai for his patient training on the optical characterization techniques. I also wish to thank Dr. Y. Shishkin and Dr. Y. Ke for their valuable help in the lab.

Special thanks go to C. Weisdack in the stockroom, K. Petrocelly and K. Kotek in the machine shop. Their generous help made my life much easier.

Last but not the least, I wish to thank my family for their love, support and encouragement. I wish I could share this moment with every one of them.

1.0 INTRODUCTION

1.1 BACKGROUND AND MOTIVATION

As a wide bandgap semiconductor, SiC has attracted a lot of research interest in the recent decades. It has high electron mobility, high breakdown electric field and high thermal conductivity. All these make it suitable for electronic use under high temperature, high frequency and high power conditions. A summary of some of the optical and electrical properties of SiC in comparison to Si and GaAs is shown in Table 1.1. Si and GaAs are picked for the comparison purpose because they are widely used in the modern semiconductor industry. SiC has a much wider bandgap than Si and GaAs, therefore it can operate at high temperatures before the intrinsic conduction effects have to be considered. The breakdown field of SiC is one order of magnitude greater than that of Si and GaAs. All these properties make SiC a suitable material for fabricating high voltage, high power devices, such as diodes, power transistors, high power microwave devices, and so on. These devices can also be packed close together for integrated circuits. The thermal conductivity of SiC is much greater than that of Si and GaAs. Actually it is comparable to metals, such as copper. This high thermal conductivity enables SiC devices to dissipate the large amount of heat generated in the high power devices. It also reduces the extra need for cooling inside the electronics, which could save space for integrated circuits and reduce the weight. The high saturated drift velocity of SiC is ideal for fabricating high frequency (RF

and microwave) devices. Besides these properties, the Si-C bond in SiC is quite strong, which makes it resistant to chemical attack and radiation. Therefore SiC devices are suitable for working under very harsh conditions. SiC is also a very good substrate for GaN crystal growth and GaN has been used to make LEDs to save the world's energy.

Table 1.1 Comparison of the electronic and physical properties of SiC, Si and GaAs [1].

	4H SiC	6H SiC	Si	GaAs
Bandgap Energy (eV)	3.26	3.03	1.12	1.43
Breakdown Field (V/cm)	$3x10^6$	$3x10^6$	$2.5x10^5$	$3.0x10^5$
Thermal Conductivity at Room Temperature (W/cm·K)	4.0	4.0	1.5	0.5
Saturated Drift Velocity (cm/s)	$2.0x10^7$	$2.0x10^7$	$1.0x10^7$	$1.0x10^7$

The many advantages of SiC semiconductor technology have been known for quite some time, but large single-crystal SiC boule growth has historically been a very difficult and expensive process due to SiC's physical properties (high melting point, hardness, polytypism, etc.). SiC wafer production has improved greatly in recent years, which gives us a chance to study some of the properties which were unable to be characterized in the old days due to the limitation of the material quality. Thanks to our collaborators who can grow high quality epitaxial thin films, we are able to study the deep level defects in SiC after electron irradiation and ion implantation.

1.2 CRYSTAL STRUCTURE OF SILICON CARBIDE

SiC is known as a wide bandgap semiconductor existing in over 170 crystallographic structures. These different crystallographic structures are called polytypes. Polytypism is one of the most unique features in SiC, which influences the properties of SiC.

The simplest way to understand the structure of the polytypes of SiC is to consider the close-packing of spheres. Figure 1.1 shows an array of white spheres in a single plane packed together in the closest possible configuration. Another layer of similarly arranged black spheres is added on top of the array of white spheres in a way that minimizes the volume taken up by the overall arrangement (the centers of the black spheres are aligned with the spaces in the white sphere packing pattern). When a third layer is added, there are two different stacking patterns which will both result in the overall arrangement occupying the least space possible. One choice, indicated by the location of the gray sphere on the left-hand side of Figure 1.1, is to place the spheres in the third layer directly above the spheres in the first layer. The first layer is labeled A, the second layer is labeled B, and, in this case, we also label the third layer A because its spheres are in the same locations as the spheres in the bottom layer. The other choice of sphere location for the third layer which equivalently minimizes the volume of the arrangement is indicated by the gray sphere on the right-hand side of Figure 1.1. Here, the spheres in the third layer are not aligned with the spheres in layer A, so we label this layer C. These two different packing structures, ABA and ABC, are referred to as hexagonal close-packed (HCP) and face-centered cubic (FCC), respectively.

These three possible layers, A, B, and C, can be arranged in many different ways. In SiC, we complicate matters because we actually have two different types of spheres - silicon atoms (whose atomic layers we label A, B, and C) and carbon atoms (whose atomic layers we label a,

b, and c). We restrict ourselves to discussion of the cases where the silicon and carbon layers are the same (e.g. AaBbCc or AaBbAa) and use only the labels A, B, and C to specify the packing sequence of both silicon and carbon atoms.

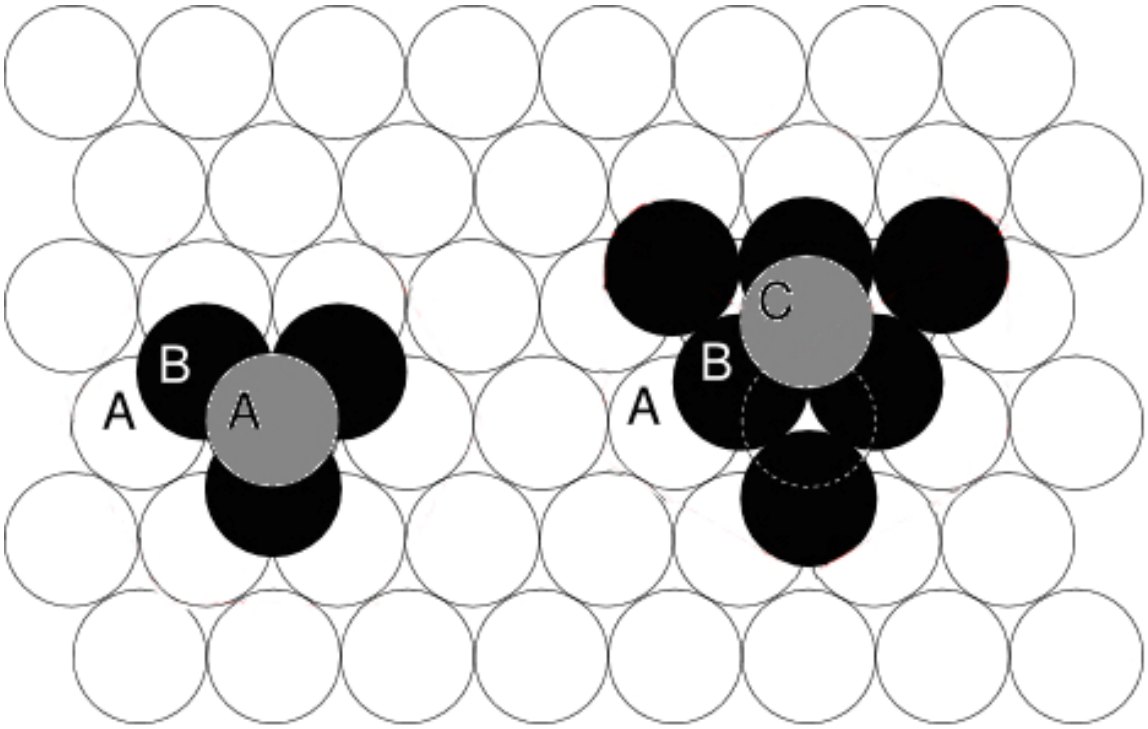

Figure 1.1 Example of packing spheres in the hexagonal close-packed (left) and face-centered cubic (right) configurations.

The common close-packed structures of SiC are typically identified using Ramsdell's notation, which involves specifying the number of layers in the unit cell followed by the letter H (hexagonal), R (rhombohedral), or C (cubic) to indicate the lattice type. 4H means there are four layers in a hexagonal unit cell, corresponding to a stacking sequence of ABAC. Similarly, 6H means there are six layers in a hexagonal unit cell, corresponding to a stacking sequence of ABCACB. 15R means there are fifteen layers in a rhombohedral unit cell, corresponding to a stacking sequence of ABCACBCABACABCB. These crystal structures of 3C, 4H and 6H SiC are shown graphically in Figure 1.2, along with real pictures taken from crystal structure models.

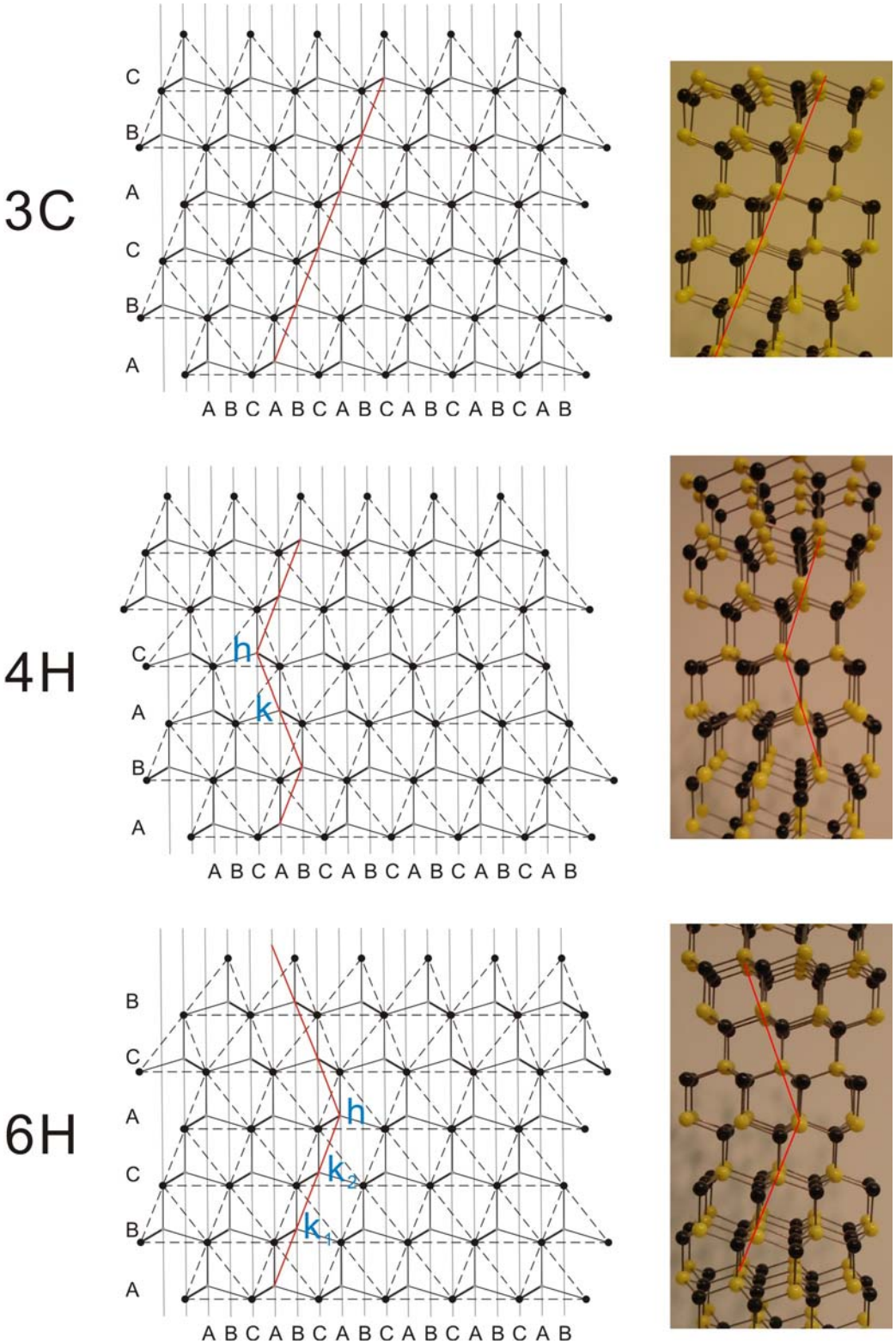

Figure 1.2 Schematic diagrams and pictures of real models of the different stacking sequences in the $(11\bar{2}0)$ plane for 3C, 4H, and 6H SiC. h and k denote the hexagonal and quasi-cubic inequivalent sites.

Figure 1.2 also illustrates one of the most important structural concepts for understanding the behavior of different polytypes of SiC - the inequivalent sites. Each individual lattice point in Figure 1.2, which is occupied by an atom, can be classified as either quasi-cubic (k) or hexagonal (h) by considering the positions of the neighboring layers surrounding it. If a lattice point is adjacent to two layers of different types (e.g. layer B surrounded by layers A and C), it is classified as quasi-cubic. If a lattice point is adjacent to two layers of the same type (e.g. layer B surrounded by A layers on both sides), it is classified as hexagonal. Even those sites which are both k sites are different if we look at the next neighbors. It is important to recognize the difference between k and h sites because these locations react differently to donor and acceptor substitutions. In 4H SiC, for example, a nitrogen atom (which acts as a donor) will have a different ionization energy when it substitutes at a k site in the crystal lattice than when it substitutes at an h site. Consequently, the single donor is responsible for two distinct donor levels in 4H SiC. Similarly in 6H SiC there are three different inequivalent sites, marked as h, k_1 and k_2.

1.3 EXCITON RECOMBINATION

1.3.1 Free Exciton

When a semiconductor is exposed to a laser with above bandgap photon energy, some of the electrons in the valence band will be excited and jump into the conduction band, leaving some holes back in the valence band. An electron and a hole may be bound together by the coulomb interaction force. This bound electron-hole pair is called an exciton.

In a direct bandgap semiconductor, where the minimum energy in the conduction band is at the same point in k-space as the maximum energy in the valence band, as shown in Figure 1.3 (a), the exciton can recombine directly without any phonons involved. This process will emit a photon with an energy of $hv = E_G - E_X$, where E_G is the bandgap of the semiconductor and E_X is the exciton binding energy.

In an indirect band gap semiconductor, the minimum energy in the conduction band does not occur at the same point in k-space as the maximum energy in the valence band, as shown in Figure 1.3 (b). The result is a significant change in momentum when an electron transition happens from the conduction to the valence band. In order to satisfy the conservation of momentum, the transition must also be accompanied by a phonon emission or absorption with the appropriate change in momentum. This additional requirement for electron-hole recombination makes the indirect band gap semiconductors rather inefficient at emitting light. The energy of the emitted photon is $hv = E_G - E_X - E_{ph}$, where E_{ph} is the energy of the phonon emitted during the recombination.

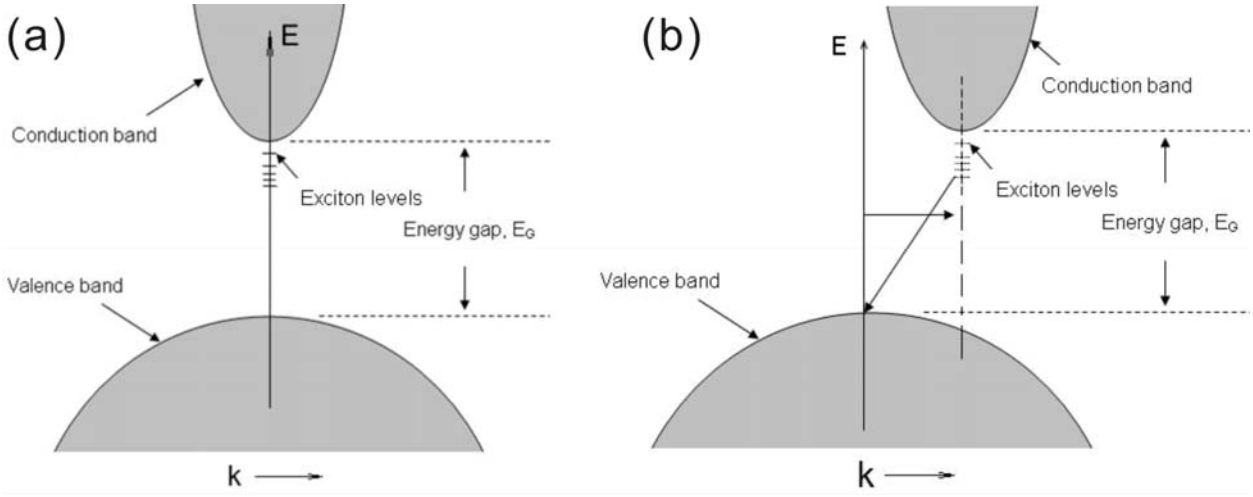

Figure 1.3 Schematic diagram of the exciton recombination process in a direct bandgap and an indirect bandgap semiconductor.

1.3.2 Bound Exciton and Four Particle Complex

What has been shown in the previous section is the creation and recombination of the free exciton, which is not bound to any impurities or defects. However, semiconductors are not absolutely impurity free. Excitons can be captured by neutral donors or acceptors and form bound excitons. Let's take the case of an exciton bound to a neutral donor as an example. There are in total four particles, including the ionized nitrogen donor core, two electrons, and one hole. This is called the four particle complex. An electron and a hole can recombine radiatively within such a four particle complex. As discussed above, recombination in an indirect band gap semiconductor typically requires a phonon emission, but recombination within a four particle complex can occur with or without a phonon emission. This is possible because the electron and hole wavefunctions partially overlap in k-space due to the fact that the bound exciton is localized. This leads to the existence of no-phonon lines in the low temperature photoluminescence (LTPL) spectrum of doped SiC. There are also phonon assisted emission lines (called "phonon replicas") which are shifted in energy from the no-phonon lines by the energy of the phonon emitted for conservation of momentum.

Just as the energy of a free exciton is shifted from the band gap energy by the binding energy of the electron and hole, the energy of a bound exciton in a four particle complex is shifted from the free exciton band gap by the exciton's binding energy to the donor or acceptor site. The energy of the emitted photon is $h\nu = E_G - E_X - E_{BX} - E_{ph} = E_{GX} - E_{BX} - E_{ph}$, where E_{BX} is the binding energy of the exciton and E_{ph} is the energy of the phonon emitted during the recombination. It is common to express an exciton's binding energy relative to the exciton energy gap, $E_{GX} = E_G - E_X$, because it is difficult to measure E_G for SiC, but straightforward to measure E_{GX} precisely.

Four particle complexes due to nitrogen in 6H, 15R, 3C and 4H SiC were first reported by Choyke et al. [1-5]. Several examples of the LTPL spectra of nitrogen bound excitons in low doped, moderately doped and highly doped 4H-SiC are shown in Figure 1.4. The notation I represents the intrinsic exciton related lines. The notations P and Q represent the nitrogen bound exciton related lines. The subscript numbers are the energies of the participating momentum conserving phonons in the unit of meV. It has been discussed earlier that in 4H SiC there are two inequivalent sites, which means there are two nitrogen levels. That's why these nitrogen related lines are marked in groups of P and Q. In this case, the shallower line P_0 is assigned to the hexagonal site h and the deeper line Q_0 is assigned to the cubic site k.

In Figure 1.4 (a), which is from a sample with a very low doping, the spectrum is dominated by the intrinsic lines. However, in Figure 1.4 (b), which is from a sample with a moderate doping, it is dominated by nitrogen bound exciton lines. Therefore it has been discovered that one can estimate the doping concentration of the sample by comparing the free exciton line I_{75} to the nitrogen no phonon line Q_0 [2-6], when the doping is in the range of 10^{13} - 10^{17} cm^{-3} and the sample is not compensated by aluminum acceptors. When the doping is above 10^{18} cm^{-3}, the spectrum doesn't show those characteristic sharp lines any more. What can be seen is mainly the broad nitrogen peak from the heavily doped sample. With increasing doping, the broad peak position shifts to the higher wavelength direction. It has also been used to estimate the doping of the highly doped samples.

One may notice that in the nitrogen bound four particle complex, the line Q_0 is much stronger than the line P_0. However, the spectrum is dominated by the phonon replicas from the P related center and the total area under P_0 and its phonon replicas is several times greater than the area under Q_0. In 4H SiC, the exciton binding energy of P_0 is smaller than that of Q_0. That means

the exciton bound to nitrogen at the Q_0 position is more localized. Therefore, the wavefunctions of the electron and hole can have bigger overlap in k space. The direct no phonon transition is favored for this site. So we see a strong no phonon line Q_0. Again, the exciton binding energy of P_0 is smaller than that of Q_0, therefore the electron wavefunction radius is bigger for P_0 position. A bigger radius results in a bigger capture cross section. So overall the spectrum is dominated by the phonon replicas of the P_0 line, although P_0 itself is smaller compared to Q_0.

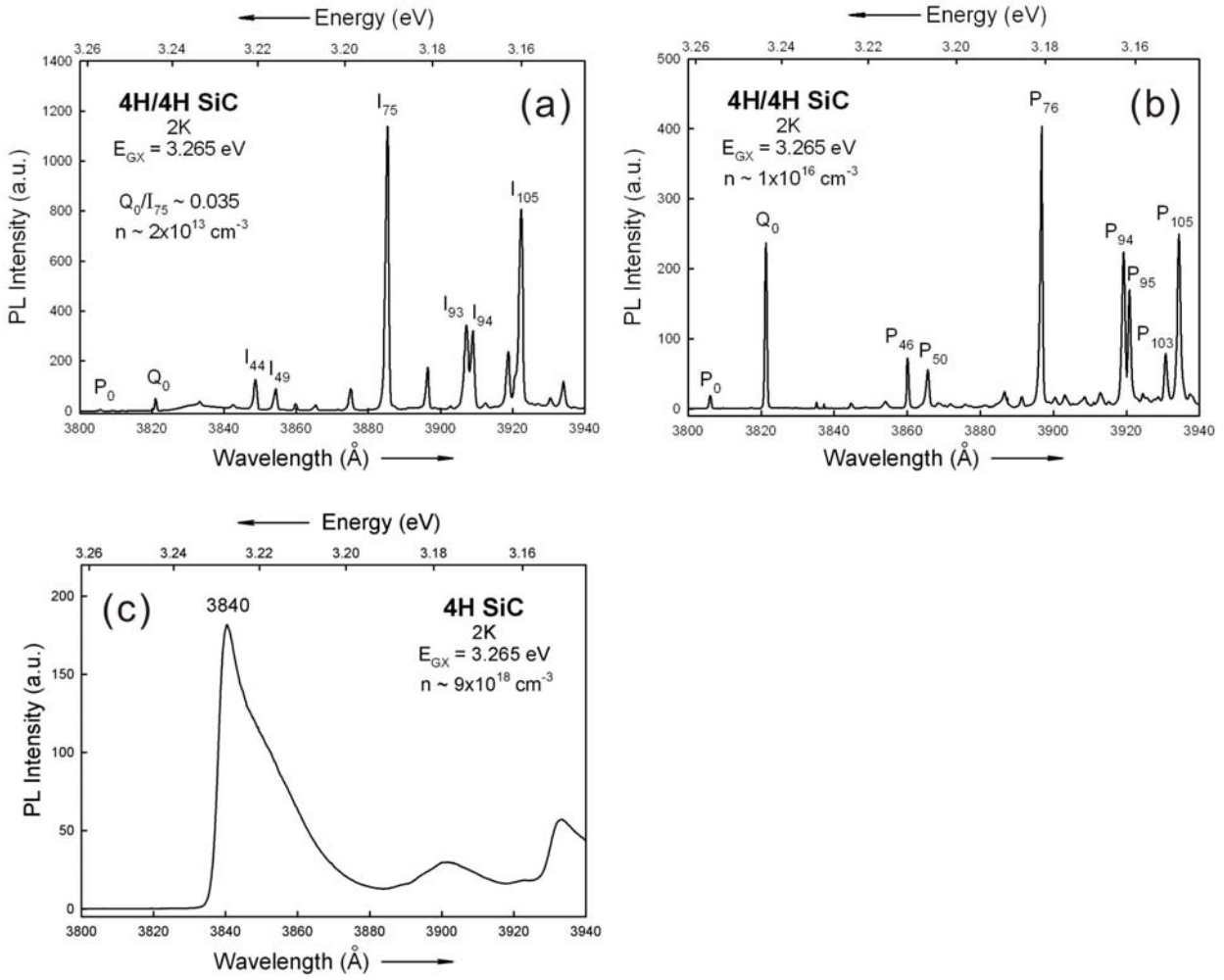

Figure 1.4 LTPL spectra of nitrogen bound excitons in (a) low doped (b) moderately doped and (c) highly doped 4H SiC.

In p-type aluminum doped SiC, excitons can be bound to the neutral aluminum acceptors and form four particle complexes. Clemen et al. published a paper which discussed the aluminum bound exciton spectra in some of the major SiC polytypes including 4H, 6H and 3C SiC [7].

1.3.3 Donor-Acceptor Pairs

Usually in p-type doped SiC, the low temperature luminescence spectrum contains many well-resolved sharp lines. These are from excitons bound to a complex called donor-acceptor pairs (DAP). A low temperature photoluminescence DAP spectrum in SiC was first reported by Choyke et al. in 1970 [8]. In the DAP recombination mechanism, electrons are bound to neutral donors and holes are bound to neutral acceptors. The electrons and holes then recombine radiatively and emit photons with the energy given by:

$$h\nu = E_G - (E_D + E_A) - E_C + E_{vdW} \tag{1.1}$$

where E_G is the energy gap, E_D and E_A are the donor and acceptor ionization energies, $E_C = -\frac{e^2}{\varepsilon r}$ is the Coulomb interaction energy between donor and acceptor ions separated by a distance r *after* electron-hole recombination, and E_{vdW} is the Van der Waals interaction energy between neutral donor and acceptor atoms *before* recombination [8]. The peak position of the luminescence is a function of the donor and acceptor distance r.

Choyke and Patrick studied the DAP luminescence in 3C SiC and got a very nice fit. It was concluded that the DAP in 3C SiC consists of nitrogen replacing carbon and aluminum replacing silicon, which is a Type II spectrum. If both donors and acceptors replace the same sublattice, it is called Type I. Ivanov, Magnusson and Janzén did similar work in 2003 on 4H SiC

which has two inequivalent sites [9]. Their results show that the recombination of pairs involving nitrogen donor and aluminum acceptor at hexagonal sites dominates the spectrum.

1.4 ORGANIZATION OF THESIS

In Chapter 2, I will present the theoretical models of different defect centers and what people have learned about some of the defects. The main focus is on the dicarbon antisite defect and the D_I defect.

Chapter 3 describes the experimental procedures in this project. This is an international collaboration involving researchers from the United States, Germany and Japan.

Chapter 4 discusses the results from our study on the dicarbon antisite. Experimental spectra are presented with high spectral resolution. We are able to fit the results with the Morse Potential model and it gives a very good prediction of the vibration energies up to the fifth harmonic with an error of less than 1%. First principles calculation by our collaborator Dr. Ádám Gali (theorist) also shows that the two-carbon dumbbell model can explain all the vibrational states observed in the experiments. The problem is simplified to a one-dimensional Schrödinger Equation, which can be solved numerically. The numerical calculation results show excellent agreement on the anharmonicity with the experimental results, which further confirms the reduced mass obtained from the first principle calculations. Additional dicarbon antisite no phonon lines are presented in this chapter. We also study the distribution of the irradiation electrons inside the SiC and explain the discrepancy between our results and a recently published paper. An unusual annealing behavior of the dicarbon antisite defect is also observed.

In Chapter 5, we summarize the systematic work we have done on the D_I defect in SiC. Defect centers are created by electron irradiation followed by annealing at different temperatures. Then we study the evolution of the D_I center observed in LTPL and try to correlate it to the defect centers observed in DLTS measurements. We first started with n-type 4H SiC and attempted to correlate the D_I optical center with the Z_1/Z_2 DLTS center, which was first proposed to be the associated to the D_I center. Our results show no correlation between these two. We repeated the whole experiment on p-type 4H SiC and attempted to correlate the D_I center with the observed DLTS HS1 center, which is proposed by the pseudodonor model. However, the thermal histories of these two defects don't show any correlation either. Therefore we cannot verify the pseudodonor model either.

In Appendix A, I explain the physics of the deep level transient spectroscopy and show how to extract the defect properties from the capacitance transient decay. The actual experiments are done by our collaborators at the University of Erlangen-Nürnberg in Germany.

Appendix B shows the Monte Carlo simulation of irradiation electrons inside SiC. It is done by a software called CASINO, but we have to apply it to our actual problem considering the incident electron energy and the creation threshold of defects.

Appendix C shows the work we have done on another defect center called D_{II} in SiC. The theoretical model is presented first, followed by the high-resolution variable temperature photoluminescence and Zeeman spectroscopy on an ion-implanted 3C SiC sample.

Appendix D presents the study of the phosphorus-related photoluminescence in SiC by intentionally doping the samples with phosphorus during growth. It is shown that phosphorus atoms substitute on the carbon lattice sites, in addition to the well-accepted mechanism of

substitution on the silicon sites. Phosphorus doping in four major SiC polytypes is studied in this appendix.

Appendix E shows a promising future use for high purity single crystal 4H and 6H SiC as an alternative cutting tool for ultra-precision nano-machining. It is demonstrated that SiC cutting tools polished to a sharp edge can be used for nano-machining of stainless steel and nickel, where conventional diamond tools wear rapidly and don't last.

2.0 DEEP LEVEL DEFECTS IN SILICON CARBIDE

2.1 BACKGROUND

Shallow dopants in SiC, such as nitrogen and aluminum have been studied extensively and the properties of these defects are well-understood. Besides these, there are some deep levels in the band gap of SiC. People don't understand too much about these deep centers. That doesn't mean they are not important. Actually it has been found that these deep centers are critical for the device fabrication because they are the killers of the lifetime. The deep centers could act as recombination centers in the devices. Ion implantation is often used in device fabrication along with high temperature annealing. After ion implantation, the crystal lattice is damaged. Vacancies and interstitials are created immediately as part of the energy loss mechanism of the penetrating ion. As the SiC is annealed, these vacancies and interstitials tend to either recombine or form some other defect complexes. Some of these deep defects could affect the device performance and people could get results very different from the original device design. Therefore we invested a lot of time and efforts to study the optical and electrical properties of some of the prominent defects.

As a compound semiconductor, there are two different kinds of vacancies in SiC, silicon vacancies V_{Si} and carbon vacancies V_C. Because of the different inequivalent sites in SiC, these vacancies also differ depending on the sites of the missing atoms. Figure 2.1 is taken from a

review paper by Bockstedte et al. [10] and shows the silicon and carbon vacancies at cubic and hexagonal sites in 4H SiC.

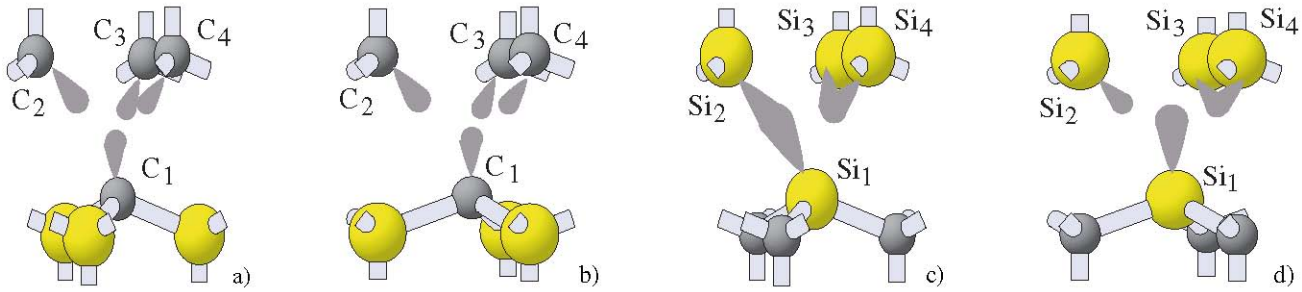

Figure 2.1 Geometry of the vacancies in 4H SiC. Silicon vacancy at the (a) cubic and (b) hexagonal sites. Carbon vacancy at the (c) cubic and (d) hexagonal sites. Yellow spheres represent silicon atoms. Gray spheres represent carbon atoms. Dangling bonds are also shown. Pictures are taken from Ref. [10].

When these two vacancies happen to be next to each other, they form a simple vacancy complex called a divacancy, as shown in Figure 2.2, which is also taken from Ref. [10]. The alignment of the complex with the c-axis is different in Figure 2.2 (a) and (b).

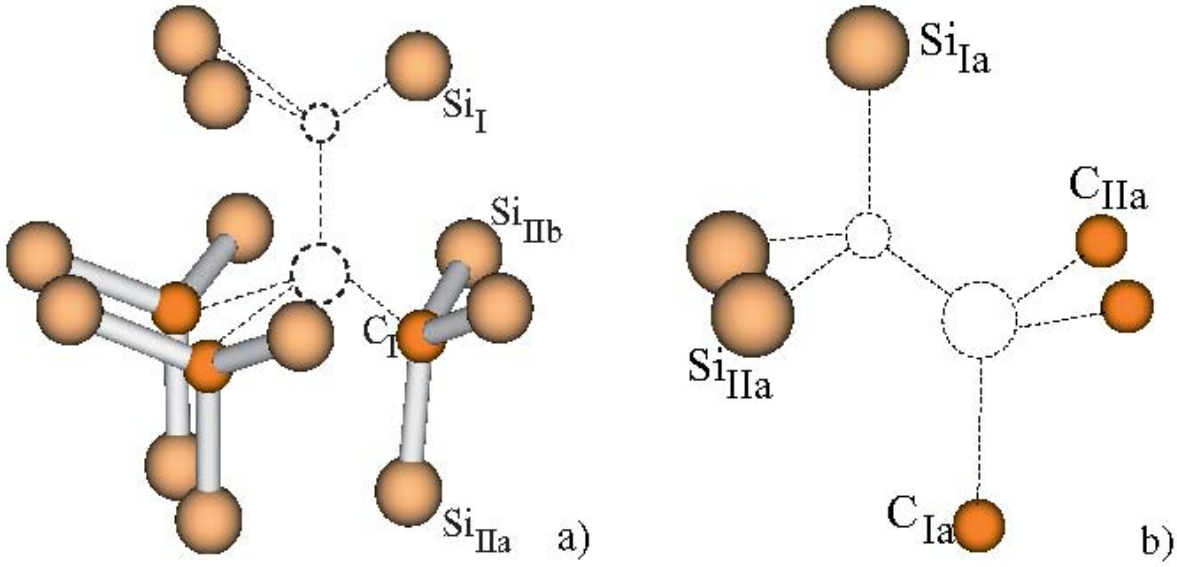

Figure 2.2 Geometry of the divacancy (a) axial complex at a hexagonal site and (b) off-axis complex V_C-V_{Si} (kh).

Another possible defect is called an antisite. That means a silicon (carbon) atom occupies a carbon (silicon) site. More complicated complexes can be formed from an antisite, such as a vacancy-antisite pair or an antisite-antisite pair. It is also possible that more than one carbon atom can occupy a silicon site and form a di-carbon antisite, tri-carbon antisite and tetra-carbon antisite, which can form a carbon cluster together with the surrounding carbon atoms. In the following sections, I will discuss the different models related to the defect centers we observed in our experiments.

2.2 DICARBON ANTISITE DEFECTS IN SILICON CARBIDE

In two recent papers published by Steeds *et al.* in Phys. Rev. B [11, 12] one finds a discussion of some unusual defect spectral lines in 4H SiC after electron irradiation. Steeds *et al.* did electron irradiation on 4H SiC using a modified transmission electron microscope (TEM). The electron fluences he used were between 10^{18} cm^{-2} and 10^{20} cm^{-2}. Most of the results he presents in these papers are from samples irradiated with fluences greater than 10^{19} cm^{-2}. The electron beam has a circular cross section with a diameter of either 100 μm or 200 μm and a uniform intensity distribution with a sharp cutoff at the perimeter. The optical excitation sources that were used are a 488 nm Ar ion laser and a 325 nm He-Cd laser. After electron irradiation and subsequent annealing, a number of "new" lines are observed in their LTPL spectra.

Our particular interest in the work of the Steeds group is a set of triplet lines at a_0 463.2, b_0 463.6 and c_0 464.2 nm with their local vibrational modes, which will be shown in Chapter 4 and have been discussed extensively in Ref. [11, 12]. Table 2.1 is taken from the original paper Ref. [11]. I have summarized the wavelengths and energies of these spectral lines in

Table 2.2 for direct comparison with our results later. Note that the error of the wavelength reading given in the paper is 0.8 Å. In this wavelength region, the corresponding error in energy is 0.5 meV. However the so called "observed" local vibrational mode energies have reported uncertainties of 0.03, 0.05 or 0.06 meV. As the authors state in the Table 2.1 title, the local vibrational mode data were obtained by averaging data from several experiments. This error is not consistent with the experimental raw data. In the case of our results there is an error of 0.14 Å in wavelength reading, which gives an error of 0.08 meV in energy. It appears that our results are more accurate in this high resolution spectral study.

Table 2.1 Wavelengths and energies of the three no phonon lines of the 463 nm triplet together with the energies of their local vibrational modes in 4H SiC. The local vibrational mode values were obtained by averaging data from several experiments carried out at different excitation wavelengths and have errors of 0.03 meV (Taken from Ref. [11]).

Optical center	(1) a_0	(2) b_0	(3) c_0
ZPL wavelength (nm)	463.15 ± 0.08	463.54 ± 0.08	454.26 ± 0.08
ZPL energy (eV)	2.676	2.674	2.670
Local vibrational mode energy (meV)	132.82 ± 0.03	132.54 ± 0.06	131.90 ± 0.05
Local vibrational mode energy (meV)	179.86 ± 0.03	178.47 ± 0.06	180.03 ± 0.05

Table 2.2 Photon wavelengths and energies of the no-phonon lines and local vibrational modes calculated from Table 2.1, for convenience in later comparison with our data.

	No phonon lines		Local vibrational modes		Local vibrational modes	
	Wavelength (Å)	Energy (eV)	Wavelength (Å)	Energy (eV)	Wavelength (Å)	Energy (eV)
a_0	4631.5	2.6762	4873.3	2.5434	4965.75	2.4961
b_0	4635.4	2.6740	4877.1	2.5415	4966.90	2.4955
c_0	4642.6	2.6698	4883.8	2.5380	4978.29	2.4898

By comparing the experimental results to the published results of *ab initio* local density approximation (LDA) calculations in two theory papers [13, 14], Steeds concludes that the triplet is actually formed by four lines. The middle two are relatively weak and too close to resolve in their setup. They conclude that the triplet lines are very likely connected with dicarbon antisites. In dicarbon antisite configuration, each of these two carbon atoms forms bonds with three neighboring carbon atoms (one of these being the other carbon in the pair) and there are two electrons left. These two electrons can form either a spin-0 (low-spin) or a spin-1 (high-spin) configuration [15]. Because of the stacking sequence in 4H SiC, there are two inequivalent sites in 4H SiC. One is a hexagonal site and the other one is a quasi-cubic site. Each of the two spin states is associated with these two inequivalent sites and therefore there are a total of four defects. The outside two lines a_0 and c_0 are from the low spin states. The middle line b_0 is actually from both high spin states and cannot be resolved in the real experiment. The connection with the theoretical calculations and the atomic model will be explained in detail in the next paragraph. Figure 2.3 is a schematic drawing which shows the perfect 3C SiC crystal structure and a dicarbon antisite in 3C SiC.

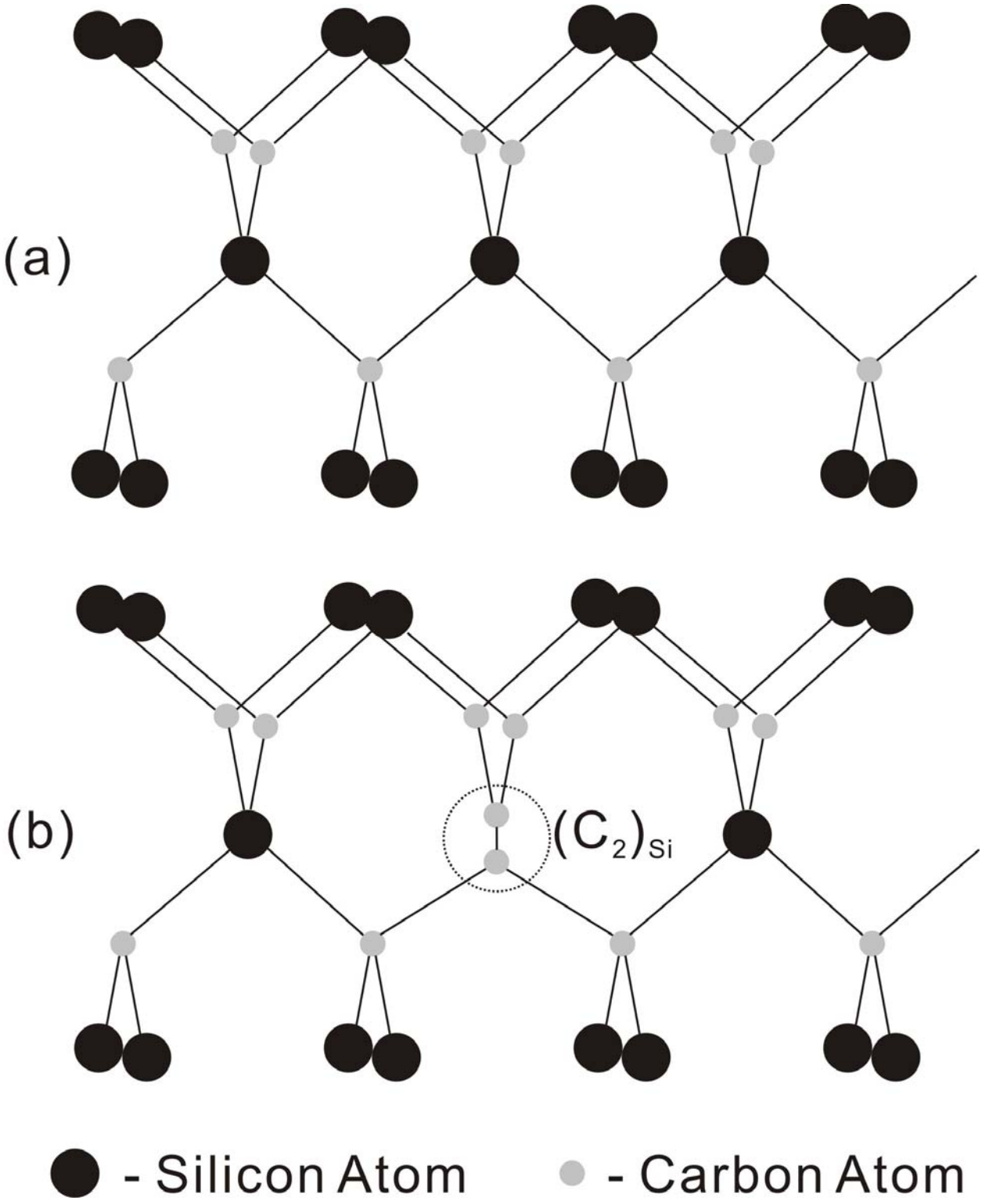

Figure 2.3 Structure of (a) a perfect 3C SiC crystal and (b) a dicarbon antisite in 3C SiC.

Since the high energy local vibrational mode is about 180 meV, which is greater than the highest lattice frequency 165 meV in diamond [16], the simplest model would be either a carbon split interstitial on a carbon site (two carbon atoms occupy a carbon site) or a dicarbon antisite so that it can generate a locally packed carbon environment similar to the diamond structure with several carbon atoms packed locally. Calculation shows that the carbon split interstitial defects are very mobile and therefore do not agree with the thermal stability of the triplet lines. The calculation of the dicarbon antisite shows that it is quite stable at relatively high temperature. The calculated local vibrational modes of the dicarbon antisites from different theoretical papers [13-15] are listed in Table 2.3 along with the experimental data from Table 2.1. By comparing the local vibrational modes, the a_0 line of the triplet is assigned as the $(C_2)_{Si,k}$ in the low spin state, and the c_0 line is assigned as the $(C_2)_{Si,h}$ in the low spin state. The b_0 line is assigned to the high spin states on both h and k sites. The high energy local vibrational modes of the high spin states are really close and cannot be resolved in the experiment. However, the low energy local vibrational modes are not in very good agreement with the calculations with 5-7 meV off.

Table 2.3 Calculated first local vibrational modes of dicarbon antisite $(C_2)_{Si}$ in 4H SiC from different theoretical papers along with the experimental data in the unit of meV. The subscripts h and k refer to the hexagonal and the quasi-cubic sites. ls denotes the low spin state. hs denotes the high spin state.

Ref. [13]	Ref.[14, 15] $(C_2)_{Si,k}$, ls	Ref [15] $(C_2)_{Si,h}$, ls	Ref [15] $(C_2)_{Si,k}$, hs	Ref [15] $(C_2)_{Si,h}$, hs	Experiment Table 2.1 $a_0/b_0/c_0$
180	178.0	179.4	177.0	177.1	179.86/178.47/180.03
138	139.1	139.3	137.6	137.6	132.82/132.54/131.90
123	135.0	136.2	136.2	136.4	
	119.7	121.9	120.7	121.0	
	102.3	103.0	101.5	100.2	

2.3 D_I DEFECTS IN SILICON CARBIDE

After annealing at high temperature above 1300 °C, the low temperature photoluminescence from ion-implanted SiC is usually dominated by the spectra from the well-known D_I and D_{II} defect centers, which are two very stable defects observed in the LTPL from ion-implanted SiC after high temperature annealing up to 1700 °C. They are both considered to be intrinsic defects since their spectra are independent of the implanted ion. The D_I center was first reported in 3C SiC in 1971 [17] and then in 6H SiC in 1972 [18] by Choyke et al. Both the D_I and D_{II} centers were first observed in ion-implanted 15R SiC by Choyke et al. in 1972 [19]. The D_{II} center in ion-implanted 3C SiC was first reported by Choyke et al. in 1973 [20]. The spectra of D_{II} in 6H and 4H SiC were published by S.G. Sridhara et al. in our group over ten years ago [21].

The D_I spectrum at 2 K has a no phonon line L_1 in 4H SiC at 4272 Å (2.901 eV). In 6H SiC the D_I spectrum consists of three no phonon lines at L_1 4722 Å (2.625 eV), L_2 4788 Å (2.589 eV) and L_3 4823 Å (2.570 eV). In 3C SiC it has a no phonon line L_1 at 6280 Å (1.974 eV). There is a phonon gap between the acoustical and optical branches in SiC. The D_I defect has been reported to have two localized modes in this phonon gap. They are at 82.0 and 82.9 meV in 3C SiC, 82.7 and 83.4 meV in 4H SiC and 82.8 and 83.7 meV in 6H SiC [22, 23].

The D_{II} spectrum at 2 K has a no phonon line in 3C SiC at 5373 Å (2.307 eV). In 6H SiC four no phonon lines are clearly resolved at 4202 Å (2.9498 eV), 4204 Å (2.9484 eV), 4205 Å (2.9477 eV) and 4210 Å (2.9442 eV). In 4H SiC it has a no phonon line at 3868 Å (3.205 eV).

Even though these deep defect centers have been studied for almost forty years, not too much progress has been made except that now people can get better spectra thanks to the much improved growth technology. People are still trying to figure out the atomic models of these defects.

2.3.1 Pseudodonor Model of the D_I Center

Deep level transient spectroscopy (DLTS) was widely used to study the deep defect centers in SiC from the beginning of the 1990's [24, 25]. Dalibor et al. studied the intrinsic defects mainly in 4H SiC after ion implantation and annealing steps [26-28]. Our group was also involved in all the work done by Dalibor et al. It was reported that in 4H SiC a one-to-one association was found between the D_I center in the LTPL spectra and the Z_1/Z_2 center at E_C - 0.68 eV in the DLTS spectra, mainly because both centers show similar behavior in terms of defect generation, thermal stability up to 2000 °C and an increase in the intensities of both peaks with increase in the ion bombardment fluence. Therefore it was proposed that these two centers are caused by the same intrinsic defect complex [26]. However, in another paper published by the same group of authors, even though the authors didn't point this out, it is clear that the intensity of the L_1 line of the D_I center on a He^+ implanted 4H SiC sample increases substantially from annealing at 430 °C to 1000 °C, while the Z_1/Z_2 concentration only increases slightly from $4x10^{15}$ cm^{-3} to $5x10^{15}$ cm^{-3} [28].

Some papers on the nature of the D_I center were published by the Linköping Group in Sweden [29, 30]. The authors proposed a model saying that the D_I defect is a pseudodonor in 4H SiC. The defect has a (+/0) charge transition level in the bandgap. It contains no charged particle at the neutral state but acts as a hole trap when the Fermi level is above this level. The D_I center is an isoelectronic defect and the bound exciton consists of a strongly localized hole at the defect with a loosely bound, effective-mass-like electron bound via Coulomb coupling. The lowest excited state of the loosely bound electron is the initial state of the L_1 recombination. The photoluminescence excitation (PLE) study in Ref. [29] shows a series of lines between 45 and 65 meV higher than the energy of the L_1 no phonon line. By fitting the strongest component within

the electron-hole coupling groups to the simple hydrogenic theory, they found the value of 62 meV as the energy of the series limit, which means the electron is promoted into the conduction band. The L_1 recombination energy from the LTPL measurement is 2.901 eV. Therefore, the ground state of this pseudodonor is 2.901 + 0.062 = 2.963 eV below the conduction band. This is the energy needed to promote an electron from the defect in its ground state into the conduction band, leaving the defect in a positively charged state with a localized hole. The binding energy of the hole equals the bandgap energy minus the ground state energy of the pseudodonor. It should be 343 meV above the valence band. The schematic diagram of the pseudodonor model is shown in Figure 2.4. The authors observed a hole trap called HS1 at 0.35 eV above the valence band by minority carrier transient spectroscopy (MCTS), which is consistent with the pseudodonor model. Therefore, they believe the D_I center is correlated to the HS1 center, not the Z_1/Z_2 center as reported from the DLTS spectra [26]. The authors in Ref. [30] tried to show the direct correlation between the L_1 intensity and the HS1 hole trap concentration in a large set of samples. Their figure (not shown here) does not seem to be very clear and convincing, even though a solid line is used as a guide for the eye.

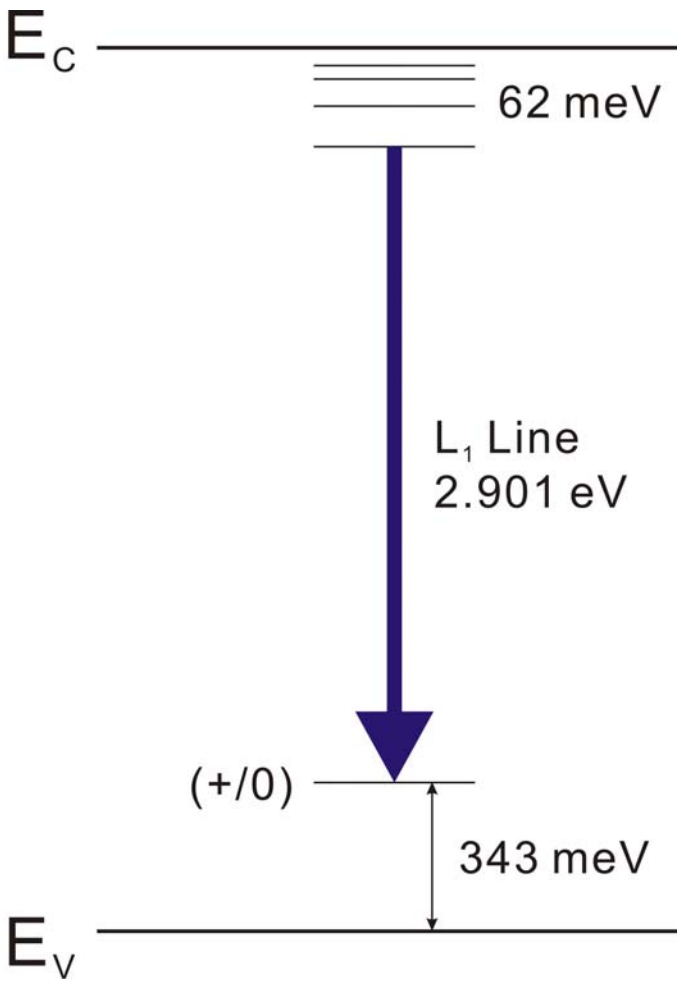

Figure 2.4 Bandgap diagram of the pseudodonor model.

2.3.2 Atomic Model of the D_I Center

Several models have been proposed for the D_I center. It was first suggested to be an impurity-vacancy complex on nearest-neighbor sites based on the extensive work on radiation damage and annealing on Si [17]. However, it was soon found that the D_I center is independent on the impurities and a new pure defect model of divacancy was suggested [18]. In a theoretical paper published by Eberlein et al. in 2003 [31], first-principle density functional calculations were used to investigate antisite pairs in 4H SiC and the nearest neighbor antisite pair was suggested to be

the model of the D_I center. The structure of the antisite pair is shown in Figure 2.5 (b). Out of many possible vibrational modes, a Si related local vibrational mode at 624.9 cm^{-1} (78 meV) from calculations is close to the experimental result of 669.4 cm^{-1} (83 meV) [17, 18].

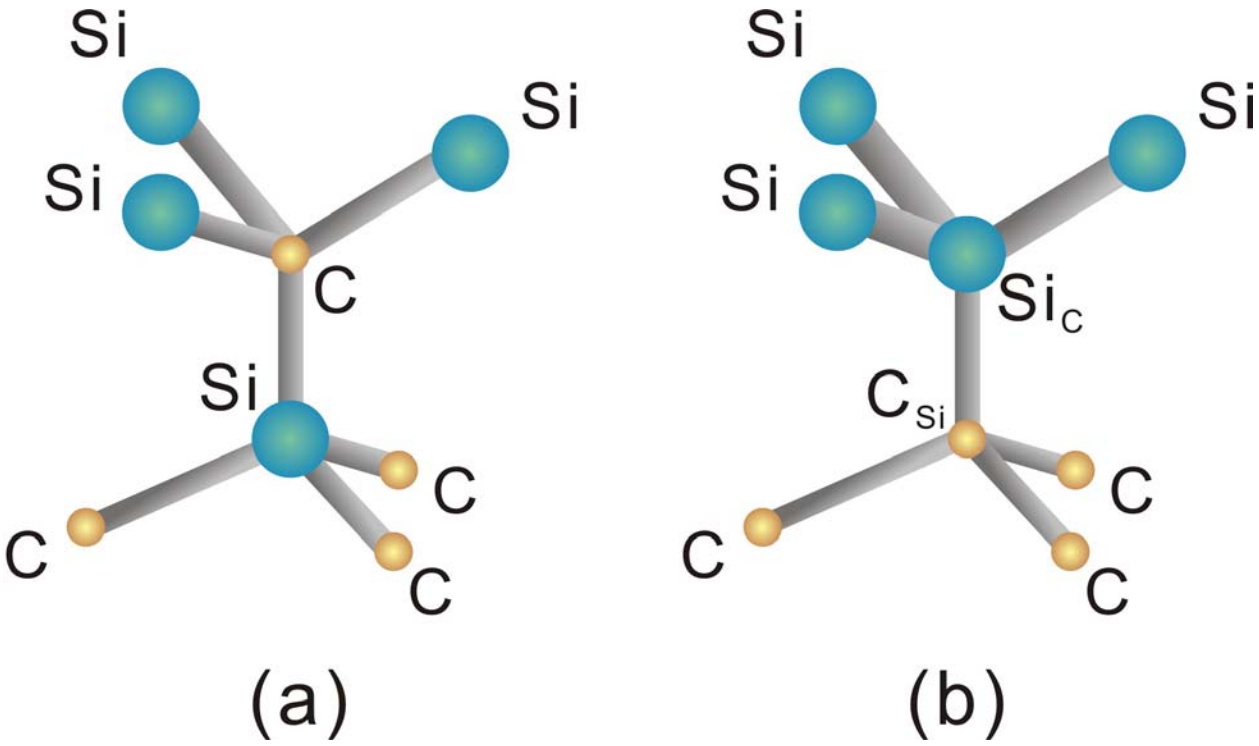

Figure 2.5 The geometry of (a) a perfect lattice and (b) the antisite pair at the k site.

Gali et al. did their own calculation using density functional theory in the local density approximation (DFT-LDA) and suggested that the neutral antisite pair is indeed a good candidate for the D_I center [22, 23]. The authors used a 128 atom fcc unit cell for 3C SiC and 96 atom hcp unit cell for 4H SiC. In 4H SiC, the one-electron levels are calculated by the CRYSTAL'98 code. There is an a_1 level at E_V + 0.16 eV and an *e* level at E_V + 0.38 eV. The calculated (+/0) level is at E_V + 0.3 eV. The local vibrational modes of the antisite pair in 3C SiC were calculated. The most interesting modes are a degenerate *e* mode at 627 cm^{-1} and an a_1 mode at 641 cm^{-1} which correspond to stretching modes of the compressed Si-Si bonds. The experimental values of the D_I local vibrational modes are 661 and 669 cm^{-1} in 3C SiC. The authors think the

calculations are comparable to the experimental results and that there are actually three local vibrational modes for the antisite pair model. The first mode may consist of two modes very close to each other. The authors also calculated the local vibrational modes of the isolated C_{Si} and Si_C. The calculated local vibrational modes of the isolated C_{Si} fall into the phonon continuum band. The isolated Si_C has one triply degenerate local vibrational mode and another local vibrational mode in the phonon band gap. Therefore, the total number of local vibrational modes in the phonon band gap depends on the number of compressed Si-Si bonds. There are three local vibrational modes for the antisite pair and four for the isolated Si_C. The authors also calculated the formation energies and one-electron defect levels. The formation energy of the antisite pair is lower than that of the Si vacancy. The calculated highest one-electron level is at $E_V + 0.38$ eV = $E_C - 2.88$ eV in 4H SiC, which is close to the transition energy of the no phonon line (2.901 eV) from the LTPL result. This energy is actually close to the pseudodonor model, which gives an energy level at $E_V + 0.343$ eV. The calculated and experimental results in 3C SiC are also very close. From the calculation, the (+/0) occupation level is at about $E_V + 0.3$ eV in 4H SiC. If this is correct, it tells us that the antisite pair is neutral in n-type and moderately p-type materials and the D_I spectrum can only be seen in n-type and moderately p-type SiC. It should not be seen in heavily doped p-type SiC as the D_I defect is positively charged in this case. From our experience during the study of the D_I defect in 4H SiC with different doping from high n-type to high p-type, it is true that we did not see L_1 line after both 170 keV and 1 MeV electron irradiation in the heavily p-type doped samples ($p \sim 4 \times 10^{18}$ cm^{-3} and 6.7×10^{17} cm^{-3}). The authors of Ref. [23] attempted to correlate the D_I center to the HS1 center at $E_V + 0.35$ eV reported by Zhang et al. [32], instead of the well-known Z_1/Z_2 center. As will be shown in our results, we have seen a DLTS center at $E_V + 0.34$ eV in our systematic work on electron irradiated p-type doped 4H SiC.

In another paper published by Pinheiro et al., the authors proposed the model of a $Si_C(C_{Si})_2$ complex as a candidate for the D_I center [33]. Their calculated local vibrational modes from the $Si_C(C_{Si})_2$ complex match the experimental values better than the Si_CC_{Si} antisite pair model. According to this model, the formation of the complex starts from an isolated Si vacancy V_{Si}, as shown in Figure 2.6 (a). After being annealed at 750 °C, the nearest neighbor carbon atom can move into this V_{Si} and form a $C_{Si}V_C$ pair, as shown in Figure 2.6 (b). During the annealing between 750 °C and 1200 °C, the carbon vacancy in the $C_{Si}V_C$ pair can be filled by a neighboring silicon atom, leaving a silicon vacancy behind. This process is illustrated in Figure 2.6 (c). This forms a complex $C_{Si}Si_C + V_{Si}$. This silicon vacancy V_{Si} can be filled up by a neighboring carbon atom simultaneously, making the complex as $C_{Si}Si_CC_{Si}V_C$ in Figure 2.6 (d). Further annealing at temperature above 1200 °C can cause the dissociation of the V_C and leave the $Si_C(C_{Si})_2$ complex as the possible atomic structure of the D_I center. In this model, the gap modes consist of vibrations of both carbon antisites and their carbon neighbors which lie in the same plane as the defect itself, as shown in Figure 2.7. In this model proposed by Pinheiro et al., the two nearby gap modes are caused by the asymmetric and symmetric vibrations of the two carbon neighbors with respect to the carbon antisite. This is quite different from the antisite pair model suggested by Gali et al. [22], in which the gap modes are associated with the compressed Si-Si bonds. However, we can question this model on the initial isolated silicon vacancy V_{Si}. D_I center has been found in low energy electron irradiated SiC when the electron energy is less than the Si displacement threshold. Therefore, the $Si_C(C_{Si})_2$ model cannot explain the formation in this case.

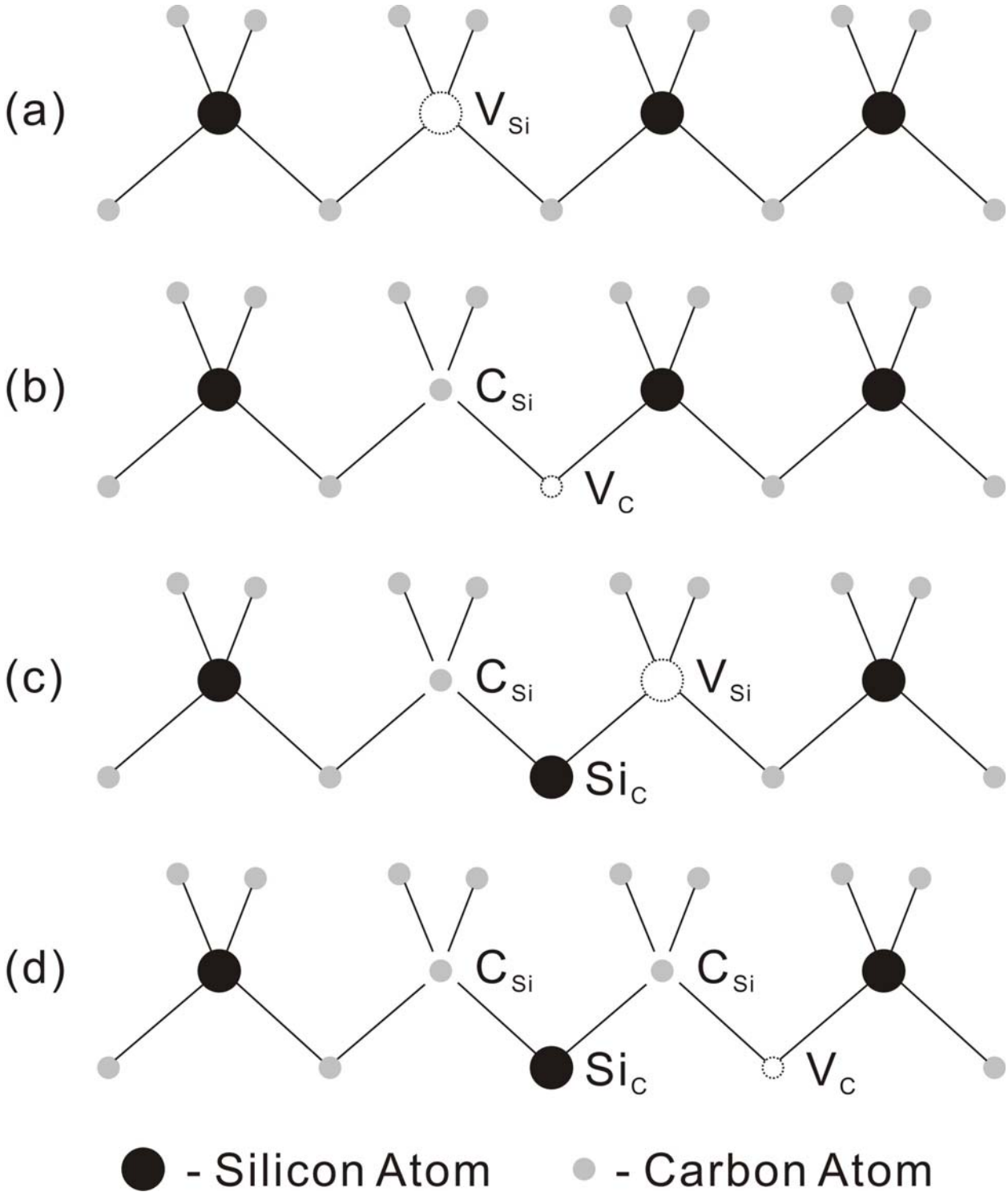

Figure 2.6 Formation of the $Si_C(C_{Si})_2$ complex starting from a Si vacancy. (a) The initial Si vacancy in the lattice. (b) Creation of a $C_{Si}V_C$ pair after 750 °C annealing. (c) Creation of a $C_{Si}Si_C + V_{Si}$ complex after annealing between 750 °C and 1200 °C. (d) A $C_{Si}Si_CC_{Si}V_C$ complex is formed simultaneously.

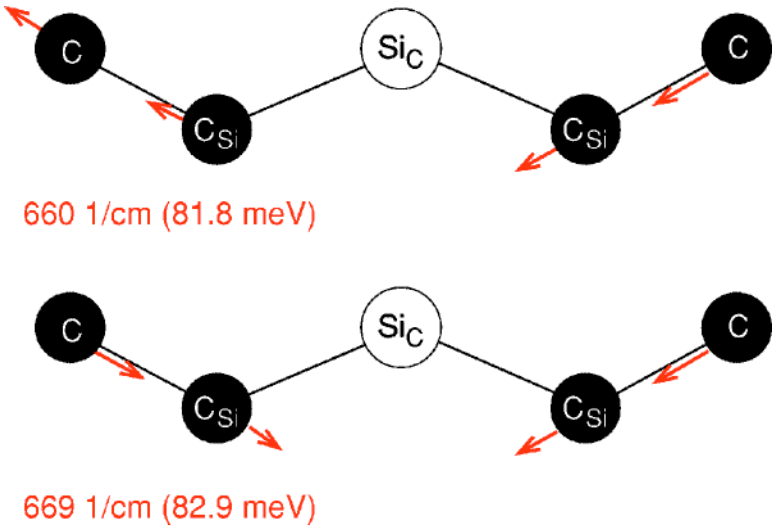

Figure 2.7 The localized modes in the phonon gap in the case of the $Si_C(C_{Si})_2$ antisite complex. Taken from Ref. [33].

In a paper published by Eberlein et al. in 2006 [34], the authors used local density functional calculations and found that neither the close-by antisite pair nor the close-by antisite pair adjacent to a carbon antisite is stable enough to explain the D_I center. They associated the isolated Si_C antisite with the D_I center. The calculated gap modes of the isolated Si_C antisite are 82.1 meV and 83.4 meV, which are also close to the experimental values of 82.7 meV and 83.4 meV. In the SiC after low energy electron irradiation which doesn't create any Si vacancies, the isolated Si_C is not formed at low temperatures. When the sample is annealed at temperatures greater than 1200 °C, the C vacancies can trap the mobile Si interstitials and form the Si_C antisites. However, our experiments have shown that the D_I defect can form at temperatures much lower than that. Annealing at 900 °C is high enough to bring strong L_1 defect lines. Therefore, this particular model is not totally convincing in this aspect. This might implicate that calculation of gap modes is not a very effective method for identifying the center.

3.0 EXPERIMENTAL TECHNIQUES

3.1 SAMPLE PREPARATION

The epilayers used for electron irradiations were grown in a horizontal hot-wall chemical vapor deposition (CVD) reactor in Prof. Kimoto's group at Kyoto University, Japan. The n-type epitaxial thin films are 20 μm thick and the doping is in the range of N_D-N_A ~ 2-4x10^{15} cm^{-3}. The p-type epitaxial thin films are 15 μm thick and the net doping concentration N_A-N_D is in the range of 3-4x10^{15} cm^{-3}.

Electron irradiation was carried out in Dr. Ohshima's group at the Japan Atomic Energy Agency (JAEA) in Takasaki, Japan. The polytype-inclusion free samples were uniformly bombarded by electrons at either 170 keV with a fluence of 5x10^{16} cm^{-2} or 1 MeV with a fluence of 1x10^{15} cm^{-2}. The electron energies required for carbon and silicon atom displacements are about 100 keV and 250 keV, respectively [35, 36]. Therefore 170 keV electrons will knock out just carbon atoms in the SiC lattice, while 1 MeV electrons will displace both silicon and carbon atoms. We hope this could give us a chance to judge whether a damage center requires just carbon vacancies and interstitials or both carbon and silicon vacancies and interstitials. The 170 keV electrons penetrate to around 90 μm deep and the 1 MeV electrons penetrate to 1 mm. The penetration depth of electrons with different energies can be calculated using a simulation program called CASINO [37]. More details about this program are discussed in Appendix B. We

also want to point out that the electron irradiation experiments by Dr. Ohshima's group were carried out in an accelerator with a uniform incident electron beam. The reason we want to make this clear is because we are going to compare our results to the literature in which the authors used a modified transmission electron microscope to do the electron irradiation. I will show the significant difference between these two techniques.

The samples were annealed in Ar for 30 min at temperatures between 700 °C and 1700 °C with 100 °C intervals. Temperatures were raised directly from room temperature to the desired temperature on every individual sample. A particular sample was annealed only once, so a large number of identical samples were required for this study.

Samples for ion-bombardment experiments were non-intentionally doped and the H^+ and $^4He^+$ bombardments were at the $5x10^{10}$ cm^{-2} fluence levels.

3.2 LOW TEMPERATURE PHOTOLUMINESCENCE

The low temperature photoluminescence measurements were carried out at 2 K using an immersion type liquid He cryostat, which was pumped below the lambda point (2.17 K). The luminescence was dispersed in an asymmetric Czerny-Turner spectrometer and collected with a liquid nitrogen cooled charge-coupled device (CCD) array. We calibrate the wavelength in every panel using the well-known noble gas discharge lines. The general schematic diagram of the whole setup is shown in Figure 3.1 with some experimental details marked on the figure.

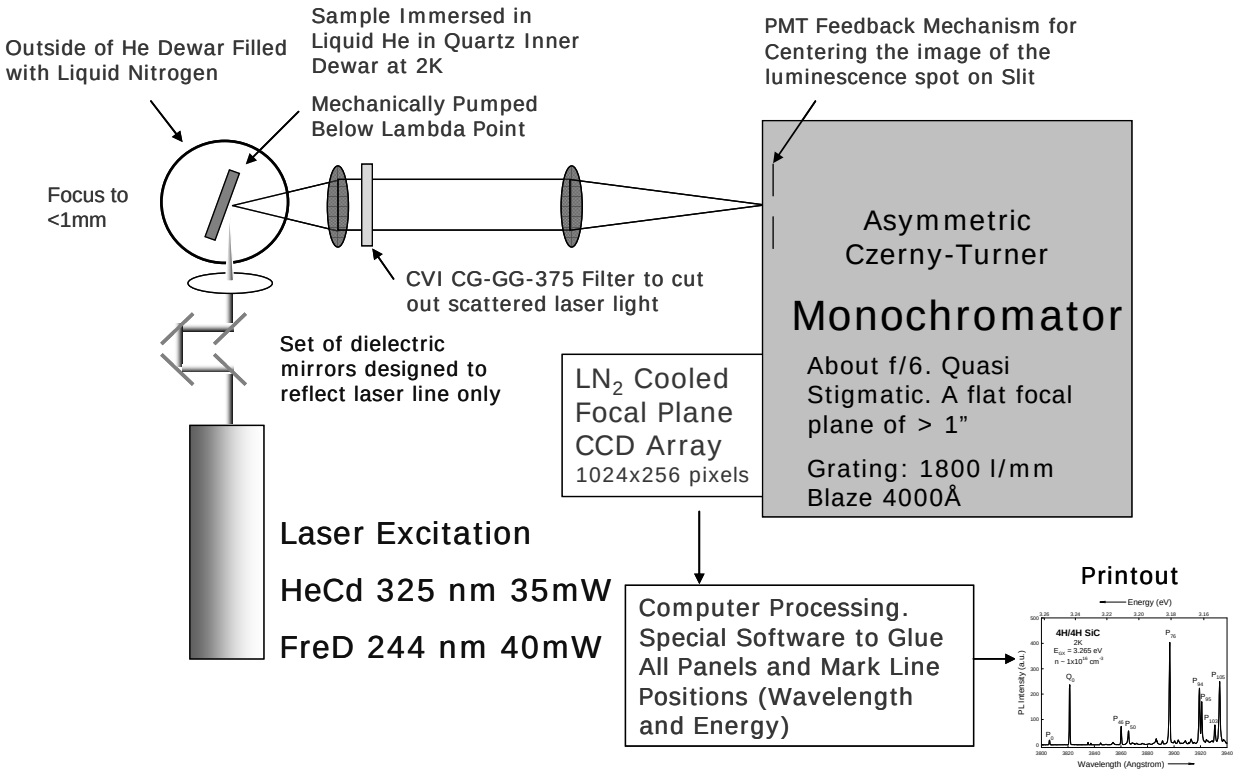

Figure 3.1 Schematic drawing of the LTPL setup

We have two different lasers to choose in our lab. One is a HeCd laser with a wavelength of 325 nm and a power of 35 mW. The other one is a frequency doubled argon ion (FRED) laser with a wavelength of 244 nm and a power above 40 mW. We pick one of these two lasers depending on the thickness of the epilayer we need to measure. The penetration depth of the HeCd 325 nm laser is about 3-8 μm and it is less than 1 μm for the FreD 244 nm laser at 2K, depending on the SiC polytype [38]. When the doping of the sample is low, the laser can penetrate much deeper because of the exciton diffusion. We always have the laser beam reflected several times from a set dielectric mirrors to eliminate the plasma lines in the laser. The laser beam is then focused onto the sample surface with a diameter less than 1 mm. The sample is immersed inside the liquid helium cryostat which is connected to a mechanical pump. The liquid helium reaches the superfluid state when the pressure is below the Lambda point (2.17 K). Operating at 2 K and below eliminates the noise generated from the helium bubbling in the light

path. The luminescence coming out from the sample passes through two lenses and a cutoff filter is used to remove the scattered laser light. The luminescence is finally focused onto the entrance slit of an asymmetric Czerny-Turner spectrometer with a grating of 1800 l/mm blazed at 4000 Å. The entrance slit we use is usually 100 μm. A smaller slit is used in case we need to get a better resolution, but that also reduces the amount of light going into the spectrometer. We have a liquid nitrogen cooled CCD mounted on the focal plane of the spectrometer. It is connected to a computer and a commercial software is used to collect and save the data. Further data processing is done on other computers.

Most of the samples we have measured using LTPL have Si-terminated (0001) face (i.e., the epilayers were grown on this face). The c direction is either perpendicular to the sample surface or has a small off-cut angle of 4° or 8°. Therefore, the photoluminescence coming out from the sample is dominated by $E \perp c$ polarization. The spectra presented in this thesis are collection with this $E \perp c$ polarization configuration unless specified otherwise. Sometimes we wanted to determine the polarization dependence of certain spectral lines and we used $<11\bar{2}0>$ a-face samples. X-ray Laue transmission patterns were first taken to determine the c direction on the sample surface [39]. We still use the same way to mount the sample but now the photoluminescence coming out of the sample is un-polarized. A Glan-Thompson polarizer is put between the cryostat and the spectrometer. By rotating the polarizer we can collect either $E \perp c$ or $E \parallel c$ polarized light.

3.3 DEEP LEVEL TRANSIENT SPECTROSCOPY

The deep level defects in semiconductors are usually characterized by Deep Level Transient Spectroscopy (DLTS), which was first proposed by D.V. Lang in 1974 [40]. The properties of the deep level defects, such as the energy levels and concentrations, are extracted by analyzing the capacitance transient decay of a Schottky diode after applying a reverse bias on the diode. The fundamental physics of this technique is explained in Appendix A based on the original paper published by D.V. Lang and the book written by Dieter K. Schroder [41]. Since we don't do this DLTS here in our group, I am not going to get into the technical details in this section. All the DLTS measurements were done by Prof. Pensl's group at the University of Erlangen in Germany.

4.0 DICARBON ANTISITE DEFECT IN 4H SILICON CARBIDE

4.1 SPECTRA FROM LTPL EXPERIMENTS

During our study of the deep defects, we have observed a set of triplet lines with their local vibrational modes in both 170 keV and 1 MeV electron irradiated n-type and p-type 4H SiC annealed at temperatures below and including 1300 °C. We also noticed that we had seen these lines before in Hydrogen and Helium ion-implanted 4H SiC. These triplet lines have first order phonon replicas of about 132 meV and 180 meV. However, for the second harmonic replicas a combination of the 132 meV and 180 meV modes is also observed. Figure 4.1 shows the triplet no-phonon lines and their first order local vibrational mode lines with different energies from an n-type Si-face 4H SiC sample bombarded by 1 MeV electrons with a fluence of $1x10^{15}$ cm^{-2} and later annealed at 1500 °C plus 1100 °C in Ar atmosphere for 30 min. I will explain the annealing procedure later in this chapter. The accurate readings of these different lines in Figure 4.1 are listed in Table 4.1. Figure 4.1 (a) is the full range spectrum showing all these lines. Figure 4.1 (b), (c) and (d) show the no-phonon lines, first order low energy local vibrational modes and high energy local vibrational modes, respectively. Note that in Figure 4.1 (d), part of the spectrum containing the $H_1{}^b$ has been magnified by a factor of 50 so that the $H_1{}^b$ peak can be seen clearly. In Ref. [11, 12], the authors claim that they occasionally saw a splitting of 0.6 meV at the position of the T_1 high energy local vibrational mode line ($H_1{}^a$ line in our notation), as shown in

Figure 4.2 (b). However, the two split lines have almost equal intensity. This is likely due to stress splitting or possibly the extra line is a spurious spike. The energy separation of the a_0 and b_0 no phonon lines is 1.9 meV from our measurements. Our data show that the energy separation of H_1^a and H_1^b is 2.6 meV, which is close to the no phonon line value and more importantly, we have seen this small H_1^b peak consistently in different samples after different bombardment conditions.

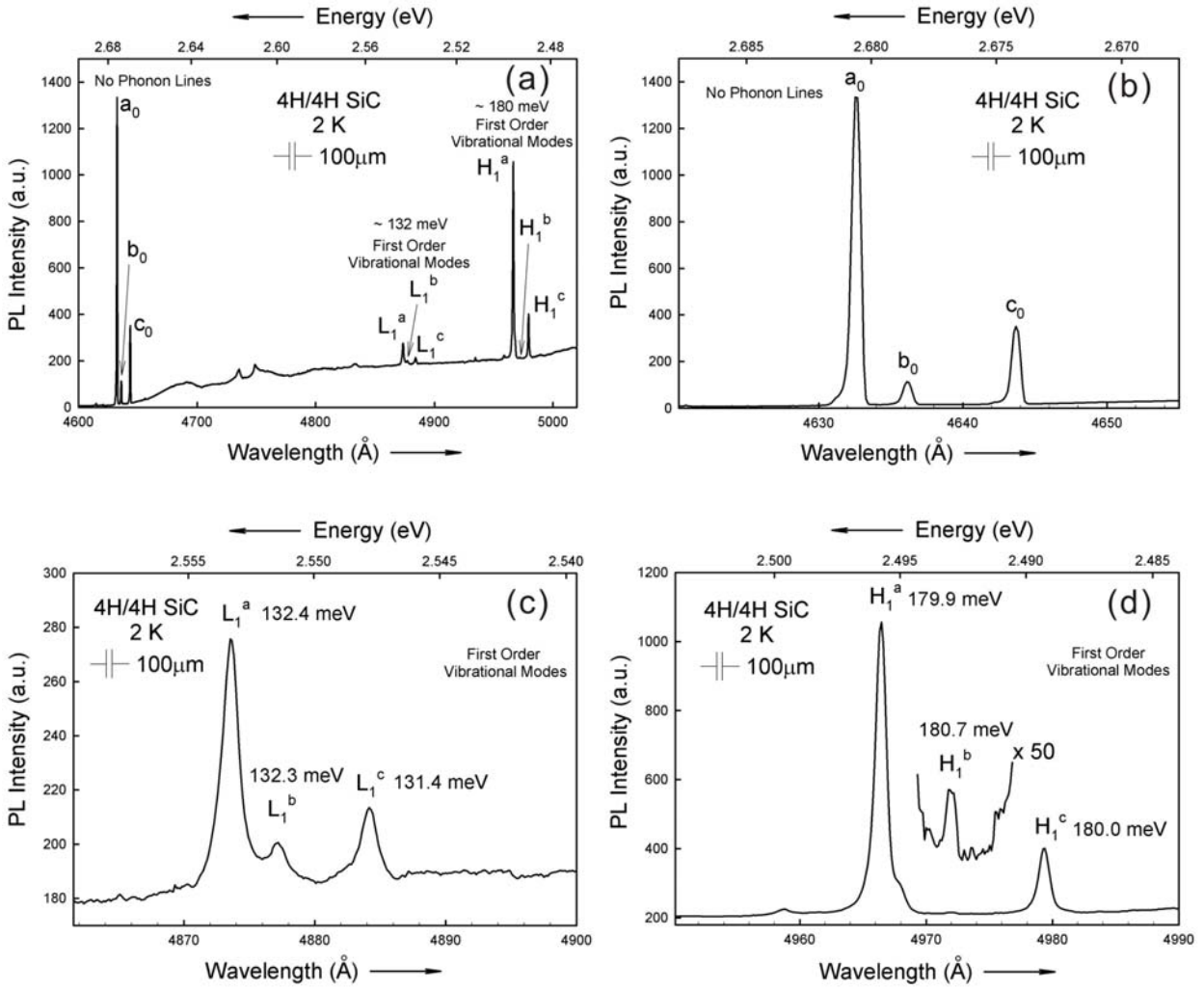

Figure 4.1 Triplet no-phonon lines and their first order local vibrational mode lines with different energies. (a) Full range spectrum showing all these lines. (b) No-phonon lines. (c) First order low energy local vibrational modes and (d) First order high energy local vibrational modes. This is from an n-type 4H SiC sample bombarded with 1 MeV electrons and later annealed at 1500 °C and 1100 °C.

Table 4.1 Wavelengths and energies of the no-phonon lines and local vibrational modes from our data in Figure 4.1.

	No phonon lines		Low energy local vibrational modes		High energy local vibrational modes	
	Wavelength (Å)	Energy (eV)	Wavelength (Å)	Energy (eV)	Wavelength (Å)	Energy (eV)
a_0	4632.46	2.67568	4873.53	2.54333	4966.44	2.49575
b_0	4635.79	2.67376	4877.07	2.54148	4971.75	2.49309
c_0	4643.51	2.66932	4884.02	2.53787	4979.38	2.48927

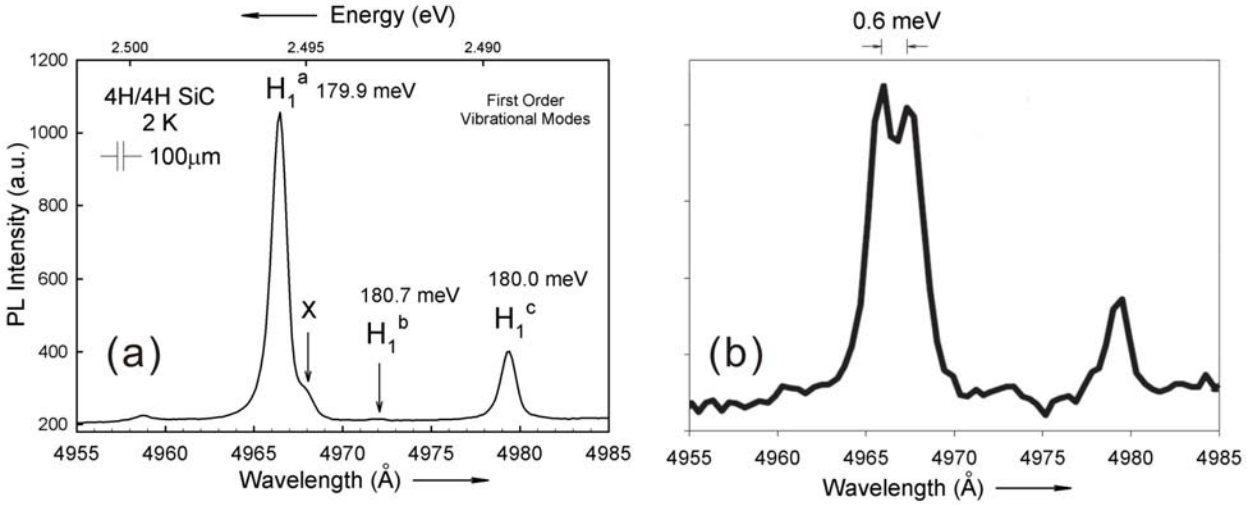

Figure 4.2 High energy local vibrational modes from (a) our data and (b) Ref. [11] by Steeds.

However, there is indeed a small bump on the high energy shoulder of the H_1^a peak. A curve fitting was tried in the wavelength region between 4962 Å and 4972 Å. The result is shown in Figure 4.3. The black curve is the original experimental result. The two green peaks are the results from Gaussian fitting. We have tried different fitting methods but cannot get a perfect fitting. The result I am showing here does not fit on the high energy side. But it serves the purpose of the peak separation on the low energy side. There appears to be a real peak at the

wavelength of 4967.91 Å. It has a 1.5 Å separation from the strong local vibrational mode line H_1^a. Its energy is 0.8 meV lower than the energy of line H_1^a. Assuming that the vibrational modes have the same energies, we conclude that it cannot be the local vibrational mode line H_1^b since the separation between the no phonon lines a_0 and b_0 is 1.9 meV. We just mark it as X.

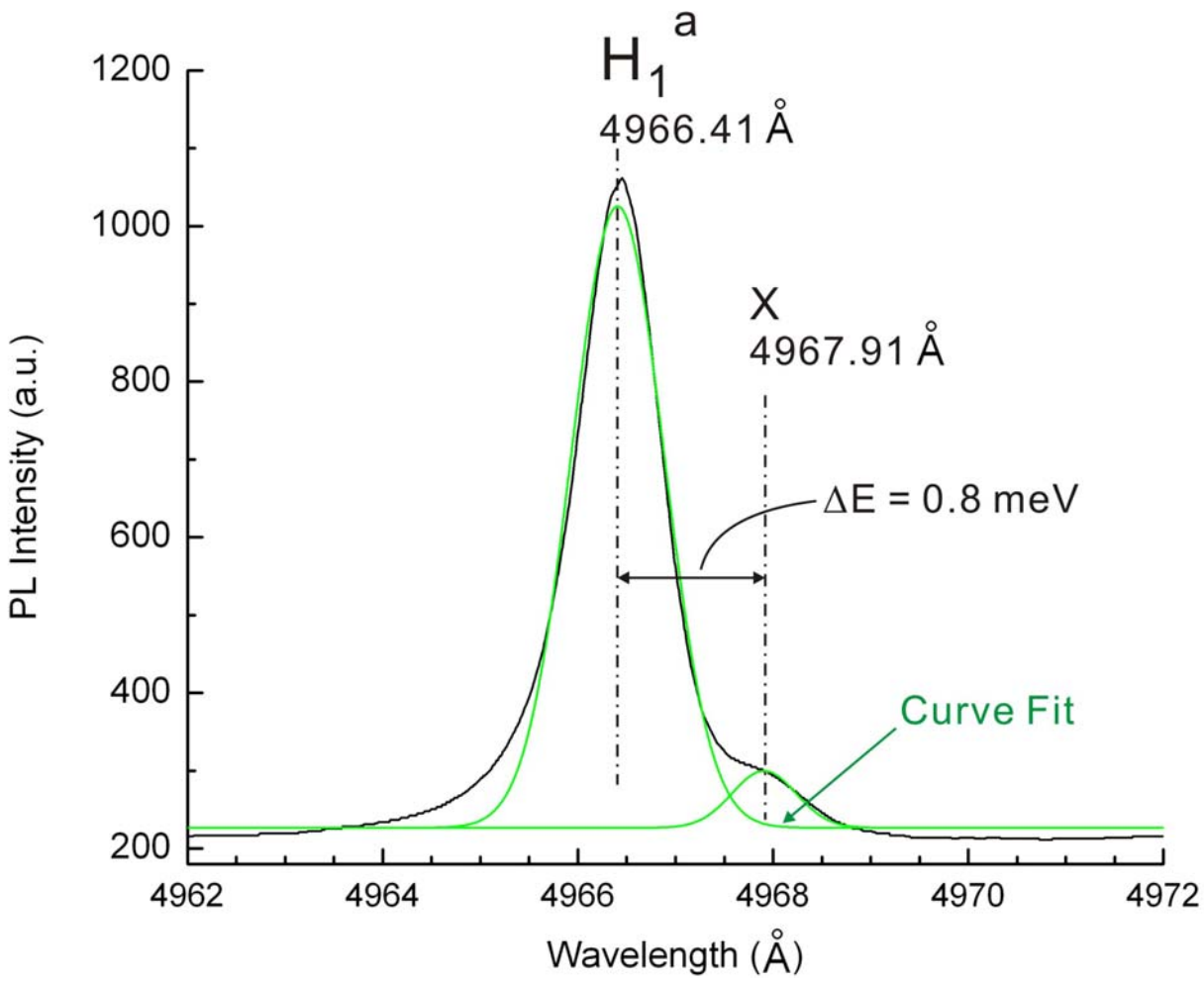

Figure 4.3 Gaussian curve fitting of the high energy local vibrational mode line H_1^a. The black spectrum is the experimental result and the green curves are the fitting results.

4.2 MORSE POTENTIAL CALCULATION

The theoretical calculations show that the high energy local vibration mode can be interpreted as due to the isolated stretching vibration of the C-C dumbbell in the dicarbon antisite $(C_2)_{Si}$. Therefore, we can treat the C-C dumbbell as an anharmonic diatomic configuration using the Morse Potential [42-45], assuming that the interaction from the rest of the lattice can be built into the parameters, which is a rough approximation.

The Morse Potential energy can be written as

$$V(r) = D_e[1 - e^{-\alpha(r-r_0)}]^2 \tag{4.1}$$

where *De* is the depth of the potential well, *r* is the distance between the bonded atoms, r_0 is the equilibrium bond distance, and α is a constant that determines the potential well width. Constant α is connected to the bond constant *k* at the potential minimum through the equation $\alpha = \sqrt{\frac{k}{2D_e}}$, which can be derived by taking the second derivative of *V(r)* evaluating it at $r = r_0$ and setting it equal to bond constant *k*.

The energy levels of the Morse Potential well are given by the following equation:

$$E(n) = \hbar\omega(n + \frac{1}{2}) - \hbar\omega x(n + \frac{1}{2})^2 \tag{4.2}$$

where *n* is the vibration quantum number *n* = 0, 1, 2, …, $\omega = \alpha\left(2D_e / \mu\right)^{1/2}$ is the harmonic vibrational frequency and ωx is the anharmonicity constant with $x = \frac{\hbar\omega}{4D_e} = \hbar\alpha / \left(8D_e\mu\right)^{1/2}$. μ is the reduced mass of these two bonded atoms and $\mu = \frac{m_1 \cdot m_2}{m_1 + m_2}$.

A schematic plot of the Morse Potential with vibration quantum number up to n = 5 is shown in Figure 4.4 .

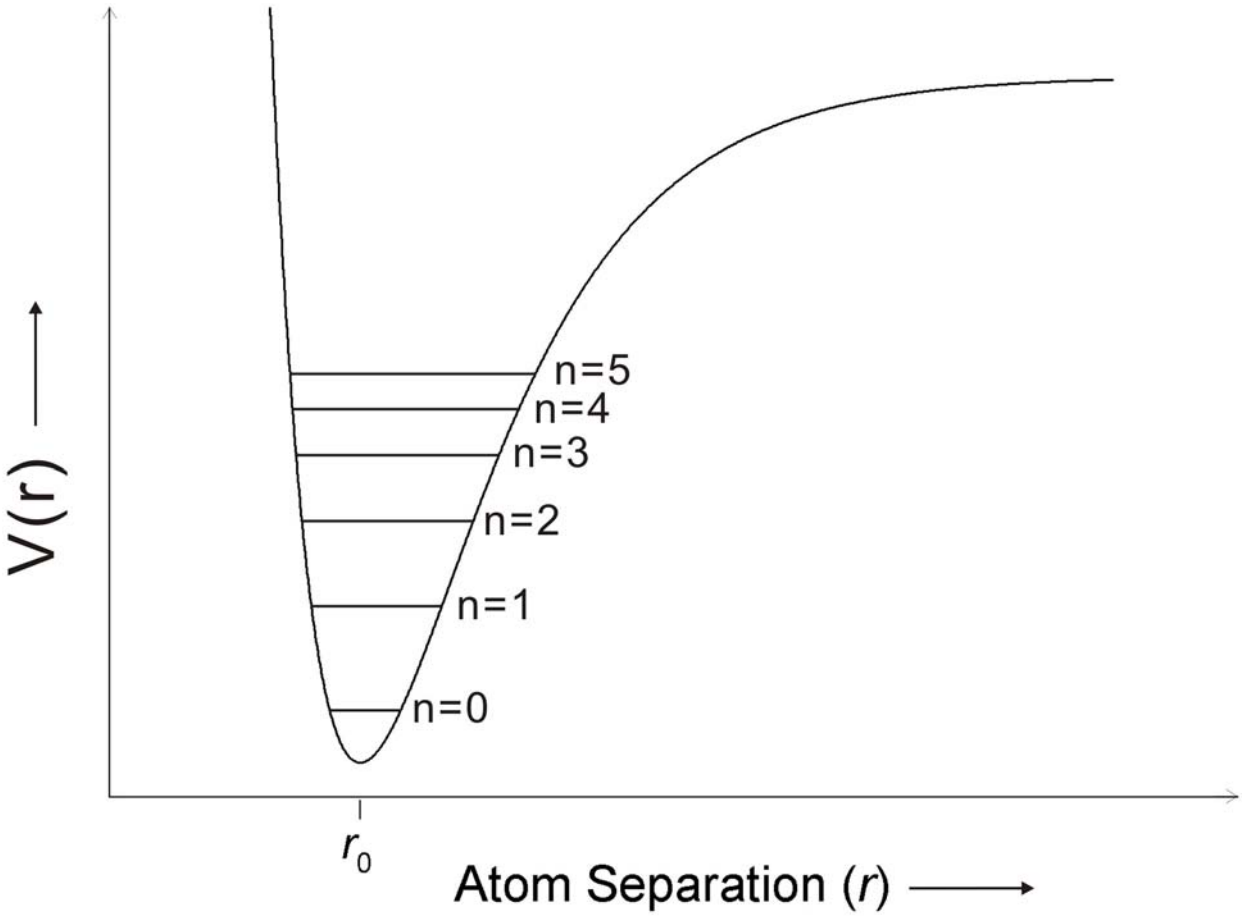

Figure 4.4 A schematic plot of the Morse Potential well with vibration quantum number up to n = 5.

From this energy level equation we can see that the energy spacing between two consecutive energy levels decreases with increasing vibrational quantum number. The extra term of the anharmonicity makes the spacing between the energy levels decrease as the vibration quantum number increases. The energy spacing between the *n*-1 and *n* level is

$$\Delta E_{n,n-1} \equiv E(n) - E(n-1) = \hbar\omega(1-2xn)\,. \tag{4.3}$$

The energies up to the fifth order harmonic are given by the following equations:

$\Delta E_{10} = E(1) - E(0) = \hbar\omega(1-2x)$, $\Delta E_{21} = E(2) - E(1) = \hbar\omega(1-4x)$,

$\Delta E_{32} = E(3) - E(2) = \hbar\omega(1-6x)$, $\Delta E_{43} = E(4) - E(3) = \hbar\omega(1-8x)$,

$\Delta E_{54} = E(5) - E(4) = \hbar\omega(1-10x)$.

From our LTPL spectrum, we have clearly observed the first order and second order vibration modes. Using the energy spacing we can calculate the values of $\hbar\omega$ and x. Then we can put these two values back and calculate the energies of the third, fourth and fifth order vibration modes. If this C-C dumbbell model is correct and the Morse Potential is applicable to this model with our approximation, we should be able to compare the observed experimental third, fourth and fifth order vibration modes with the calculated values. The only problem is when the vibration quantum number increases, the corresponding LTPL peaks become smaller and smaller and eventually not strong enough to be seen in the spectrum. In our careful experiment we were still able to observe up to the fifth harmonic of the high energy local vibrational mode in our experiment, as shown in Figure 4.5. The first line of the triplet is labeled as a_0, where 0 means it is the no phonon line. All the harmonic vibration modes are labeled with corresponding subscripts. Using the experimental energy values of the first two harmonics, we get $\hbar\omega = 182.1$ meV and x = 0.00631521. We can then predict the energies of the higher order harmonics. The results from the Morse Potential predictions and the experimental results from LTPL measurements are all listed in Table 4.2. We can see that they agree with each other very well within an error of less than 1.3 meV up to the fifth harmonic, which is just 0.8% in error.

Table 4.2 A comparison of experiment and Morse Potential predictions for the harmonic energies up to the fifth order of the dicarbon antisite C-C dumbbell vibrations in 4H SiC.

Triplet Line a	ΔE_{10} (meV)	ΔE_{21} (meV)	ΔE_{32} (meV)	ΔE_{43} (meV)	ΔE_{54} (meV)
Experiment	179.8	177.5	175.3	173.7	171.9
Morse Potential Prediction	/	/	175.2	172.9	170.6

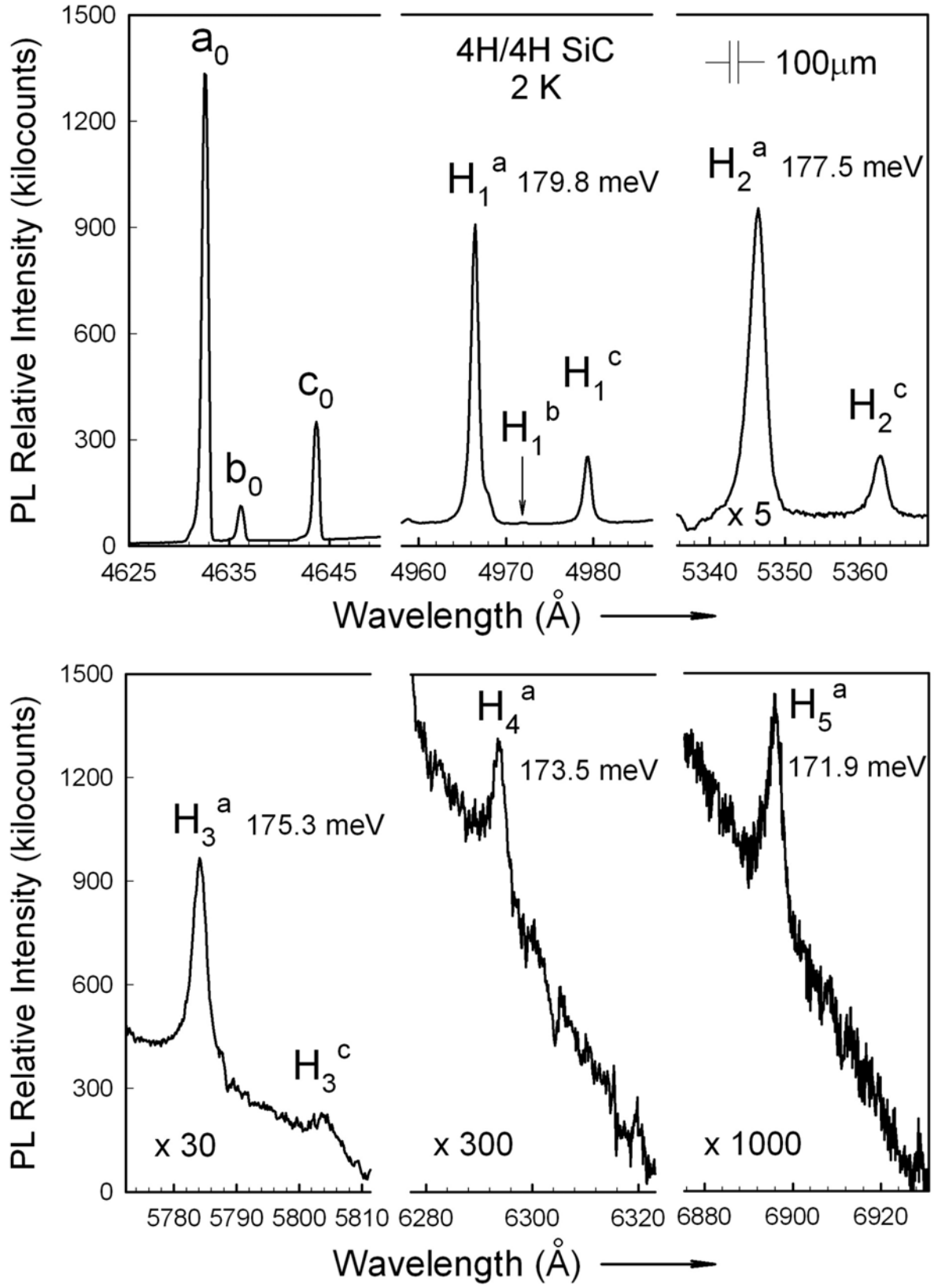

Figure 4.5 Line a_0 of the triplet no phonon lines and its harmonics up to the fifth order.

Table 4.3 shows all the phonon replicas observed for the triplet no phonon lines a_0, b_0 and c_0. ΔE^{ph}_{1-0} is the additional vibrational energy (first vibrational quantum) contributing to the first replica relative to the no phonon line. ΔE^{ph}_{2-1} is the additional vibrational energy (second vibrational quantum) contributing to the second replica relative to the first replica and similarly for ΔE^{ph}_{3-2}, ΔE^{ph}_{4-3} and ΔE^{ph}_{5-4}.

Table 4.3 Dicarbon antisite C-C dumbbell defect center triplet no phonon lines with phonon replicas.

	ΔE^{ph}_{1-0} (meV)	ΔE^{ph}_{2-1} (meV)	ΔE^{ph}_{3-2} (meV)	ΔE^{ph}_{4-3} (meV)	ΔE^{ph}_{5-4} (meV)
a_0 4632.46 Å	179.8	177.5	175.3	173.5	171.9
b_0 4635.79 Å	180.7				
c_0 4643.51 Å	180.0	177.9	175.5		
a_0 4632.46 Å	132.4	132.5			
b_0 4635.79 Å	132.3				
c_0 4643.51 Å	131.4	131.3			
a_0 4632.46 Å	132.4	179.9	177.6	175.0	
c_0 4643.51 Å	131.4	180.0	178.2	175.2	

4.3 FIRST PRINCIPLES CALCULATION ON THE DICARBON ANTISITE DUMBBELL

Our collaborator Dr. Gali calculated the vibrational properties of the dicarbon antisite dumbbell in a large 576-atom supercell using the density functional theory within the local density approximation (LDA). The vibration modes within the quasi-harmonic approximation were calculated as the numerical derivative of the forces. Two different defect-molecule models were used in the calculation of vibration: (a) only C1 and C2 atoms (see Figure 4.6) are allowed to

vibrate; (b) all six carbon atoms from C1 to C6 are allowed to vibrate. The numbering of the carbon atoms is shown in Figure 4.6 with the red arrows indicating the motion of C1 and C2 atoms in the stretch vibration mode.

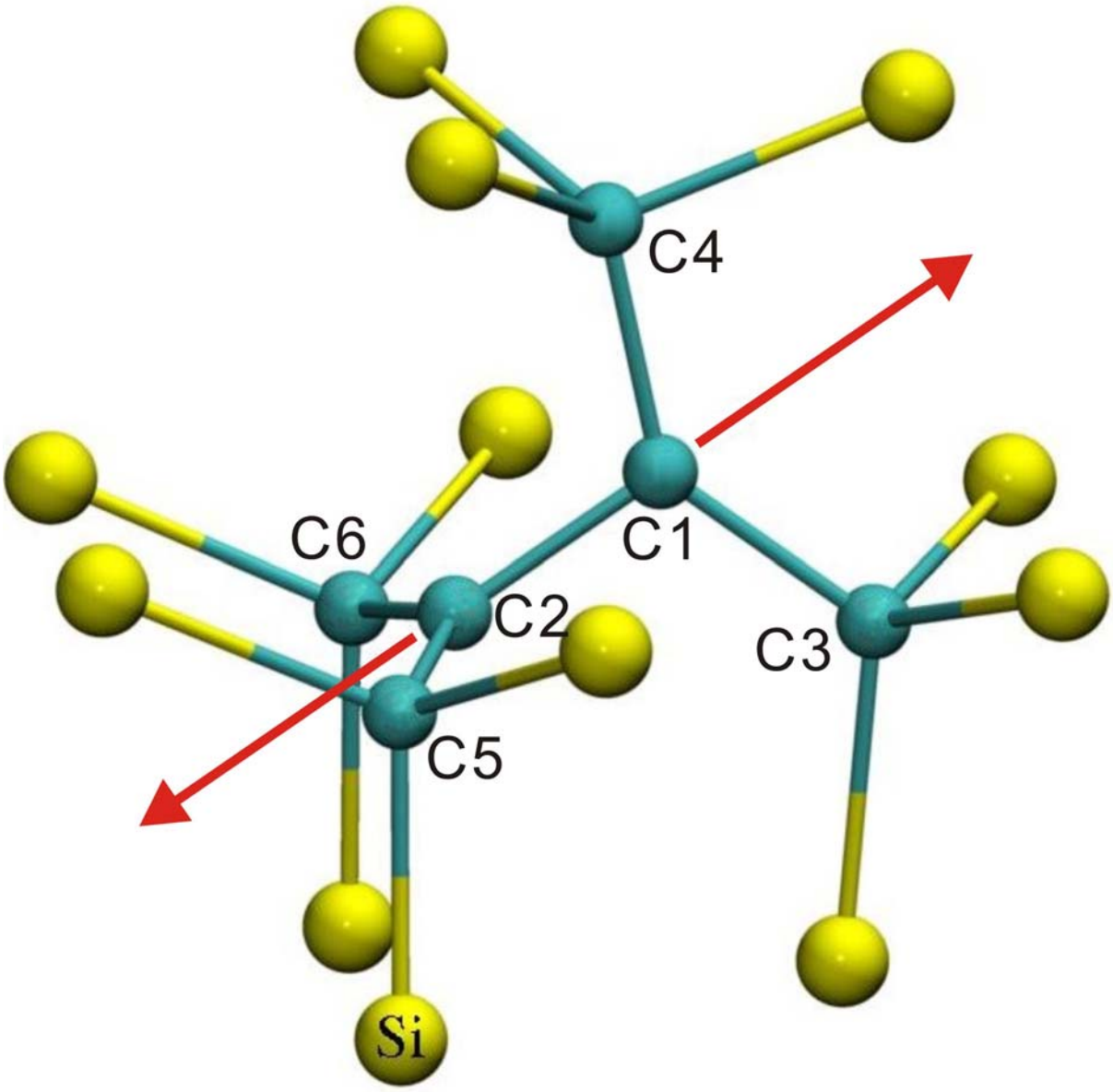

Figure 4.6 Dicarbon antisite defect at the hexagonal site in 4H-SiC. The carbon atoms are labeled by numbers. The arrows indicate the motion of C1 and C2 atoms in the stretch vibration mode.

The calculated stretch mode energy in the case (a) was about 172 meV, which slightly increased to 174 meV in the case (b). In the case (b) we obtained 136 meV for the symmetrically

allowed bending mode that can be tentatively compared to the experimental value of 132 meV. The main reason of the discrepancy between the calculated (174 meV) and measured (~180 meV) stretch modes is likely due to the limitation on the number of atoms that were allowed to vibrate, while the LDA potential energy surface (PES) is sufficiently appropriate. It was found that for both cases (a) and (b) that the normal coordinates of the stretch mode show the motion of C1 and C2 atoms along their bond in the direction of the red arrows in Figure 4.6. This enables a simplification of the description of the stretch mode to a one-dimensional model where only C1 and C2 atoms are moving symmetrically with respect to their bond center by compressing or expanding the bonding distance between them. Calculations at a total of 18 points were done where the maximum compression (expansion) of the bond was about 0.24 (0.36) Å. A very accurate match between the Morse Potential and the calculated first principles data was obtained despite the fact that the Morse Potential contains only two parameters, as shown in Figure 4.7. The units of Hartree and Bohr radius are defined in detail in the next section. This one-dimensional Morse Potential can be applied in the one-dimensional Schrödinger equation where the kinetic energy contains the effective reduced mass (μ) of the vibrating system. If the C1 and C2 atoms are not connected to the rest of the SiC crystal then $\mu = m_C/2$, where m_C is the mass of the ^{12}C isotope. However, μ will be reduced due to the fact that C1 and C2 atoms are bound to the rest of SiC crystal, so $\mu = \chi \cdot m_C/2$ where $\chi<1$. μ was used as a parameter to fit the first transition to the experimental value of 179.8 meV and a value of $\chi \approx 0.9$ was obtained. The one-dimensional Schrödinger equation was solved numerically by applying the corresponding kinetic energy operator and the Morse Potential. The first five transitions were calculated to compare with the experimental results. The anharmonicity reduces the transition energies by about 2.09 meV for each increment in the quantum number of the vibrational states, which agrees nicely

with the experimental value of 2.30 meV. The very nice agreement between experiment and theory further supports the dicarbon antisite model.

The first principles calculations also give the length of the different C-C bonds. The C-C distance between C1-C2 is 1.41 Å. It is 1.50 Å between C1, C2 and their first C neighbors. The next neighbor C-Si bond length is between 1.86 and 1.96 Å.

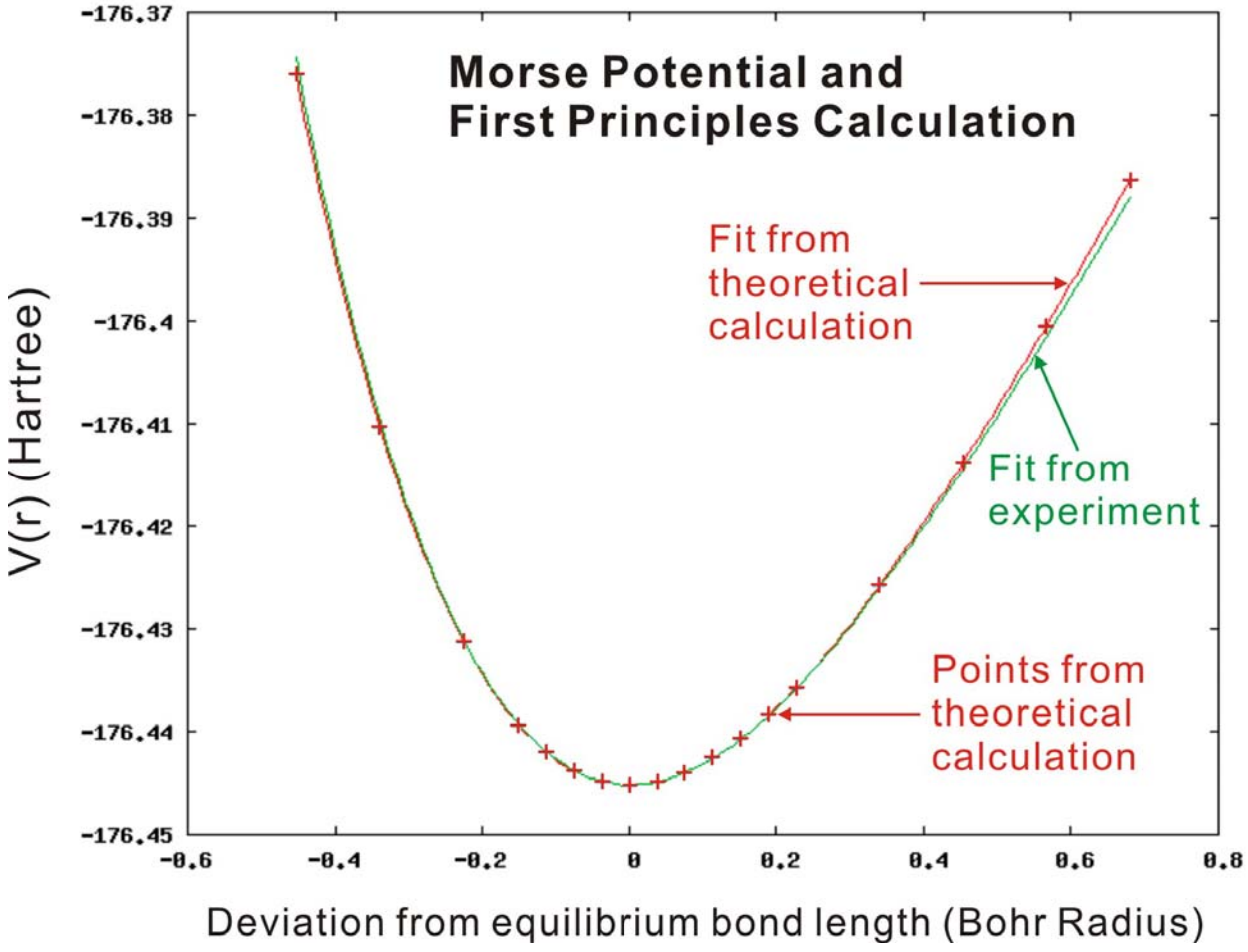

Figure 4.7 Plots of both the Morse Potential fit and the First Principles calculation.

4.4 NUMERICAL SOLUTION TO THE SCHRÖDINGER EQUATION WITH MORSE POTENTIAL

4.4.1 Atomic Units

In general physics, the International System of Units (SI) is widely used with a meter-kilogram-second (MKS) system. But when one wants to do computational calculations, this system will cause some trouble especially when quantum mechanics is involved in the problem. Here are several examples under the standard unit system. The electron rest mass m_e is 9.10938215x10^{-31} kg. The Planck constant h is 6.62606896x10^{-34} J·s. The electron charge e is 1.602176487x10^{-19} C. All these numbers have high orders of magnitude with a +/– sign. During the computational calculations, these will reduce the efficiency of the program because of the high orders of magnitude. Therefore, a so-called Atomic Units system is introduced for which six physical constants are defined as unity and a whole new set of units is given from them. For this part of our problem, I will give some of the physical constants under the atomic units system.

The electron rest mass $m_e = 1$.

The reduced Planck constant $\hbar = 1$.

The electron charge $e = 1$.

The unit of length is called Bohr Radius $a_0 = 1$ (in SI $a_0 = \frac{4\pi\varepsilon_0\hbar^2}{m_e e^2} = 5.291772108\text{x}10^{-11}$ m = 0.529 Å).

The unit of energy is called Hartree E_h = 1 (SI: $E_h = \frac{\hbar^2}{m_e a_0^2}$ = 4.35974417x10^{-18} J = 27.2116 eV).

I will keep the traditional equations in the following text, but I will use the atomic units in my numerical calculations. Atomic units are also used in Dr. Gali's calculations.

From the first principles calculations, Dr. Gali was able to get the reduced mass μ value of 9983.939635 a.u. From the two equations $\omega = \alpha\left(2D_e / \mu\right)^{1/2}$ and $x = \frac{\hbar\omega}{4D_e} = \hbar\alpha / \left(8D_e\mu\right)^{1/2}$, I can calculate the values of D_e and α since we already got $\hbar\omega$ and x from our Morse Potential fitting and reduced mass μ from Dr. Gali. D_e = 7.20878 eV = 0.264916 Hartree and actually doesn't depend on the reduced mass. α = 5.76051x10^{-11} m^{-1} = 0.918628 (Bohr Radius)$^{-1}$.

4.4.2 The Numerov Algorithm

Our model can be treated as a one-dimensional time-independent Schrödinger equation and the deviation from the equilibrium bond length $x = r - r_0$ is the only variable. Let's write the Schrödinger equation as

$$-\frac{\hbar^2}{2\mu}\frac{d^2\varphi(x)}{dx^2} + V(x)\varphi(x) = E\varphi(x) \tag{4.4}$$

We can rewrite it as

$$\varphi''(x) + k^2(x)\varphi(x) = 0 \tag{4.5}$$

where $k^2(x) = \frac{2\mu}{\hbar^2}[E - V(x)]$. Once I put in the atomic units in here, I will set $\hbar$ = 1 and the reduced mass μ will be a simple number. One boundary condition we can think of easily is that the wavefunction $\varphi(x)$ has to go to zero when x goes to infinity.

$$\varphi(x) \to 0, \text{ when } x \to \pm\infty \tag{4.6}$$

We can treat the problem in a region big enough so that we can consider *φ(x)* is already zero at a certain distance. Then we divide this big region into many very small equally spaced segments with a spacing Δx.

We can write the Taylor expansions of the wavefunction:

$$\varphi(x+\Delta x) = \varphi(x) + \Delta x \cdot \varphi'(x) + \frac{\Delta x^2}{2!}\cdot\varphi''(x) + \frac{\Delta x^3}{3!}\cdot\varphi'''(x) + \frac{\Delta x^4}{4!}\cdot\varphi''''(x) + \frac{\Delta x^5}{5!}\cdot\varphi'''''(x) + O(\Delta x^6) \tag{4.7}$$

$$\varphi(x-\Delta x) = \varphi(x) - \Delta x \cdot \varphi'(x) + \frac{\Delta x^2}{2!}\cdot\varphi''(x) - \frac{\Delta x^3}{3!}\cdot\varphi'''(x) + \frac{\Delta x^4}{4!}\cdot\varphi''''(x) - \frac{\Delta x^5}{5!}\cdot\varphi'''''(x) + O(\Delta x^6) \tag{4.8}$$

Add these two equations and the odd power terms cancel out. We get

$$\varphi(x+\Delta x) + \varphi(x-\Delta x) = 2\varphi(x) + \Delta x^2 \cdot \varphi''(x) + \frac{\Delta x^4}{12}\cdot\varphi''''(x) + O(\Delta x^6) \tag{4.9}$$

From Eq. (4.5), we have $\varphi''(x) = -k^2(x)\varphi(x)$. Now we can get the fourth derivative from this equation starting from the third derivative.

$$\varphi'''(x) = -\frac{d}{dx}[k^2(x)\varphi(x)] = -\frac{k^2(x+\Delta x)\varphi(x+\Delta x) - k^2(x)\varphi(x)}{\Delta x} \tag{4.10}$$

$$\begin{aligned}
\varphi''''(x) &= -\frac{d^2}{dx^2}[k^2(x)\varphi(x)] \\
&= -\frac{1}{\Delta x^2}\{[k^2(x+\Delta x)\varphi(x+\Delta x) - k^2(x)\varphi(x)] - [k^2(x)\varphi(x) - k^2(x-\Delta x)\varphi(x-\Delta x)]\} \\
&= -\frac{1}{\Delta x^2}[k^2(x+\Delta x)\varphi(x+\Delta x) + k^2(x-\Delta x)\varphi(x-\Delta x) - 2k^2(x)\varphi(x)]
\end{aligned} \tag{4.11}$$

Substitute Eqs. (4.5) and (4.11) into Eq. (4.9) and we get

$$\begin{aligned}
&\varphi(x+\Delta x) + \varphi(x-\Delta x) = 2\varphi(x) + \Delta x^2 \cdot [-k^2(x)\varphi(x)] \\
&+ \frac{\Delta x^4}{12}\cdot\{-\frac{1}{\Delta x^2}[k^2(x+\Delta x)\varphi(x+\Delta x) + k^2(x-\Delta x)\varphi(x-\Delta x) - 2k^2(x)\varphi(x)]\} + O(\Delta x^6)
\end{aligned} \tag{4.12}$$

Re-arrange the equation and we get

$$\varphi(x+\Delta x)=\frac{2[1-\frac{5}{12}\Delta x^2\cdot k^2(x)]\varphi(x)-[1+\frac{1}{12}\Delta x^2\cdot k^2(x-\Delta x)]\varphi(x-\Delta x)}{1+\frac{1}{12}\Delta x^2\cdot k^2(x+\Delta x)}+O(\Delta x^6) \quad (4.13)$$

From this equation, we can see that once we set the initial values of the first two wavefunction points, we can calculate all the rest of the wavefunction points. We can also see that this equation gives a high accuracy with an order of Δx^6, where Δx itself is a very small constant and the power of 6 only makes it much smaller.

This is the key of the Numerov Algorithm and is widely used for numerically solving the second order ordinary differential equations, such as the Schrödinger equation here and the Poisson equation. It has been discussed in extensive details in some computational physics books, such as "*An Introduction to Computational Physics*" by Tao Pang [46] and "*Quantum Mechanics: Concepts and Applications*" by Nouredine Zettili [47]. These books also have examples of the programs written in C++, which can be applied to the actual problems after making the appropriate adjustments.

4.4.3 Numerical Calculation Results

After applying the parameters we got in section 4.4.1, we can solve the Schrödinger equation numerically for the dicarbon antisite dumbbell model. Figure 4.9 (a) shows the profile of the given Morse Potential obtained during the numerical calculation simultaneously. Figure 4.9 (b) shows the wavefunctions for different vibrational states to the fifth excited state. The corresponding energy eigenvalues for these vibrational states are $3.3354\text{x}10^{-3}$, $9.9430\text{x}10^{-3}$, 0.0165, 0.0229, 0.0293 and 0.0355 in the unit of Hartree. They are also plotted in Figure 4.9 (a). Convert them to the unit of meV and we get 90.7629, 270.5637, 448.0645, 623.2652, 796.1659

and 966.7667. The transition energies between two consecutive states are 179.8008, 177.5008, 175.2007, 172.9007 and 170.6008 meV. The anharmonicity difference between these transition energies is about 2.30 meV. This is slightly different from the 2.09 meV calculated by Dr. Gali, which is coming from his potential energy surface calculation. In the Morse Potential fitting section, my original fitting gives $\hbar\omega$ = 182.1 meV and x = 0.00631521. The anharmonicity factor should be $\hbar\omega \cdot (2x)$ = 2.30 meV, which is a perfect match to my numerical calculation result. So I am self-consistent with myself. More importantly, this match further confirms the reduced mass value calculated by Dr. Gali from the potential energy surface method.

From quantum mechanics, we know that the probability density $P_n(x) = |\varphi_n(x)|^2$. Therefore, we can plot the probability densities for different vibrational states to the fifth excited state, which are shown in Figure 4.9 (a). They are converted into a probability density map at different energy levels. Figure 4.9 (b) shows the map along with the potential well. The color scale is shown on the right side. Blue color represents very small probability density, while red color represents big probability density. From this map, we can clearly see that the anharmonic shape of the distribution and the places with high probability densities are near the both sides of the potential well, which is similar to what we have learned from the harmonic oscillator case in quantum mechanics.

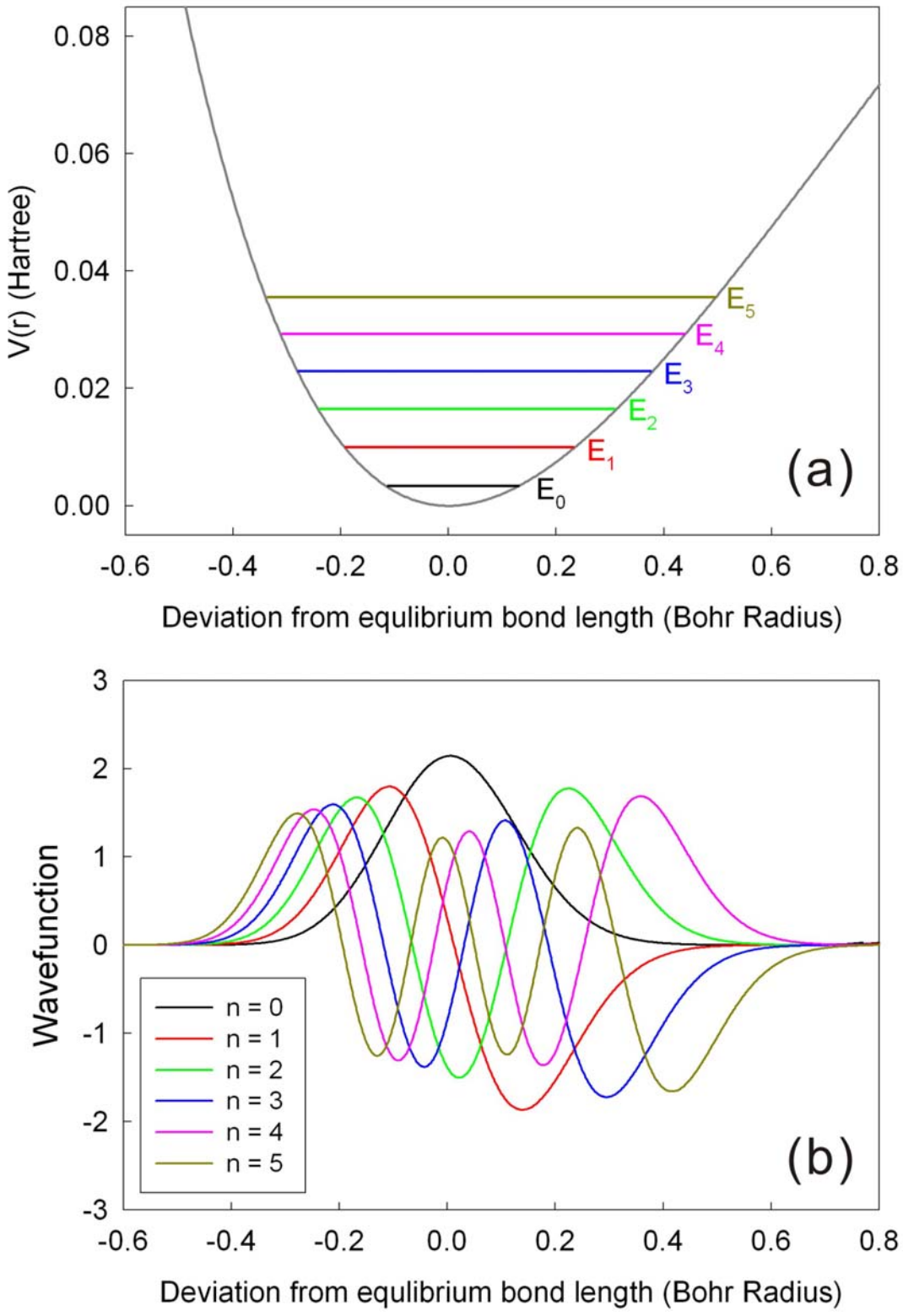

Figure 4.8 (a) The calculated Morse Potential profile with energy levels of different vibrational states. (b) Plots of the corresponding wavefunctions from the ground state up to the fifth excited states.

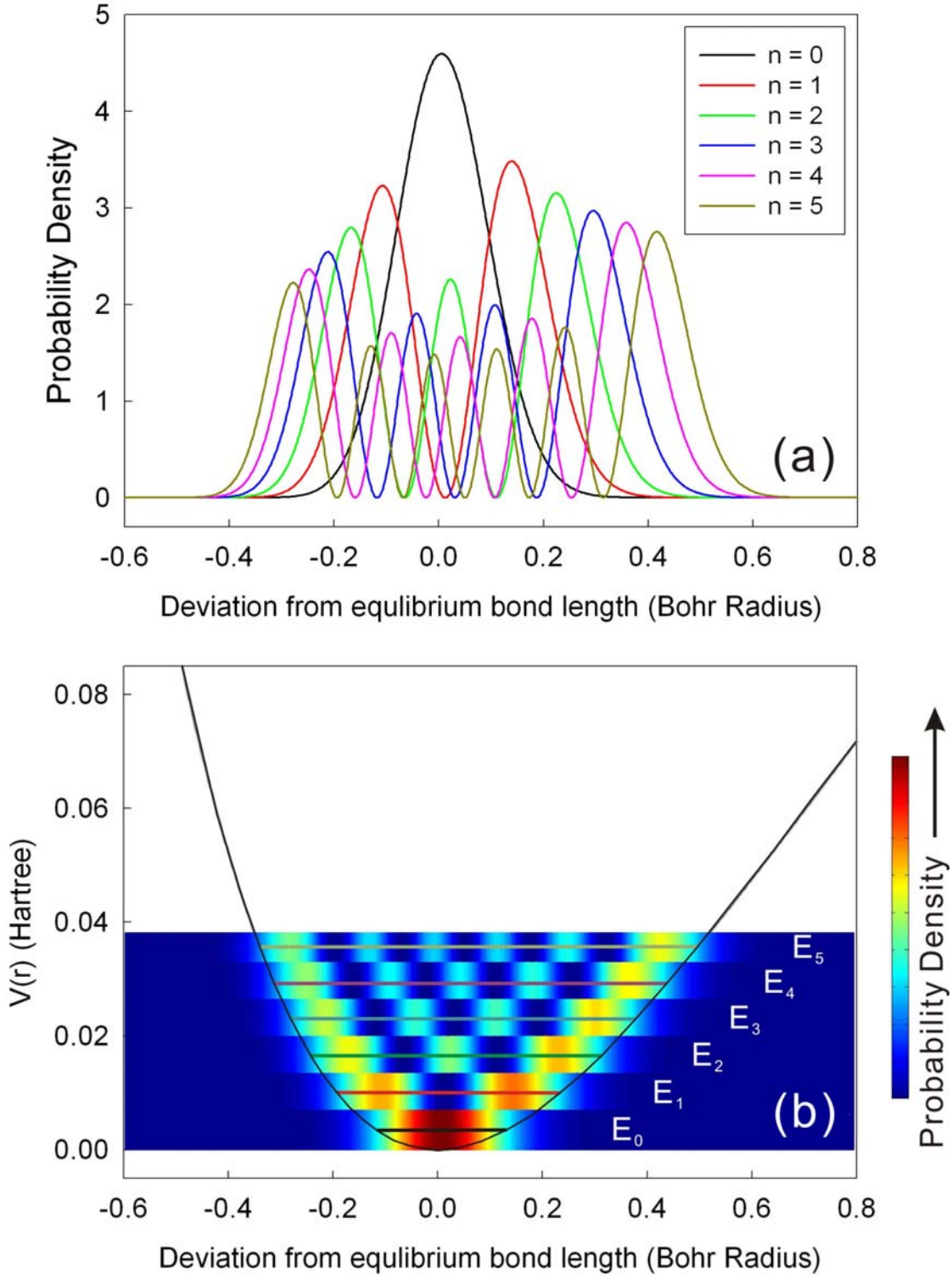

Figure 4.9 (a) Plots of the probability densities from the ground state up to the fifth excited states. (b) Map of the probability densities converted from the plots in (a).

4.5 OTHER DICARBON ANTISITE DEFECT LINES OBSERVED IN LTPL

In addition to the previously observed no phonon lines a_0, b_0 and c_0 we observe a number of new lines E_0, F_0, θ_0, Φ_0, K_0, G_0, J_0, and M_0 as shown in Figure 4.10. The triplet no phonon lines are plotted next to them for intensity comparison. It is clear that those new lines are relatively weak, but they are all reproducible in different samples after both electron irradiation and ion implantation. They all annealed out together between 1300 °C and 1400 °C. This is evidence that the lines are not impurity related and are due to the same or perhaps very similar intrinsic defect center.

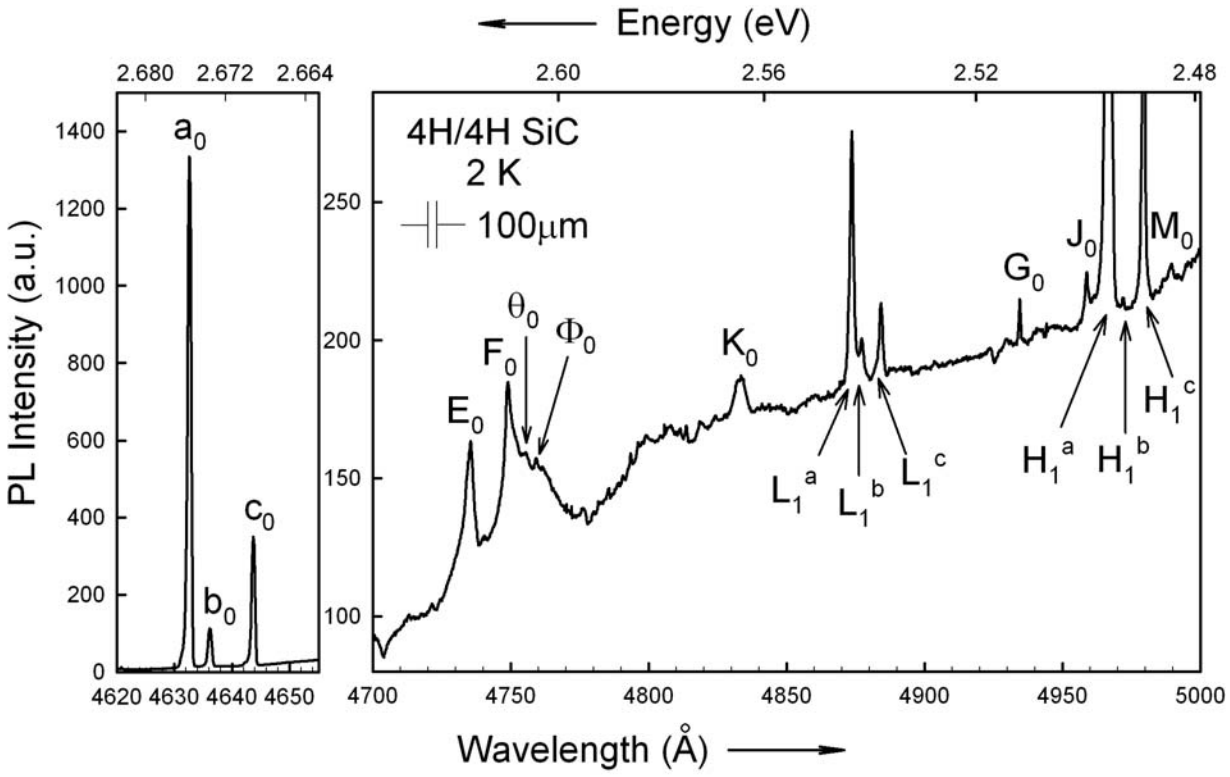

Figure 4.10 Other lines of the dicarbon antisite C-C dumbbell center from 4H SiC irradiated by 1 MeV electrons with a fluence of $1x10^{15}$ cm^{-2}.

Table 4.4 Other dumbbell lines with phonon replicas, excluding the triplet a_0, b_0 and c_0.

Defect Lines	E_0	F_0	θ_0	Φ_0	K_0	G_0	J_0	M_0
Wave-length (Å)	4735.39	4748.71	4755.55	4759.23	4833.06	4934.29	4958.81	4989.32
ΔE^{ph}_{1-0} (meV)	179.5	180.2	179.1	180.2	179.8	169.6	132.3	179.0
ΔE^{ph}_{2-1} (meV)	177.7	177.8				169.2		

In Table 4.4 we also show the observed phonon replicas for these new lines. Line G_0 deviates from the normal pattern of phonon mode replica energies but that doesn't rule out that it might be a variant of the proposed carbon dumbbell center. Since the 169 meV local vibrational mode of G line is really close to the 165 meV frequency of diamond [16], we can speculate that it might have something to do with the dicarbon antisite with the surrounding four carbon atoms. The interaction between one of the two carbon antisite atoms with one of the four nearest carbon neighbors is similar to the carbon-carbon interaction in the diamond, except that the bond length and stiffness are changed due to difference between the SiC unit cell and the diamond unit cell in addition to the two carbon atoms squeezed into one Si site.

At this point, we cannot make the statement that these new lines are additional no phonon lines from the dicarbon antisite, even though they have phonon replica energies similar to the triplet lines. It is still possible that these new lines are also phonon replicas from the triplet a_0, b_0 and c_0 lines with different replica energies. In order to clear up this, a photoluminescence excitation (PLE) spectroscopy experiment has to be done. A collaboration is currently being scheduled with Dr. Ivan Ivanov at Linköping University in Sweden for the PLE study.

4.6 MONTE CARLO SIMULATION OF THE DAMAGE DISTRIBUTION

In Ref. [11, 12] the authors claim that the electron beam fluences used were either 10^{20} cm^{-2} or high 10^{19} cm^{-2}. Our experiments have shown that under such conditions the samples are irreversibly rendered amorphous. We have used fluences of $5x10^{16}$ cm^{-2}. So how can we reconcile this discrepancy? Steeds also reports that, using a He-Cd laser at 325 nm, he was only able to observe this triplet system at considerable distance from the central axis and beyond the irradiation profile of the TEM beam diameter of 100 μm or 200 μm. He had no explanation for this mysterious phenomenon. We believe that if one assumes that the 325 nm laser penetrates 10 to 20 μm from the surface one can explain his results due to the tremendous scattering of the 170 keV electron beam in the SiC lattice. Although Steeds claims his TEM electron beam has a sharp cutoff at the perimeter, this is only true before the electrons get into the SiC material. Once the electrons have penetrated into the sample, they will travel not only in the forward direction but also laterally because of the scattering with the SiC lattice. Therefore there is a significant irradiated volume outside of the initial beam area. However, the electron fluence recedes as one goes further away from the TEM beam profile. In the next paragraph we give results of an electron simulation of a 170 keV electron beam entering a SiC crystal again using the simulation program CASINO [37].

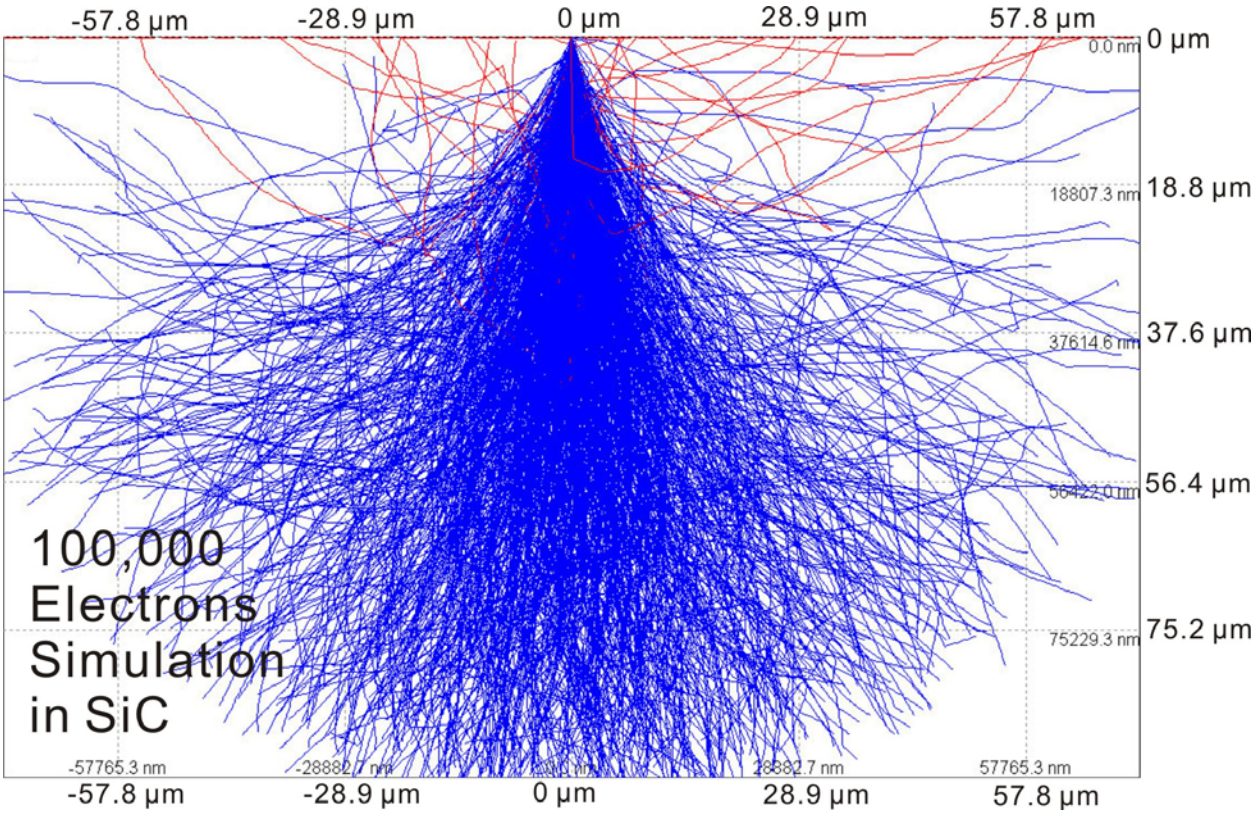

Figure 4.11 Simulated penetration trajectories of 100,000 electrons inside SiC for 170 keV electrons. The incident electron beam has a diameter of 10 nm.

Figure 4.11 is a trajectory simulation of 100,000 electrons with an energy of 170 keV going into SiC. The blue lines are the electrons which are still inside the SiC and stop at 100 keV, which is the threshold to displace any atoms. The red lines are the electrons which escape from the sample surface. From this figure, we can see that 20 µm away from the edge of the TEM beam and at a depth of 20 µm, there are many trajectories spreading perpendicular to the original beam direction. We can do a rough estimate here. At a distance of 20 µm from the edge of the TEM beam and at a depth of 20 µm from the surface we estimate the electron fluence to be approximately four orders of magnitude smaller than the incident beam. If the incoming beam fluence is 10^{20} cm^{-2}, our estimate of the effective electron fluence at 20 µm from the edge of the TEM beam is between 10^{15} cm^{-2} to 10^{16} cm^{-2}, which is exactly what we used in our own electron

irradiation experiments. Hence, there are regions outside of the central beam which are irradiated by electrons but at a reduced fluence. This makes the Steeds result of observing the triplet lines well beyond the confines of the TEM beam very plausible.

4.7 UNUSUAL ANNEALING BEHAVIOR OF THE DICARBON ANTISITE DEFECT LINES

Another thing we have observed is a startling re-appearance of all the dicarbon antisite defect lines subsequent to a re-heating of the samples at 1100 °C after they have been annealed out at 1400 °C. We have done the annealing on many samples in our own ceramic tube furnace and these triplet lines are always annealed out between 1300 °C and 1400 °C. We sent these samples to our collaborator Dr. Pensl at the University of Erlangen for the DLTS measurement. They processed the 1400 °C annealed samples in their graphite furnace and re-heated them at 1100 °C again. When we got them back, we checked them with LTPL and we were very surprised to see that these lines re-emerged. We have noticed that the re-emergence appears only after the sample has been processed in the graphite furnace at the University of Erlangen. We have done the 1400 °C annealing and subsequent heating at 1100 °C all in our own ceramic tube furnace, but we do not see the re-appearance of the triplets. This suggests that the furniture in the Erlangen annealing furnace has a profound effect on this defect system. Since the atomic model of this particular defect is a dicarbon antisite, the additional carbon atoms available in the graphite furnace might be the key to the reappearance of the defect lines.

5.0 D_I DEEP DEFECT IN N-TYPE AND P-TYPE 4H SILICON CARBIDE

5.1 EXPERIMENT PROCEDURES

In order to give a clear answer to this controversy of the D_I center summarized in Chapter 2, we decided to do a systematic study on the defect centers in electron irradiated 4H SiC. We used electron irradiation to create the damage because it is a clean way to create the deep centers without introducing other impurities. In order to see if there is any correlation between the D_I center in LTPL and the Z_1/Z_2 center in DLTS, we tried the n-type 4H SiC first. We then repeated the same procedures on p-type 4H SiC so that we can check the HS1 defect, which can be detected by DLTS only in the p-type material.

The CVD growth and electron irradiation have been presented in the experimental techniques chapter. Prior to the electron irradiation, DLTS was done on these samples to make sure they have a DLTS background of $5x10^{11}$ cm^{-3}. This is two orders of magnitude lower than DLTS backgrounds found in ordinary materials. We have tried with several different growth groups and Prof. Kimito's group was the only place where such a low deep defect background could be obtained. This ensures that we are starting with samples which don't have the background to interfere with the deep defects we are going to create using electron irradiation. We cut the wafer into many 3mm x 5mm pieces and checked all of them with LTPL. Some of the pieces contain polytype inclusions and were ruled out.

We did the LTPL and DLTS measurements on samples annealed at different temperatures to check if there is any correlation between the defect centers observed using these two different characterization techniques.

5.2 EXPERIMENTAL RESULTS FROM LTPL AND DLTS ON ELECTRON IRRADIATED N-TYPE 4H SILICON CARBIDE

In LTPL it is not possible to determine the absolute concentration of certain defects without using other measurement techniques for calibration. People have developed a method to determine the concentration of the nitrogen from the LTPL spectra, but capacitance-voltage (*C-V*) measurement and secondary ion mass spectrometry (SIMS) were used to find the correct doping as a calibration, then an extrapolation was made [2-4, 6].

However, a qualitative result with small relative errors can be determined by taking the intensity ratio of the defect line with a line corresponding to an impurity which is expected to have a constant concentration in all samples. In our experiment, the electron bombardment lattice damage is sufficiently small so that the no phonon nitrogen Q_0 line at 3821 Å in n-type 4H SiC remains almost constant as samples are annealed from room temperature to 1700 °C. Consequently, we use Q_0 as a standard and take ratios of peak heights of a desired defect line to the Q_0 line at each anneal temperature in n-type 4H SiC. We can use the variation of this intensity ratio as a tool to study the concentration of the desired defect center. Figure 5.1 shows an example of these particular two lines from an n-type 4H SiC sample which was irradiated by 1 MeV electrons and annealed at 1300 °C. Table 5.1 lists all the L_1 to Q_0 ratios from both 170 keV and 1 MeV irradiated n-type samples after different annealing.

Table 5.1 Intensity ratios of L_1 to the nitrogen no phonon line Q_0 from n-type samples after electron irradiation and annealing.

Annealing Temperature (°C)	L_1/Q_0 Intensity Ratio	
	170 keV	1 MeV
900	0.0113	0.1302
1000	0.0153	0.1224
1100	0.0109	0.1338
1200	9.1582×10^{-3}	0.1264
1300	7.1276×10^{-3}	0.1614
1400	7.3890×10^{-3}	0.1912
1500	0.0157	0.1928
1600	0.0866	0.2488
1700	0.2916	1.0890

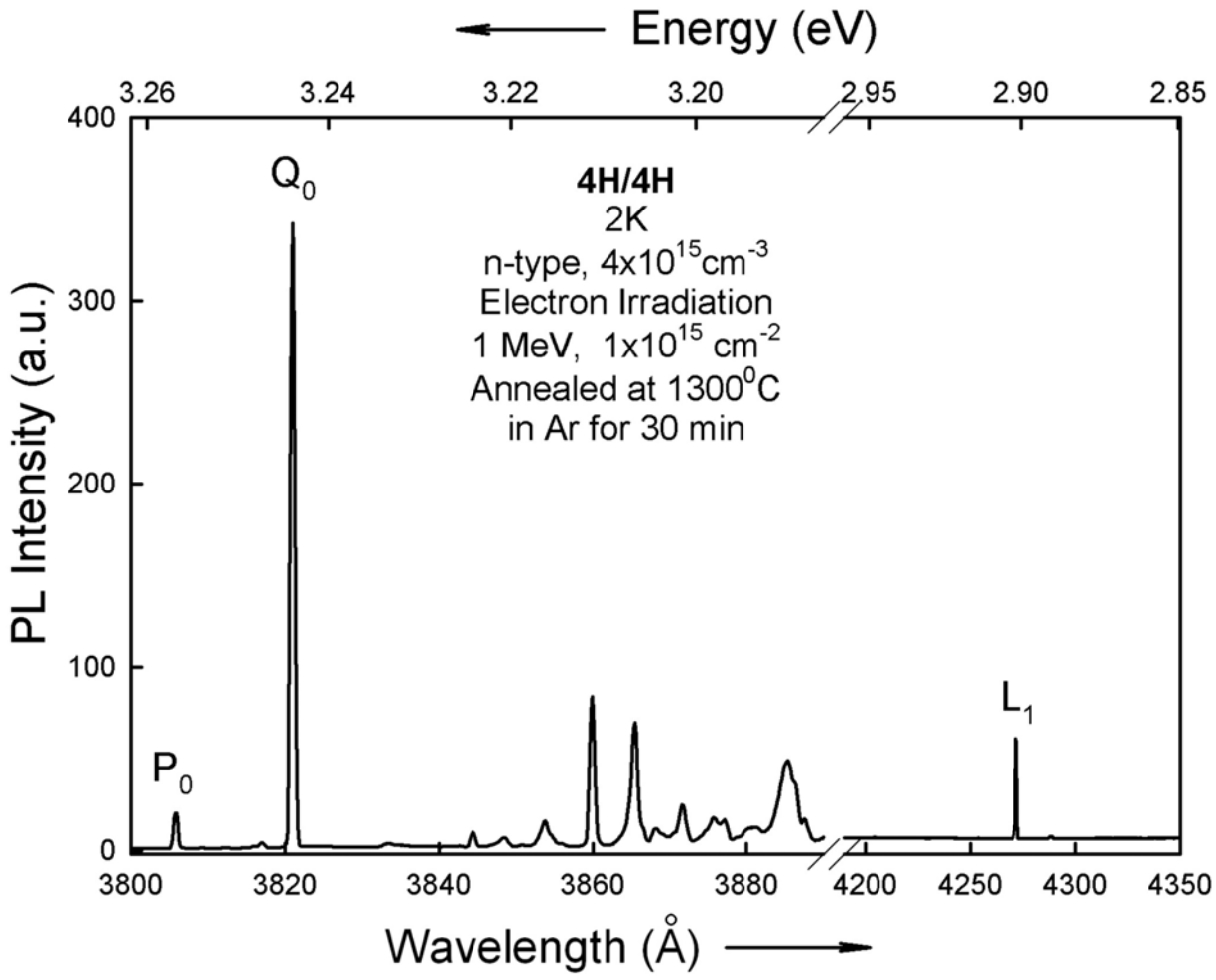

Figure 5.1 One LTPL example from a 1 MeV electron irradiated and 1300 °C annealed n-type 4H SiC sample showing both the D_I no phonon line L_1 and the nitrogen bound exciton no phonon line Q_0. The intensity ratio of these two is used to monitor the concentration change of the D_I center in all the samples during the different temperature annealing.

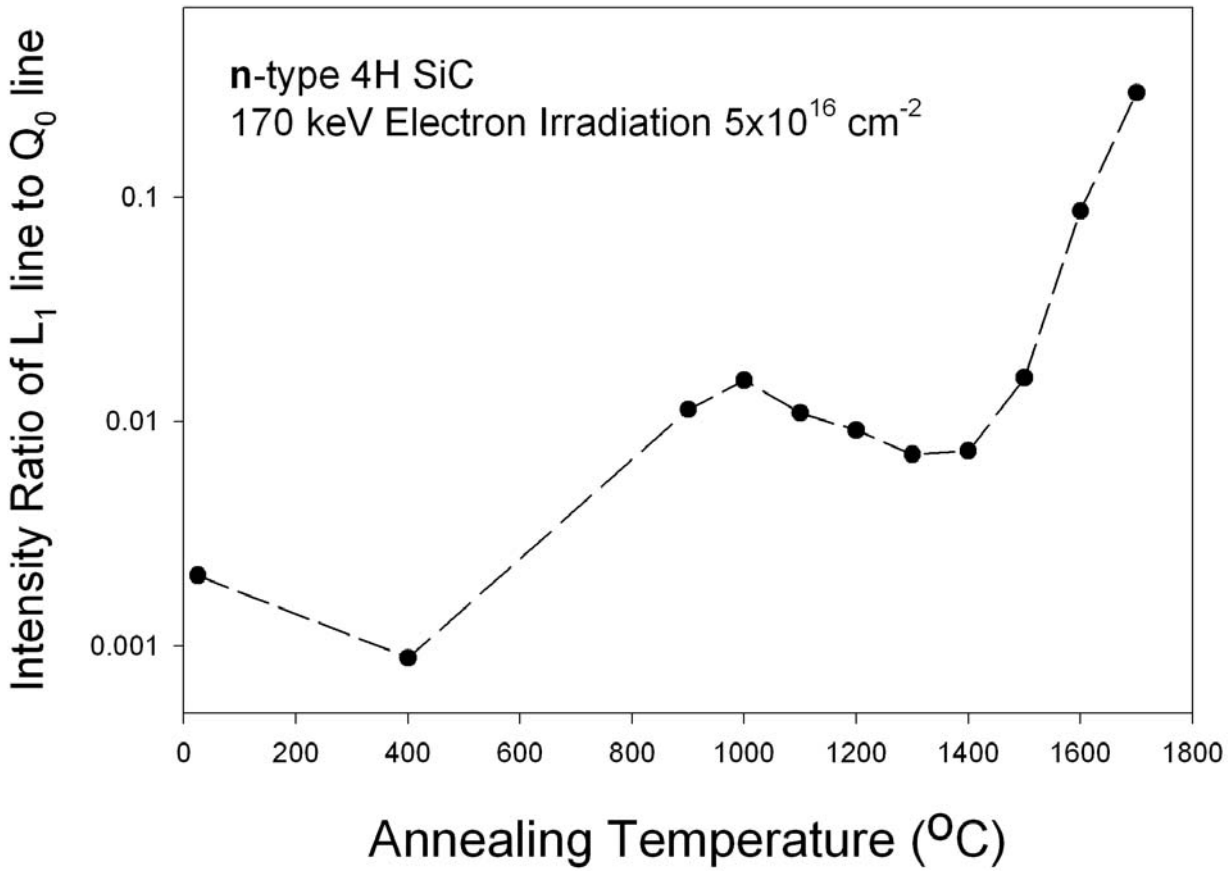

Figure 5.2 The annealing temperature dependence of the intensity ratio of L_1/Q_0 from n-type 4H SiC which has been irradiated with 170 keV electrons. Note the intensity ratio is plotted in semi-logarithmic scale.

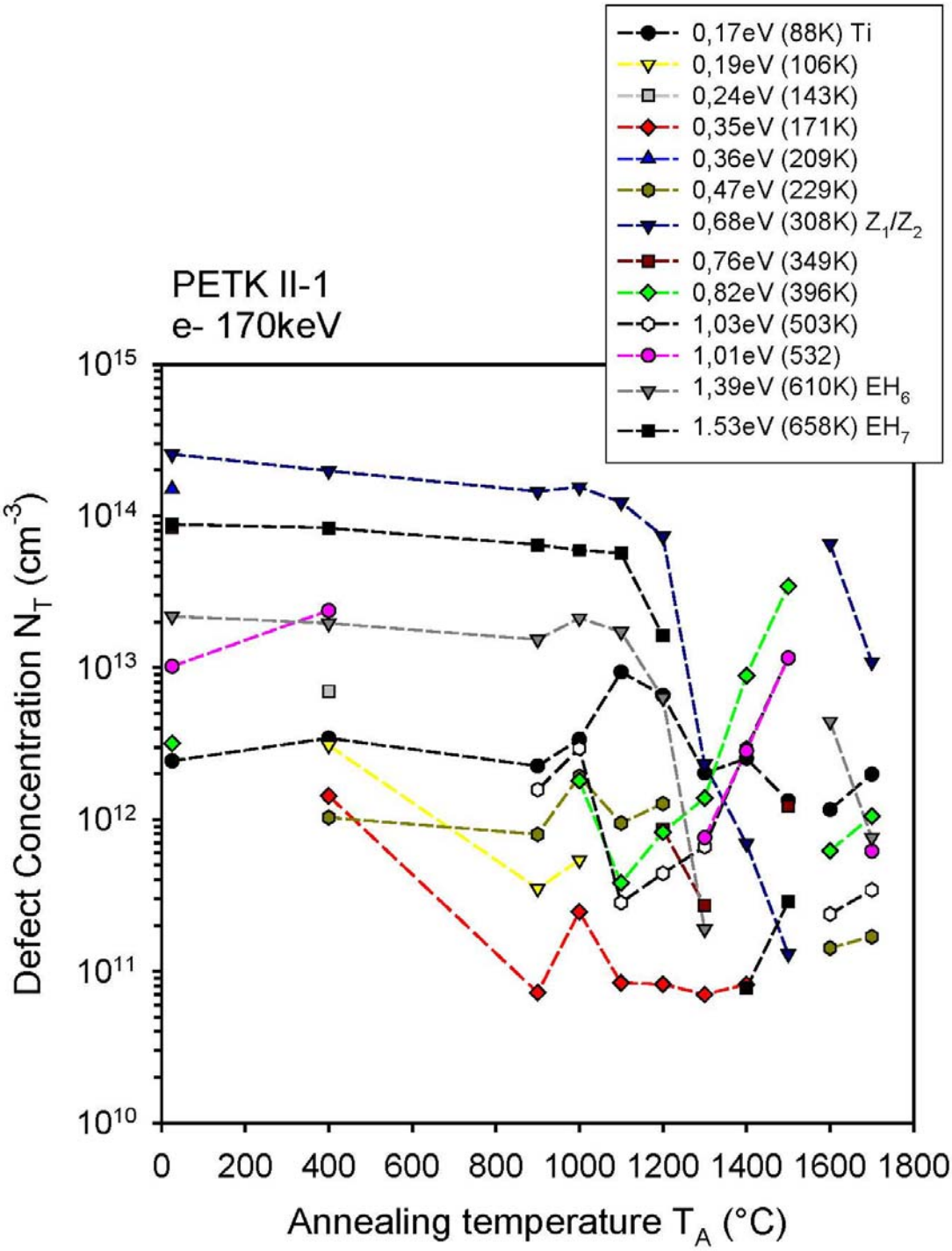

Figure 5.3 The annealing temperature dependence of all the defect centers detected by DLTS from n-type 4H SiC which has been irradiated with 170 keV electrons. The blue triangle represents the particular Z_1/Z_2 center which we are trying to correlate to the L_1 line from the D_I center in LTPL.

Figure 5.2 shows the annealing temperature dependence of the intensity ratio of L_1/Q_0 from n-type 4H SiC which has been irradiated by 170 keV electrons. The intensity ratio of L_1/Q_0 after annealing at 900 °C is about one order of magnitude higher than that from non-annealed samples. L_1 does not further increase very much until we reach 1500 °C and then increases from 1500 °C to 1700 °C. In the DLTS results in Figure 5.3, the concentration of the Z_1/Z_2 center is plotted with blue triangles and shown to be roughly constant until 1200 °C annealing. It then drops three orders of magnitude from 1200 °C to 1500 °C. The Z_1/Z_2 concentration appears to recover after annealing to 1600 °C but then anneals out at 1700 °C. What is striking is that we don't see any direct correlation between the D_I center in LTPL and the Z_1/Z_2 center in DLTS.

One may notice that these is a discontinuity between 1500 °C and 1600 °C. We have a possible explanation for this discontinuity. The n-type sample annealing below and including 1500 °C was done in our ceramic tube furnace which can only go up to 1500 °C. For annealing at higher temperatures, we had to send the samples to our collaborator at the University of Erlangen. They have a graphite furnace which can handle the 1600 °C and 1700 °C annealing. Therefore, this discontinuity between 1500 °C and 1600 °C might come from the different annealing environment in two different kinds of furnaces. Anyway, if we compare the evolution of the L_1/Q_0 intensity ratio and the Z_1/Z_2 center concentration, we just simply can not see any direct correlation between these two.

We can compare the L_1/Q_0 intensity ratio and the Z_1/Z_2 center concentration from the 1 MeV irradiated n-type 4H SiC, as shown in Figure 5.4 and Figure 5.5, respectively. We still can not find any similarity between these two figures.

Our conclusion from the work done in this section is that we don't see any direct correlation between the D_I center in LTPL and the Z_1/Z_2 center in DLTS in n-type 4H SiC.

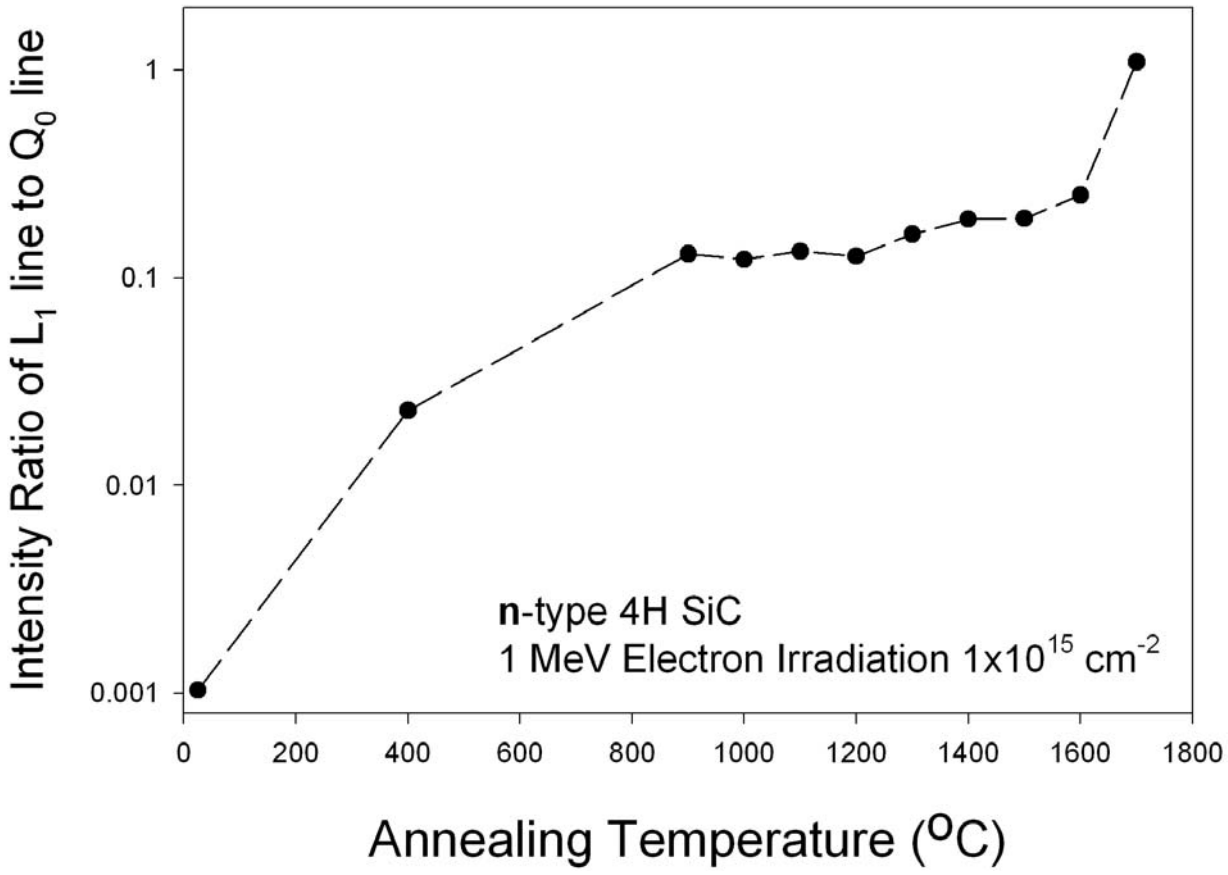

Figure 5.4 The annealing temperature dependence of the intensity ratio of L_1/Q_0 from n-type 4H SiC which has been irradiated with 1 MeV electrons. Note the intensity ratio is plotted in semi-logarithmic scale.

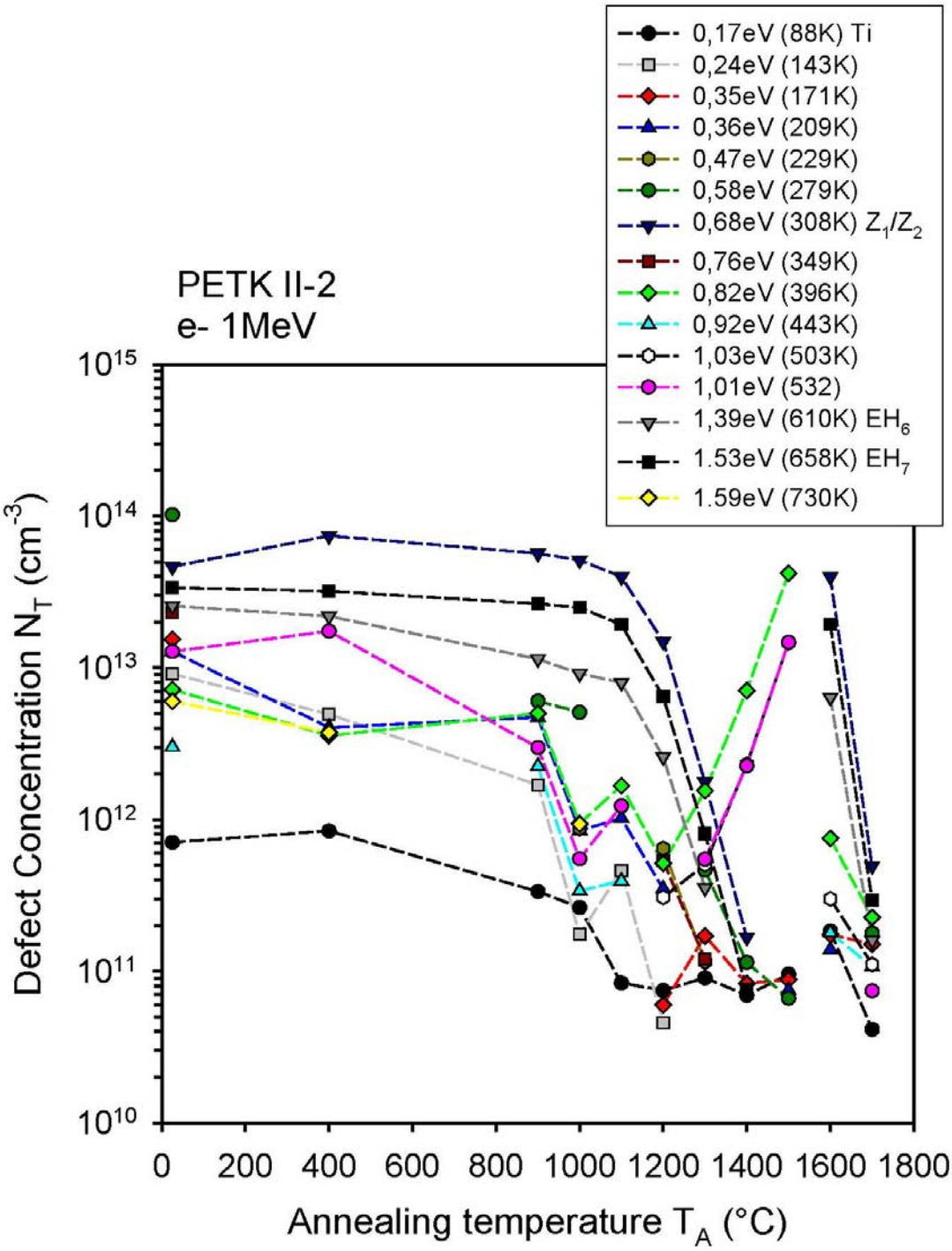

Figure 5.5 The annealing temperature dependence of all the defect centers detected by DLTS from n-type 4H SiC which has been irradiated with 1 MeV electrons. The blue triangle represents the particular Z_1/Z_2 center which we are trying to correlate to the L_1 line from the D_I center in LTPL.

5.3 EXPERIMENTAL RESULTS FROM LTPL AND DLTS ON ELECTRON IRRADIATED P-TYPE 4H SILICON CARBIDE

In October 2007 there was an International Conference of Silicon Carbide and Related Materials (ICSCRM) in Otsu, Japan. All the collaborators in this project including some theorists gathered together and had a small meeting. People went through all the data from the n-type 4H SiC material and agreed that if the pseudodonor model [30] is correct, we should be able to see a clear correlation between the D_I center and the HS1 center from the same experiments on p-type 4H SiC. Therefore, after this meeting the collaborating team started the whole procedure again on p-type 4H SiC, including thin film growth, electron irradiation, annealing, LTPL and DLTS.

Similar to the study on n-type samples, for p-type 4H SiC, we assume that the aluminum concentration in all these samples is the same. Then we can use the ratio of the intensity of the L_1 line and the strongest aluminum bound exciton no phonon line at 3815 Å to monitor the concentration change of the D_I center. Figure 5.6 shows an example from an n-type 4H SiC sample which was irradiated by 170 keV electrons and annealed at 1300 °C.

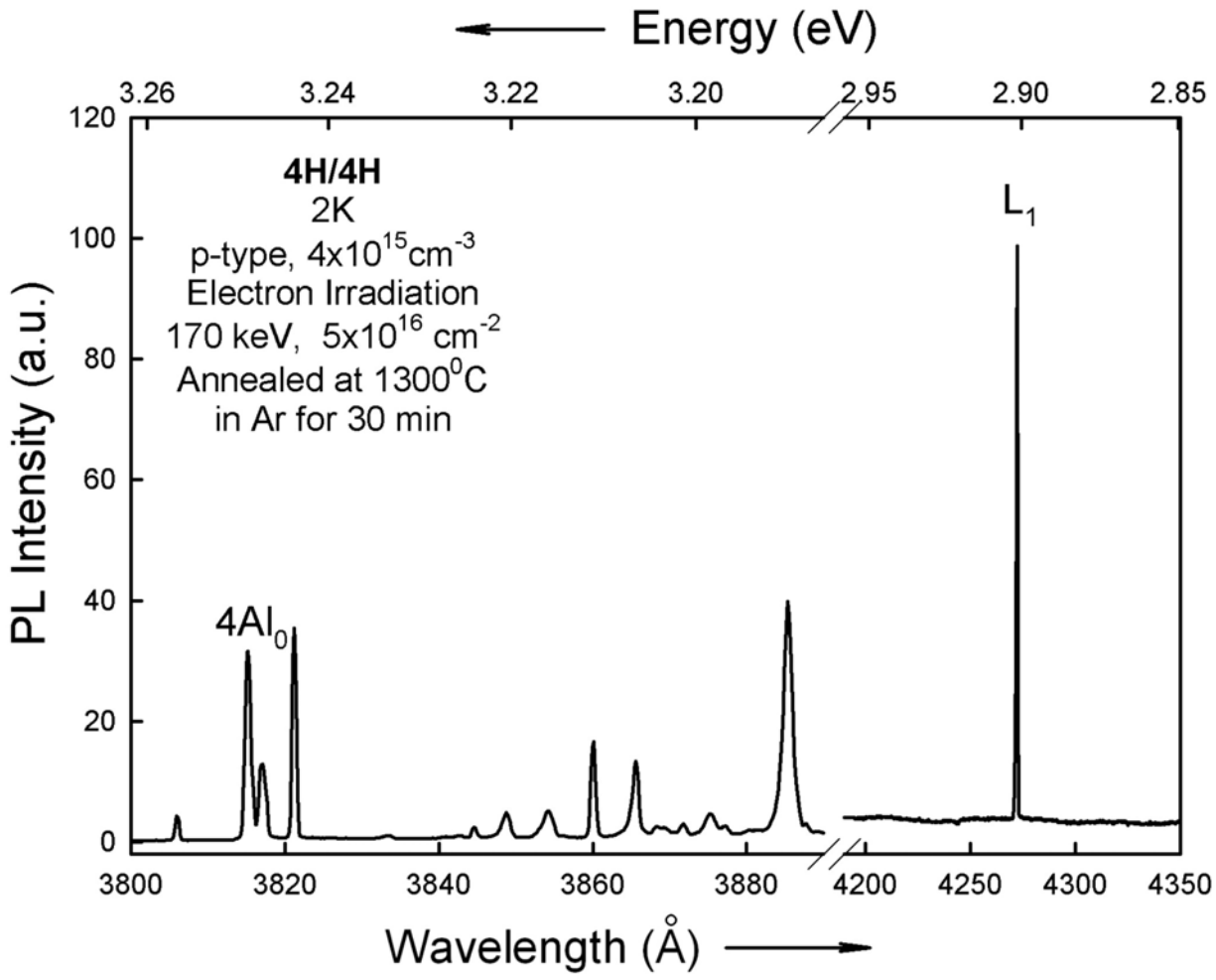

Figure 5.6 One LTPL example from a 170 keV electron irradiated and 1300 °C annealed p-type 4H SiC showing both the D_I no phonon line L_1 and the strongest aluminum bound exciton no phonon line at 3815 Å. The intensity ratio of these two is used to monitor the concentration change of the D_I center in all the samples during the different temperature annealing.

Table 5.2 Intensity ratios of L_1 to the strongest aluminum no phonon line from p-type samples after electron irradiation and annealing.

Annealing Temperature (°C)	Intensity Ratio of L_1 to Al 3815 Å Line	
	170 keV	1 MeV
700	0.183	0.060
800	0.288	0.244
900	0.558	0.156
1000	3.15	2.11
1100	-	6.48
1200	3.64	5.05
1300	3.01	5.77
1400	3.32	9.69
1500	14.7	10.1
1600	7.67	7.24
1700	37.1	11.7

Table 5.2 lists all the ratios of the L_1 line to the aluminum 3815 Å line from both 170 keV and 1 MeV irradiated p-type samples after different annealing. We didn't have enough good samples for the 170 keV and 1100 °C annealing, so it is left blank in the table. When we did the annealing on the n-type materials, we used our ceramic tube furnace for the temperature up to 1500 °C and used the graphite furnace at the University of Erlangen for the 1600 °C and 1700 °C annealing. This time we sent all p-type samples to the University of Erlangen for the annealing to make sure there is no difference in the annealing environment.

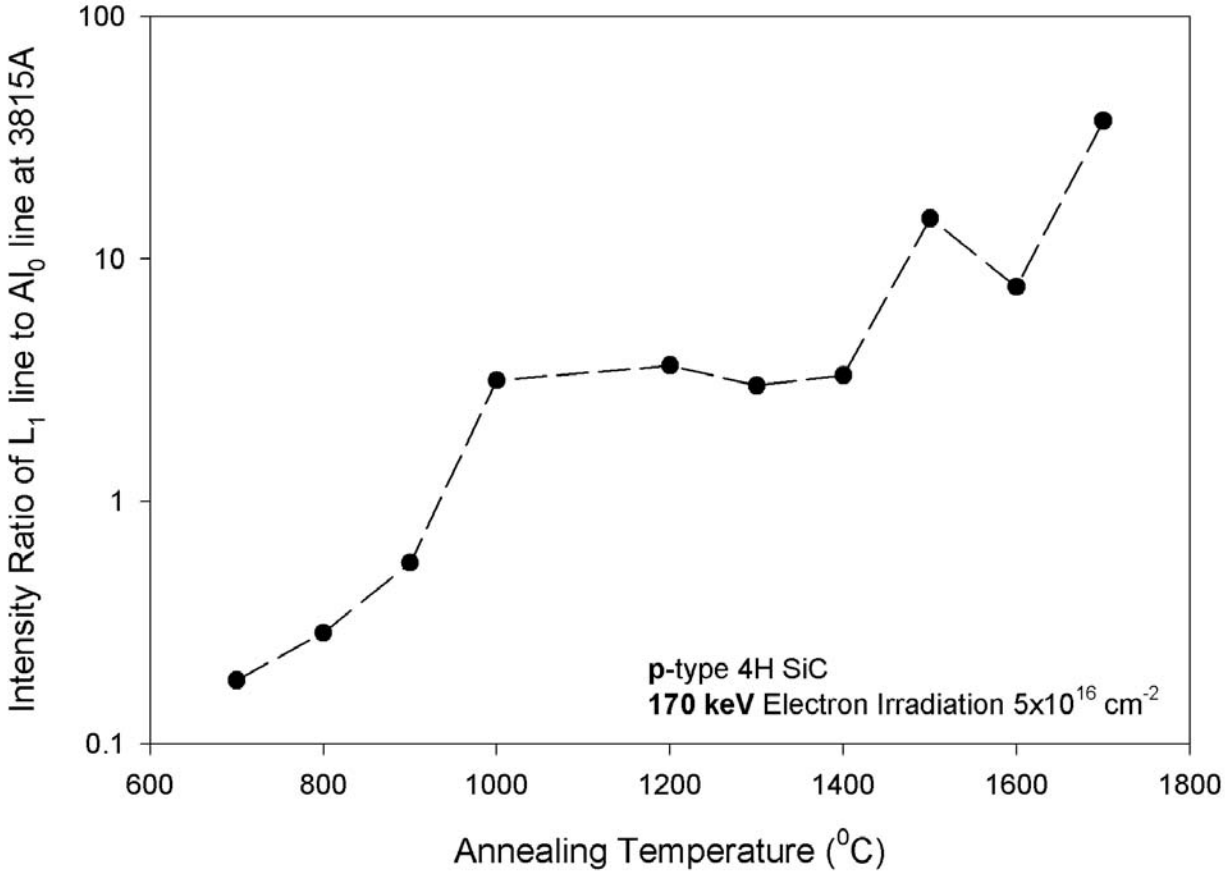

Figure 5.7 The annealing temperature dependence of the intensity ratio of L_1 to the strongest aluminum no phonon line at 3815 Å from p-type 4H SiC which has been irradiated with 170 keV electrons. Note the intensity ratio is plotted in semi-logarithmic scale.

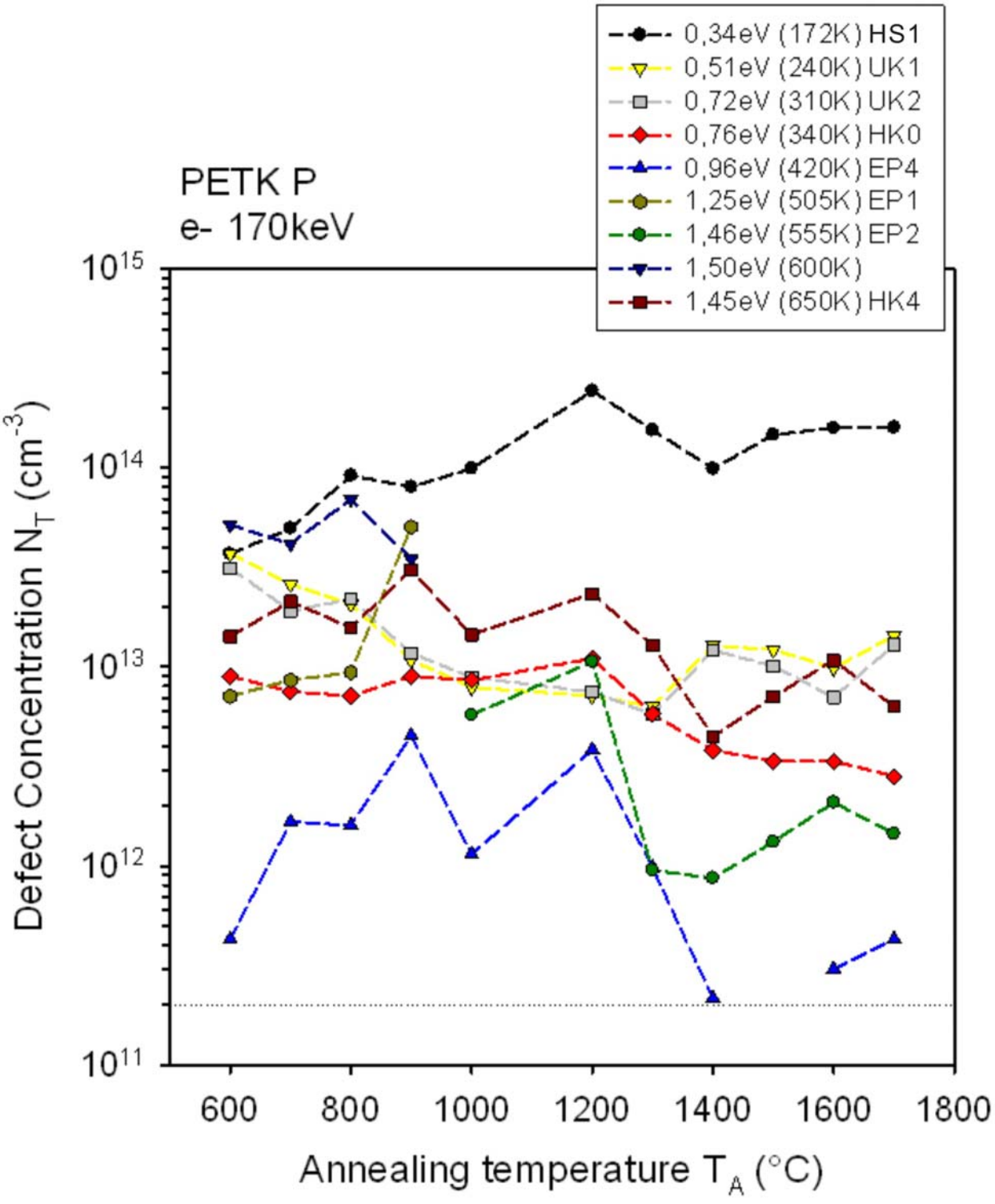

Figure 5.8 The annealing temperature dependence of all the defect centers detected by DLTS from p-type 4H SiC which has been irradiated with 170 keV electrons. The black round dot represents the particular HS1 center which we are trying to correlate to the L_1 line from the D_I center in LTPL.

Figure 5.7 shows the annealing temperature dependence of the intensity ratio of L_1 to the Al 3815 Å line from p-type 4H SiC which has been irradiated by 170 keV electrons. The ratio of the LTPL line L_1 to Al_0 can be seen to vary by more than two orders of magnitude between 700 °C and 1700 °C. In the pseudodonor model of 4H SiC the ground state of the D_I center is postulated to be 343 meV above the valence band. Hence the appearance of a 340 meV peak above the valence band in p-type 4H SiC might be associated with the ground state of D_I in the pseudodonor model. Indeed, a 0.34 eV peak was observed in the p-type DLTS measurements, as shown in Figure 5.8. The black dots represent the concentration of the E_V + 0.34 eV center measured from DLTS. This is the most dominating defect center in the p-type samples, especially after high temperature annealing. Unfortunately, the concentration of the 0.34 eV peak appears essentially constant (increases by a factor of three) as we anneal the p-type samples from room temperature to 1700 °C. As we have already pointed out we find the L_1 peak of the D_I center to increase in intensity by more than a factor of 100 between samples annealed at 700 °C and 1700 °C. Apparently these two centers do not show a one-to-one correlation judging from the results on the170 keV electron irradiated p-type 4H SiC.

We can also compare the results from the 1 MeV electron irradiated p-type 4H SiC. The results from the LTPL and DLTS are shown in Figure 5.9 and Figure 5.10, respectively. The intensity ratio of the L_1 line to the Al 3815 Å line increases by two orders of magnitude as the annealing temperature goes up. But the concentration of the E_V + 0.34 eV defect is fluctuating within one order of magnitude. We do not see any clear correlation between these two on the 1 MeV electron irradiated p-type 4H SiC.

Therefore, the conclusion of the experiments on p-type 4H SiC is that no correlation has been found between the 340 meV DLTS level and the L_1 line of the D_I center and our

experiments provide no confirmation of the existence of a 343 meV ground state postulated in the pseudodonor model.

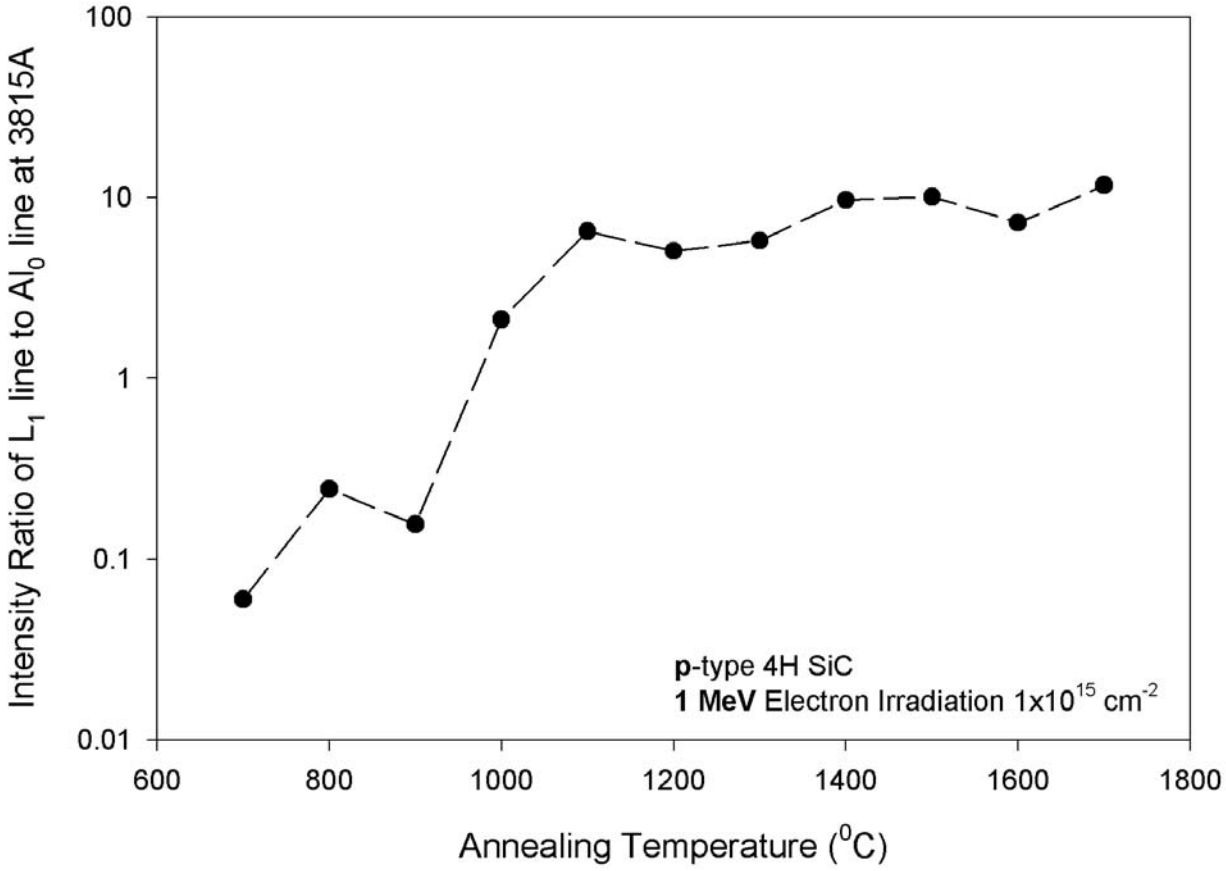

Figure 5.9 The annealing temperature dependence of the intensity ratio of L_1 to the strongest aluminum no phonon line at 3815 Å from p-type 4H SiC which has been irradiated with 1 MeV electrons. Note the intensity ratio is plotted in semi-logarithmic scale.

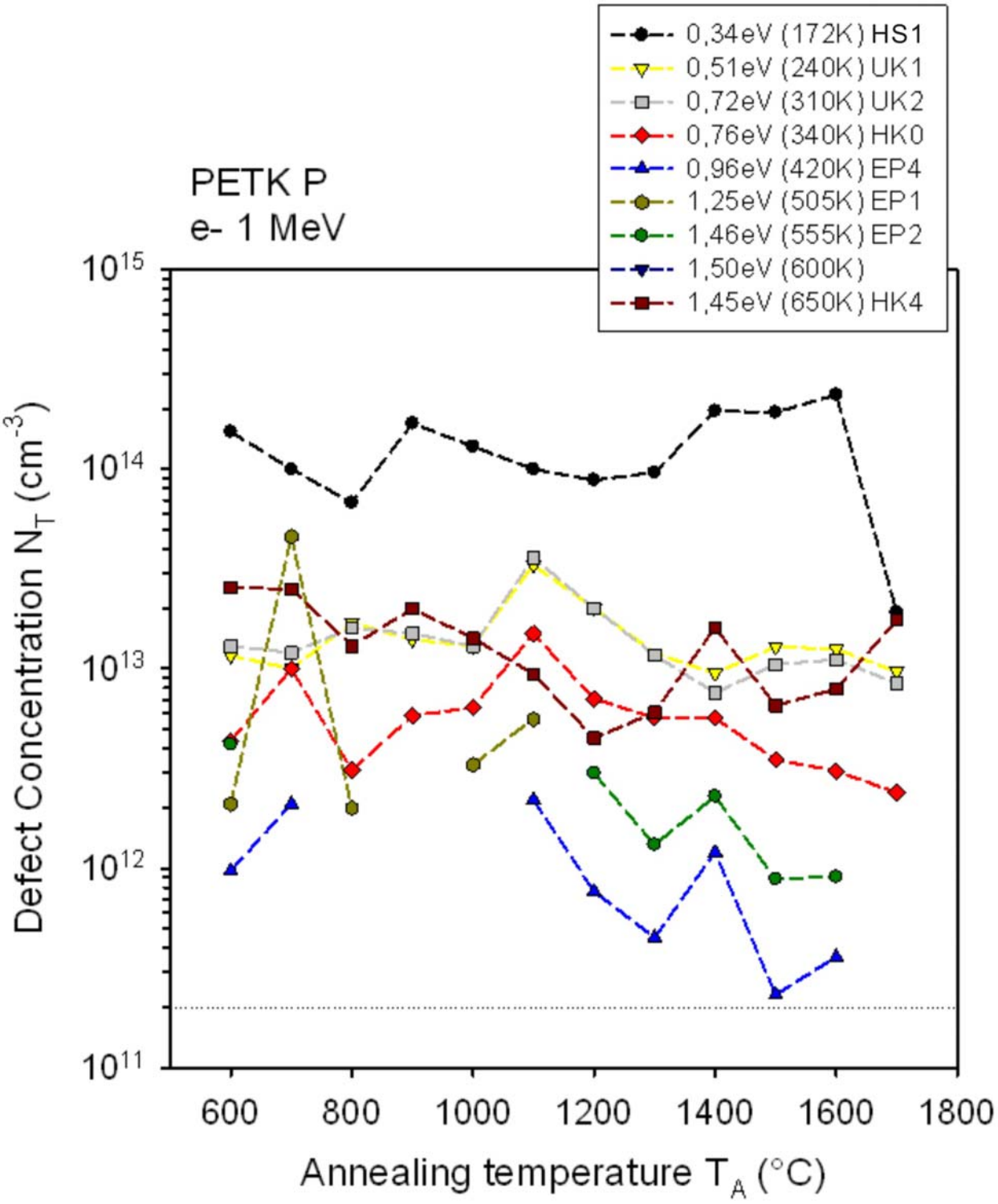

Figure 5.10 The annealing temperature dependence of all the defect centers detected by DLTS from p-type 4H SiC which has been irradiated with 1 MeV electrons. The black round dot represents the particular HS1 center which we are trying to correlate to the L_1 line from the D_I center in LTPL.

5.4 CONCLUSION

We have studied the LTPL of n-type and p-type 4H SiC irradiated by 170 KeV and 1 MeV electrons with annealing at different temperatures. In n-type 4H SiC no correlation is found between the Z_1/Z_2 DLTS signal at annealing temperatures from room temperature to 1700 °C and the intensity of L_1 measured by LTPL in the same temperature interval. Hence, we conclude there is no connection between Z_1/Z_2 and D_I. In p-type SiC no correlation is found between the 340 meV DLTS signal and the intensity variation of the L_1 line of the D_I center. We conclude that our data cannot verify the existence of a 343 meV ground state for the D_I center in the pseudodonor model.

APPENDIX A

DEEP LEVEL TRANSIENT SPECTROSCOPY

A.1 BACKGROUND ON DEEP LEVEL TRANSIENT SPECTROSCOPY

A.1.1 Capture and Emission Processes on the Deep Level Defects

Figure A.1 shows the electron energy band diagram of a deep level defect inside the semiconductor bandgap. E_C and E_V are the bottom of the conduction band and top of the valence band, respectively. E_T is the energy position of the deep level, which has a concentration of N_T. The electron concentration is n in the conduction band and the hole concentration is p in the valence band. There are totally four difference processes that could happen in the bandgap. The deep level defect could capture an electron from the conduction band with an electron capture coefficient c_n, which is labeled as process (a) in Figure A.1. There are two possible processes following this process (a). The electron which is captured could be emitted and return to the conduction band with an electron emission coefficient e_n, labeled as process (b) in Figure A.1. Or the defect could capture a hole from the valence band with a hole capture coefficient c_p, which is process (c) in Figure A.1. Now the deep defect is occupied by a hole and there are two possible processes. It could emit the hole back to the valence band with a hole emission coefficient c_p,

which is labeled as process (d) in Figure A.1. Or it could capture an electron from the conduction band, which is just process (a).

There are two possible charge states on the deep centers. When it is occupied by an electron, it is in the n_T state. When it is occupied by a hole, it is in the p_T state. The total density of these two charge states should equal the density of the deep centers itself $N_T = n_T + p_T$. The electron concentration n in the conduction band is affected by the electron capture process (a) and electron emission process (b). The rate of change of the electron concentration in the conduction band can be written as

$$\frac{dn}{dt} = e_n n_T - c_n n p_T \tag{A.1}$$

The physics meaning of this equation is that the rate of change of the electron concentration is increased by the electron emission process (b) from the deep centers and is decreased by the electron capture process (a). For the electron emission process, it is proportional to the total number of deep centers occupied by an electron. The second term on the right side of Eq. (A.1) is the electron capture rate. It is slightly different from the first term because it is also proportional to the total electrons available in the conduction band. Therefore there is an extra factor n in the second term. So e_n means the total number of electrons emitted per second from the deep centers. c_n means the total number of electrons captured per second to the deep centers. $c_n n$ means the total number of electrons captured per second from the conduction band to the deep centers.

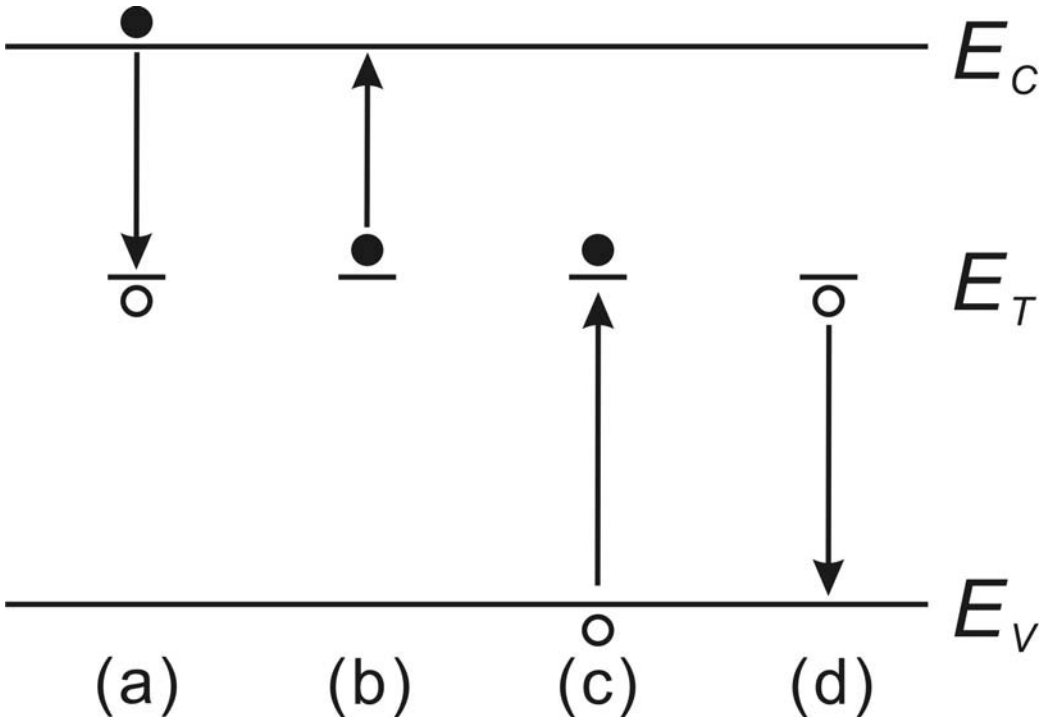

Figure A.1 Electron energy band diagram with deep level defects. (a), (b), (c) and (d) are electron capture and emission processes mentioned in the text.

The electron capture coefficient is defined as

$$c_n = \sigma_n v_{th} \tag{A.2}$$

where σ_n is the electron capture cross section of the deep centers and v_{th} is the thermal velocity of the electrons.

Similarly for holes, the rate equation can be written as

$$\frac{dp}{dt} = e_p p_T - c_p p n_T \tag{A.3}$$

Now we can look at the deep centers which are occupied by electrons. The change rate of the concentration of these centers is

$$\begin{aligned}\frac{dn_T}{dt} &= \frac{dp}{dt} - \frac{dn}{dt} \\ &= (e_p p_T - c_p p n_T) - (e_n n_T - c_n n p_T) \\ &= (c_n n + e_p) p_T - (c_p p + e_n) n_T \\ &= (c_n n + e_p)(N_T - n_T) - (c_p p + e_n) n_T\end{aligned} \tag{A.4}$$

Rewrite it and we get this equation:

$$\frac{dn_T}{dt} = -(c_n n + e_p + c_p p + e_n) n_T + (c_n n + e_p) N_T \tag{A.5}$$

We can do an approximation and consider the quasi-neutral regions where *n* and *p* can be considered constant. That will make Eq. (A.5) easy to solve.

To solve this differential equation, I will define two quantities to make the equation look simple. Define $A = (c_n n + e_p) N_T$ and $\tau = \dfrac{1}{c_n n + e_p + c_p p + e_n}$, where A is a constant and will be determined later.

For a first order differential equation $\dfrac{dy}{dx} + P(x) y = Q(x)$, the general solution is $y = e^{-\int P(x)dx}[\int Q(x) e^{\int P(x)dx} dx + C]$, where *C* is a constant.

Compare to Eq. (A.5) and we get $P(x) = \dfrac{1}{\tau}$ and *Q(x)=A*.

So the solution for Eq. (A.5) is

$$\begin{aligned}n_T &= e^{-\int \frac{1}{\tau} dt}[\int A e^{\int \frac{1}{\tau} dt} dt + C] \\ &= e^{-t/\tau}[A\tau e^{t/\tau} + C] \\ &= A\tau + C e^{-t/\tau}\end{aligned} \tag{A.6}$$

Set *t = 0* and we get $n_T(0) = A\tau + C$, so $C = n_T(0) - A\tau$. Put it back into Eq. (A.6), we get

$$n_T = A\tau + Ce^{-t/\tau} = A\tau + (n_T(0) - A\tau)e^{-t/\tau}$$
$$= A\tau(1-e^{-t/\tau}) + n_T(0)e^{-t/\tau}$$
$$= (c_n n + e_p)N_T\tau(1-e^{-t/\tau}) + n_T(0)e^{-t/\tau}$$

$$n_T(t) = n_T(0)e^{-t/\tau} + \frac{c_n n + e_p}{c_n n + e_p + c_p p + e_n} N_T(1-e^{-t/\tau}) \tag{A.7}$$

In order to use Eq. (A.7), we need to do some simplification. In an *n*-type sample, we can neglect the hole concentration *p*. Eq. (A.7) is simplified as

$$n_T(t) = n_T(0)e^{-t/\tau} + \frac{c_n n + e_p}{c_n n + e_p + e_n} N_T(1-e^{-t/\tau}) \tag{A.8}$$

where $\tau = \dfrac{1}{c_n n + e_p + e_n}$.

Now let us consider the Schottky diode on an *n*-type substrate.

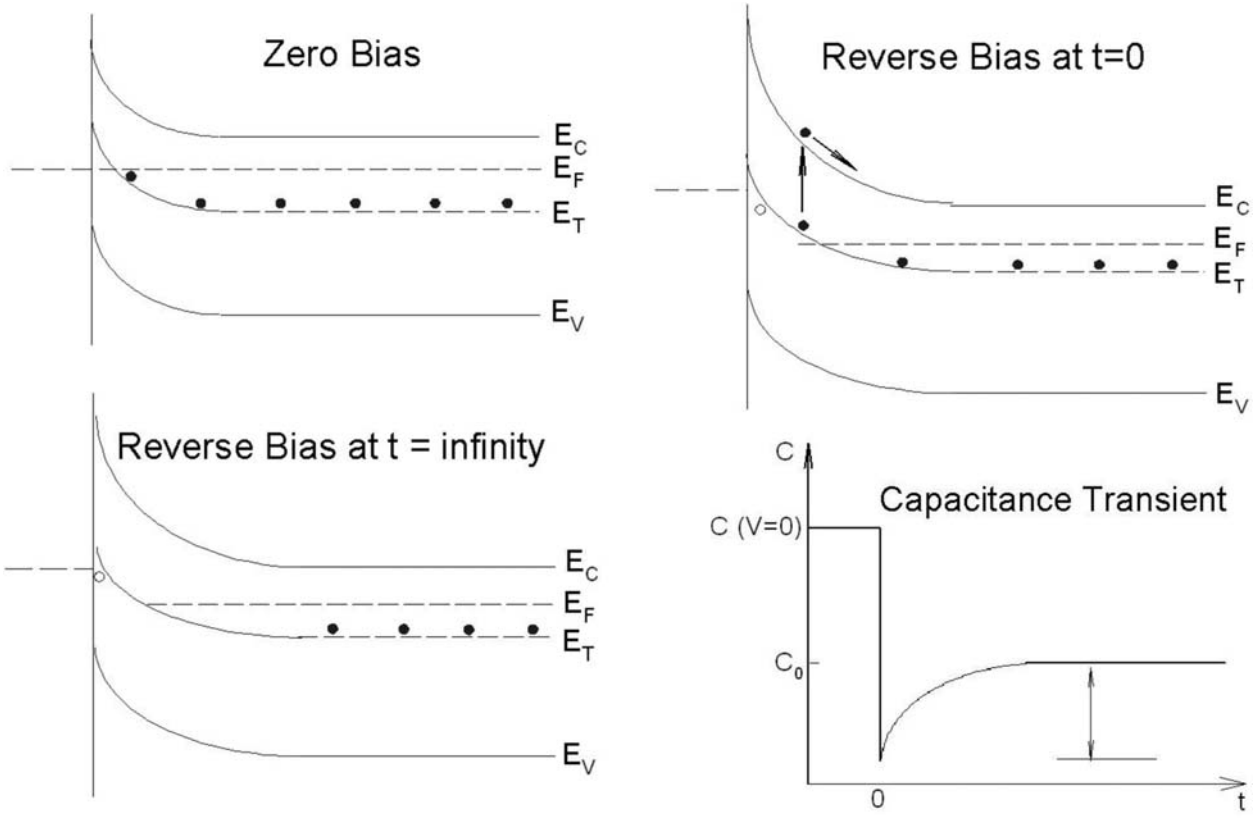

Figure A.2 Schottky diode on an n-type substrate

When the Schottky diode is at zero bias, the deep centers below the Fermi level E_F are occupied by electrons. When a reverse bias is applied, the Fermi level is pushed down and the electrons are emitted from some of the deep centers in the space charge region. Once the electrons jump into the bottom of the conduction band, they could either jump back on the deep centers or be swept out of the space charge region. In reality, the time required to remove the electrons from the space charge region is much shorter than the time required to recapture the electrons back on the deep centers. Finally it will come to equilibrium as $t \to \infty$. During the whole process, the capacitance over this Schottky diode is changing as a function of time. The capacitance transient is shown schematically in Figure A.2.

A.1.2 Capacitance Measurements

The capacitance of a Schottky diode on an n-type substrate can be found in any fundamental semiconductor physics book. In order to explain the topic clearly, I am going to derive all the equations in this section. I will start with a p-n junction first.

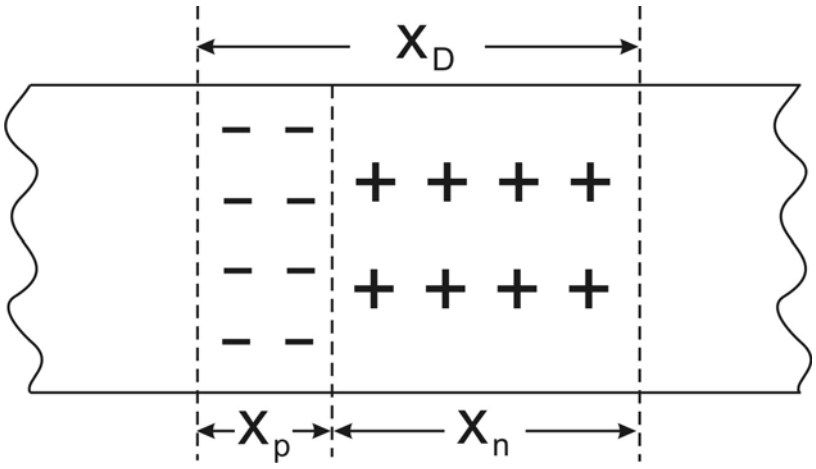

Figure A.3 Schematic drawing of the charge distribution in a p-n junction in thermal equilibrium with zero bias voltage applied.

Figure A.3 is the schematic drawing of a p-n junction. On the left side is the p-type material. On the right side is the n-type material. The width of the negatively charged acceptor ions region is x_p. The width of the positively charged donor ions region is x_n. The total width of the space charge region is $X_D = x_p + x_n$. The charge density distribution in the space charge region is

$$\rho(x) = \begin{cases} -qN_A & (-x_p < x < 0) \\ qN_D & (0 < x < x_n) \end{cases} \tag{A.9}$$

where N_A and N_D are the acceptor and donor concentrations on the p-type and n-type sides, respectively. $x = 0$ is chosen to be at the interface.

Since the p-n junction itself has to be neutral, the net positive charges and net negative charges should cancel out each other. This gives the equation $qN_A x_p = qN_D x_n = Q$, where Q is the total charge on a unit cross section area inside one of the two space charge regions. Therefore

$$N_A x_p = N_D x_n \tag{A.10}$$

From the classical electromagnetics, we know the general Poisson equation for a charge density ρ is $\nabla^2 V = -\frac{\rho}{\varepsilon}$, where ε is the permittivity of the medium and equals to the product of the dielectric constant (relative permittivity) ε_r and the vacuum permittivity ε_0. Apply this equation to both sides of the p-n junction and we have

$$\left.\begin{aligned} \frac{d^2V_1(x)}{dx^2} &= \frac{qN_A}{\varepsilon} \qquad (-x_p < x < 0) \\ \frac{d^2V_2(x)}{dx^2} &= -\frac{qN_D}{\varepsilon} \qquad (0 < x < x_n) \end{aligned}\right\} \tag{A.11}$$

where $V_1(x)$ and $V_2(x)$ are the electric potentials in the negative and positive charge regions.

Integrate Eq. (A.11) once to obtain

$$\left.\begin{aligned} \frac{dV_1(x)}{dx} &= (\frac{qN_A}{\varepsilon})x + C_1 \qquad (-x_p < x < 0) \\ \frac{dV_2(x)}{dx} &= -(\frac{qN_D}{\varepsilon})x + C_2 \qquad (0 < x < x_n) \end{aligned}\right\} \tag{A.12}$$

where C_1 and C_2 are constants to be determined using the boundary conditions.

Outside of the space charge region, the material should be neutral and the electric field is zero. Therefore we can apply this at the boundaries on both left and right sides.

$$\left.\begin{aligned} E\left(-x_p\right) &= -\left.\frac{dV_1(x)}{dx}\right|_{x=-x_p} = 0 \\ E\left(x_n\right) &= -\left.\frac{dV_2(x)}{dx}\right|_{x=x_n} = 0 \end{aligned}\right\} \tag{A.13}$$

Apply Eq. (A.13) back to Eq. (A.12) and we get the two constants:

$$C_1 = \frac{qN_A x_p}{\varepsilon},\ C_2 = \frac{qN_D x_n}{\varepsilon}. \tag{A.14}$$

Eq. (A.10) gives $N_A x_p = N_D x_n$, therefore $C_1 = C_2$. The electric field inside the space charge region is

$$\left.\begin{aligned} E_1\left(x\right) &= -\frac{dV_1(x)}{dx} = -\frac{qN_A(x + x_p)}{\varepsilon} \qquad (-x_p < x < 0) \\ E_2\left(x\right) &= -\frac{dV_2(x)}{dx} = \frac{qN_D(x - x_n)}{\varepsilon} \qquad (0 < x < x_n) \end{aligned}\right\} \tag{A.15}$$

Integrate Eq. (A.15) once to get the equation of the electric potential.

$$\left.\begin{aligned} V_1\left(x\right) &= (\frac{qN_A}{2\varepsilon})x^2 + \frac{qN_A x_p}{\varepsilon}x + D_1 \qquad (-x_p < x < 0) \\ V_2\left(x\right) &= -(\frac{qN_D}{2\varepsilon})x^2 + \frac{qN_D x_n}{\varepsilon}x + D_2 \qquad (0 < x < x_n) \end{aligned}\right\} \tag{A.16}$$

where D_1 and D_2 are constants and will be determined using the boundary conditions.

We can set the electric potential in the neutral region on the p-type side as zero, and then the electric potential in the neutral region in n-type side is V_D, where V_D is the built-in voltage. These are two boundary conditions for Eq. (A.16).

$$V_1(-x_p) = 0,\ V_2(x_n) = V_D\,. \tag{A.17}$$

Put Eq. (A.17) back into Eq. (A.16) and we get those two constants.

$$D_1 = \frac{qN_A {x_p}^2}{2\varepsilon},\ D_2 = V_D - \frac{qN_D {x_n}^2}{2\varepsilon} \tag{A.18}$$

Since $V(x)$ is continuous at $x = 0$, from Eq. (A.16) we can see that $D_1 = D_2$.

Finally we have the equations for the electric potentials.

$$\left.\begin{aligned} V_1(x) &= \frac{qN_A(x^2 + x_p^2)}{2\varepsilon} + \frac{qN_A x x_p}{\varepsilon} \qquad (-x_p < x < 0) \\ V_2(x) &= V_D - \frac{qN_D(x^2 + x_n^2)}{2\varepsilon} + \frac{qN_D x x_n}{\varepsilon} \qquad (0 < x < x_n) \end{aligned}\right\} \tag{A.19}$$

From $V_1(0) = V_2(0)$, we get $\frac{qN_A x_p^2}{2\varepsilon} = V_D - \frac{qN_D x_n^2}{2\varepsilon}$. So

$$V_D = \frac{q(N_A x_p^2 + N_D x_n^2)}{2\varepsilon} \tag{A.20}$$

From two equations $X_D = x_p + x_n$ and $N_A x_p = N_D x_n$, we get

$$x_n = \frac{N_A X_D}{N_D + N_A},\ x_p = \frac{N_D X_D}{N_D + N_A} \tag{A.21}$$

$$N_A x_p^2 + N_D x_n^2 = \frac{N_A N_D X_D^2}{N_D + N_A} \tag{A.22}$$

Eq. (A.20) can be rewritten as

$$V_D = \frac{q}{2\varepsilon}\left(\frac{N_A N_D}{N_D + N_A}\right) X_D^2 \tag{A.23}$$

The width of the whole space charge region is

$$X_D = \sqrt{V_D \left(\frac{2\varepsilon}{q}\right)\left(\frac{N_D + N_A}{N_A N_D}\right)} \tag{A.24}$$

Eq. (A.24) is for the case when there is no bias voltage applied accross the p-n junction. When there is an external voltage V on the p-n junction, the overall voltage across the p-n junction is $V_D - V$. V is greater than zero for a forward bias and less than zero for a reverse bias. Eq. (A.24) can be extended as

$$X_D = \sqrt{\left(\frac{2\varepsilon}{q}\right)\left(\frac{N_D + N_A}{N_A N_D}\right)(V_D - V)}\,. \tag{A.25}$$

From the following equations $X_D = x_p + x_n$ and $qN_A x_p = qN_D x_n = Q$, we can get $X_D = \frac{Q}{qN_A} + \frac{Q}{qN_D} = \frac{Q}{q}\frac{N_A + N_D}{N_A N_D}$. So the relationship between the total charge on a unit cross sectional area and the applied voltage can be written as

$$Q = \sqrt{2\varepsilon q \left(\frac{N_D N_A}{N_A + N_D}\right)(V_D - V)} \tag{A.26}$$

The differential capacitance on a unit cross section area is

$$C' = \frac{dQ}{dV} = \sqrt{2\varepsilon q \left(\frac{N_D N_A}{N_A + N_D}\right)} \cdot \frac{1}{2}(V_D - V)^{-\frac{1}{2}} = \sqrt{\frac{\varepsilon q N_D N_A}{2(N_A + N_D)(V_D - V)}} \tag{A.27}$$

If the cross section area is A, then the total differential capacitance is

$$C = A\sqrt{\frac{\varepsilon q N_D N_A}{2(N_A + N_D)(V_D - V)}} \tag{A.28}$$

For a Schottky diode on n-type material, we can let $N_A \to \infty$. Then we have

$$C = A\sqrt{\frac{\varepsilon q}{2}}\sqrt{\frac{N_D}{V_D - V}} \tag{A.29}$$

So far I have only considered the situation with no deep level defects at reverse bias $-V$. If there are some deep level defects, the donor concentration N_D in Eq. (A.29) should be replaced with the net donor concentration in the space charge region $N_{scr} = N_D - n_T(t)$.

$$C = A\sqrt{\frac{\varepsilon q}{2}}\sqrt{\frac{N_{scr}}{V_D - V}} = A\sqrt{\frac{\varepsilon q}{2}}\sqrt{\frac{N_D - n_T(t)}{V_D - V}} = A\sqrt{\frac{\varepsilon q N_D}{2(V_D - V)}}\sqrt{1 - \frac{n_T(t)}{N_D}} \tag{A.30}$$

Define $C_0 = A\sqrt{\frac{\varepsilon q N_D}{2(V_D - V)}}$, which is the capacitance when there are no deep level defects.

$$C = C_0\sqrt{1 - \frac{n_T(t)}{N_D}} \tag{A.31}$$

Usually during the DLTS measurements, the deep level defect concentration is far less than the donor concentration (which has been discussed in the experiment procedures). Therefore we can do an expansion on Eq. (A.31).

$$C \approx C_0[1 - \frac{n_T(t)}{2N_D}] \tag{A.32}$$

The time dependence of the deep center concentration is Eq. (A.8) $n_T(t) = n_T(0)e^{-t/\tau} + \frac{c_n n + e_p}{c_n n + e_p + e_n} N_T(1 - e^{-t/\tau})$, where $\tau = \frac{1}{c_n n + e_p + e_n}$. Consider the traps in the upper half of the band gap. The electron emission rate e_n is greater than the hole emission rate e_p. So we can neglect e_p. At the initial emission stage, the electron emission process dominates and the electron capture process barely happens. Then we can neglect the electron capture term c_n. Finally we can simplify Eq. (A.8) as

$$n_T(t) = n_T(0)\exp(-t/\tau_e) \tag{A.33}$$

where $\tau_e = \frac{1}{e_n}$.

Put Eq. (A.33) into Eq. (A.32), we get

$$C = C_0[1 - \frac{n_T(0)}{2N_D}\exp(-t/\tau_e)] \tag{A.34}$$

Now we need to find out what τ or e_n is.

Under equilibrium condition, process (a) and (b) in Figure A.1 should cancel each other. Therefore Eq. (A.1) should be zero.

$$e_{n0}n_{T0} = c_{n0}n_0p_{T0} = c_{n0}n_0(N_T - n_{T0}) \tag{A.35}$$

where the subscript 0 represents the equilibrium condition.

From fundamental semiconductor physics, we know that

$$n_0 = n_i \exp(\frac{E_F - E_i}{kT}),\ n_{T0} = \frac{N_T}{1+\exp[(E_T - E_F)/kT]} \tag{A.36}$$

Put Eq. (A.36) into Eq. (A.35), we get

$$e_{n0}\frac{N_T}{1+\exp[(E_T - E_F)/kT]} = c_{n0}n_i \exp(\frac{E_F - E_i}{kT})\frac{N_T \exp[(E_T - E_F)/kT]}{1+\exp[(E_T - E_F)/kT]}$$

$$e_{n0} = c_{n0}n_i \exp(\frac{E_T - E_i}{kT}) = c_{n0}n_1 \tag{A.37}$$

where $n_1 = n_i \exp(\frac{E_T - E_i}{kT})$.

We need to make a critical assumption here, assuming that the emission and capture coefficients remain equal to their equilibrium values under non-equilibrium conditions. Then we can take out the subscript 0 and get a new equation:

$$e_n = c_n n_1 \tag{A.38}$$

Since $\tau_e = \frac{1}{e_n}$ and $c_n = \sigma_n v_{th}$, we can put everything in Eq. (A.38) and get the following:

$$\frac{1}{\tau_e} = \sigma_n v_{th} n_i \exp(\frac{E_T - E_i}{kT})$$

$$\tau_e = \frac{1}{\sigma_n v_{th}} \frac{\exp[(E_i - E_T)/kT]}{n_i} \tag{A.39}$$

From fundamental semiconductor physics, we know that n_0 can be expressed using the effective density of states in the conduction band N_c as

$$n_0 = N_c \exp[-(E_C - E_F)/kT] \tag{A.40}$$

Compare Eq. (A.40) to Eq. (A.36), we get

$$\frac{1}{n_0} = \frac{\exp[-(E_F - E_i)/kT]}{n_i} = \frac{\exp[(E_C - E_F)/kT]}{N_c} \tag{A.41}$$

Multiply $\exp[(E_F - E_T)/kT]$ on both sides of Eq. (A.41) and get a new equation:

$$\frac{\exp[(E_i - E_T)/kT]}{n_i} = \frac{\exp[(E_C - E_T)/kT]}{N_c} \tag{A.42}$$

We can rewrite Eq. (A.39) as

$$\tau_e = \frac{1}{\sigma_n v_{th}} \frac{\exp[(E_C - E_T)/kT]}{N_c} = \frac{\exp[(E_C - E_T)/kT]}{\sigma_n v_{th} N_c} \tag{A.43}$$

The thermal velocity of electrons is

$$v_{th} = \sqrt{\frac{3kT}{m_n}} \tag{A.44}$$

The density of states in the conduction band is

$$N_c = 2(\frac{2\pi m_n kT}{h^2})^{3/2} \tag{A.45}$$

Therefore the time constant is

$$\tau_e = \frac{\exp[(E_C - E_T)/kT]}{\sigma_n \sqrt{\frac{3kT}{m_n}} 2(\frac{2\pi m_n kT}{h^2})^{3/2}} = \frac{\exp[(E_C - E_T)/kT]}{T^2 \sigma_n \sqrt{\frac{3k}{m_n}} 2(\frac{2\pi m_n k}{h^2})^{3/2}}$$

Define $\gamma_n = \sqrt{\frac{3k}{m_n}} 2(\frac{2\pi m_n k}{h^2})^{3/2}$, which is a constant determined by the electron effective mass. We can get the equation of the time constant as a function of temperature:

$$\tau_e = \frac{\exp[(E_C - E_T)/kT]}{T^2 \sigma_n \gamma_n} \tag{A.46}$$

During the DLTS measurement using a double boxcar instrument, the capacitance difference between two different times is a standard output feature. Use Eq. (A.34), we get

$$\delta C = C(t_1) - C(t_2) = \frac{C_0 n_T(0)}{2N_D}[\exp(-t_2/\tau_e) - \exp(-t_1/\tau_e)]. \tag{A.47}$$

Figure A.4 illustrates how the DLTS spectrum is obtained. The capacitance decay is shown on the left side at different temperatures with different decay rate, which can be explained by Eq. (A.46). When the capacitance decays really slowly or fast, the capacitance difference between two different window times t_1 and t_2 is quite small. This capacitance difference reaches the maximum value at a temperature in the middle. This δC as a function of the temperature T is plotted on the right side. In order to find the temperature with the maximum capacitance difference, we can set the differential of Eq. (A.47) with respect to τ_e to zero.

$$\frac{d(\delta C)}{d\tau_e} = \frac{C_0 n_T(0)}{2N_D}[-t_2 \exp(-t_2/\tau_e) + t_1 \exp(-t_1/\tau_e)] = 0$$

$$t_2 \exp(-t_2/\tau_e) = t_1 \exp(-t_1/\tau_e)$$

$$\frac{t_2}{t_1} = \exp[-\frac{1}{\tau_e}(t_1 - t_2)]$$

$$\ln(\frac{t_2}{t_1}) = \frac{1}{\tau_e}(t_2 - t_1)$$

$$\tau_{e,\max} = \frac{t_2 - t_1}{\ln(t_2/t_1)} \tag{A.48}$$

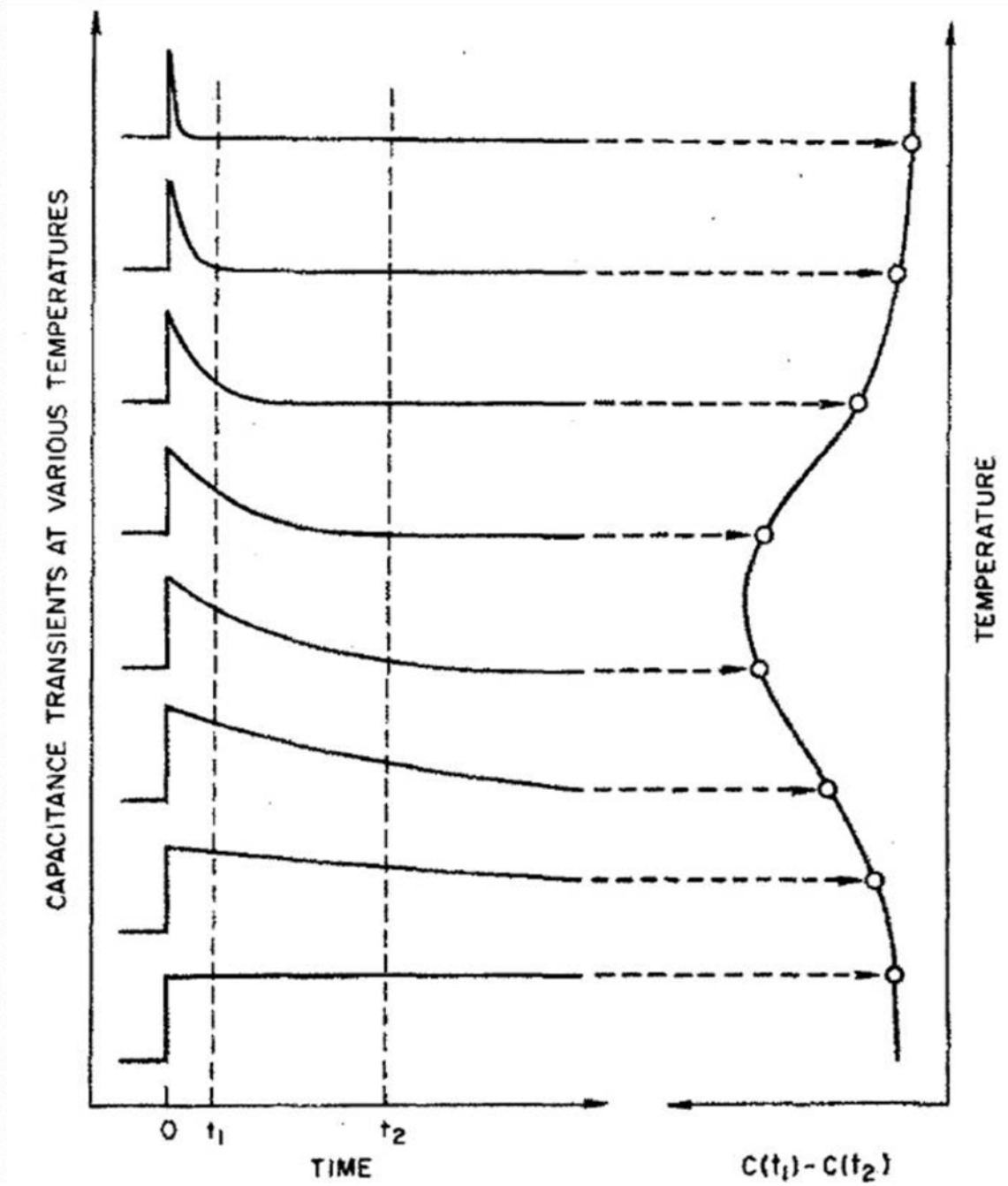

Figure A.4 Illustration of how a double boxcar is used to define the rate window. The left-hand side shows capacitance transients at various temperatures, while the right-hand side shows the corresponding DLTS signal resulting from using the double boxcar to display the difference between the capacitance at time t_1 and the capacitance at time t_2 as a function of temperature. Figure is taken from D. V. Lang, J. Appl. Phys. 45, 3023 (1974).

From Eq. (A.46) $\tau_e = \dfrac{\exp[(E_C - E_T)/kT]}{T^2 \sigma_n \gamma_n}$, we can re-arrange the equation and get

$$\ln(\tau_e T^2) = \frac{E_C - E_T}{k}\frac{1}{T} - \ln(\sigma_n \gamma_n) \tag{A.49}$$

Usually the capture cross section is assumed to be temperature independent. Therefore a plot of $\ln(\tau_e T^2)$ versus $1/T$ is a straight line using values of τ_e for various choices of t_1 and t_2. The slope gives the deep centers energy level. The intercept on the y-axis gives the capture cross section.

Another important property of the deep center is the concentration. It can be obtained from Eq. (A.47) $\delta C = \dfrac{C_0 n_T(0)}{2N_D}[\exp(-t_2/\tau_e) - \exp(-t_1/\tau_e)]$. First let's set $r = t_2/t_1$.

$$\begin{aligned}
N_T \approx n_T(0) &= \frac{\delta C_{\max}}{C_0}\cdot 2N_D \cdot \frac{1}{\exp(-t_2/\tau_e) - \exp(-t_1/\tau_e)} \\
&= \frac{\delta C_{\max}}{C_0}\cdot 2N_D \cdot \frac{1}{\exp[-\dfrac{t_2}{t_2 - t_1}\ln(\dfrac{t_2}{t_1})] - \exp[-\dfrac{t_1}{t_2 - t_1}\ln(\dfrac{t_2}{t_1})]} \\
&= \frac{\delta C_{\max}}{C_0}\cdot 2N_D \cdot \frac{1}{\exp[-\dfrac{r}{r-1}\ln r] - \exp[-\dfrac{1}{r-1}\ln r]} \\
&= \frac{\delta C_{\max}}{C_0}\cdot 2N_D \cdot \frac{1}{r^{\frac{r}{1-r}} - r^{\frac{1}{1-r}}} \\
&= \frac{\delta C_{\max}}{C_0}\cdot 2N_D \cdot \frac{r^{\frac{r}{r-1}}}{r^{\frac{r}{r-1}}(r^{\frac{r}{1-r}} - r^{\frac{1}{1-r}})}
\end{aligned}$$

$$N_T = \frac{\delta C_{\max}}{C_0}\cdot 2N_D \cdot \frac{r^{\frac{r}{r-1}}}{1-r} \tag{A.50}$$

The DLTS system can measure $\frac{\delta C_{\max}}{C_0}$ in the range of 10^{-5} to 10^{-4}. The donor concentration can be obtained from the C-V measurement. Therefore the deep center concentration can be obtained from the above equation.

To summarize, the most important equations in the DLTS measurement are

$$C = C_0[1 - \frac{n_T(0)}{2N_D}\exp(-t/\tau_e)]$$

$$\tau_e = \frac{\exp[(E_C - E_T)/kT]}{T^2\sigma_n\gamma_n}$$

$$\tau_{e,\max} = \frac{t_2 - t_1}{\ln(t_2/t_1)}$$

The procedure to carry out a DLTS measurement is

1. Set a window rate τ_{ref} by setting t_1 and t_2.
2. Heat up the sample.
3. When the temperature T reaches a value which makes $\tau_e(T, E_T, \sigma_n)$ equal τ_{ref}, one can get the maximum output on the meter. Different deep centers have different E_T and σ_n. Therefore they will show up as different peaks at different temperatures.
4. Change the preset value of τ_{ref} and get a different DLTS spectrum. The peak positions will shift a little bit.
5. From all the runs, one can get a data set with a τ_{ref} corresponding to a maximum temperature T for each deep center.
6. Plot $\ln(\tau_e T^2)$ versus $1/T$. Get the deep center energy level from the slope and the capture cross section from the intercept, respectively.

A.2 EXAMPLE OF DLTS MEASUREMENTS

To give an example of the DLTS measurement, I am going to use the figure in D.V. Lang's original DLTS paper to do the calculations. Figure A.5 is copied directly from D.V. Lang's first paper on DLTS. I'm going to use trap B as an example. I can do a rough estimate of all the peak positions and get Table A.1.

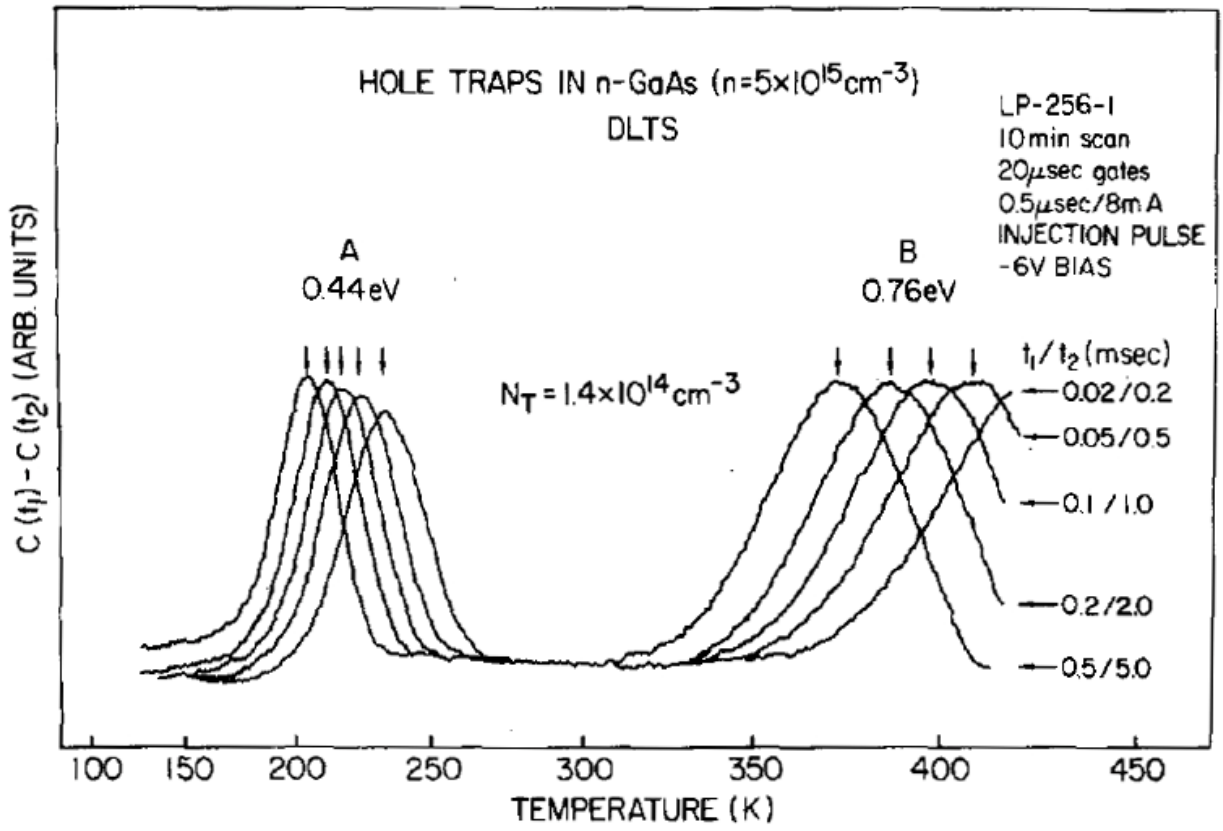

Figure A.5 Typical experimental DLTS spectra for hole traps in n-GaAs. The two traps are labeled A and B and have activation energies measured from the valence band of 0.44 and 0.76 eV, respectively. The trap concentrations are both 1.4×10^{14} cm^{-3}. Five different spectra are shown corresponding to the five rate windows determined by the values of t_1 and t_2. Figure and text are taken from D. V. Lang, J. Appl. Phys. 45, 3023 (1974).

Table A.1 Window times, rate windows and peak positions of trap B from DLTS spectra in Figure A.5.

t_1 (msec)	t_2 (msec)	τ (msec)	T (K)
0.5	5	1.95	372.22
0.2	2	0.78	387.33
0.1	1	0.39	397.78
0.05	0.5	0.20	408.89

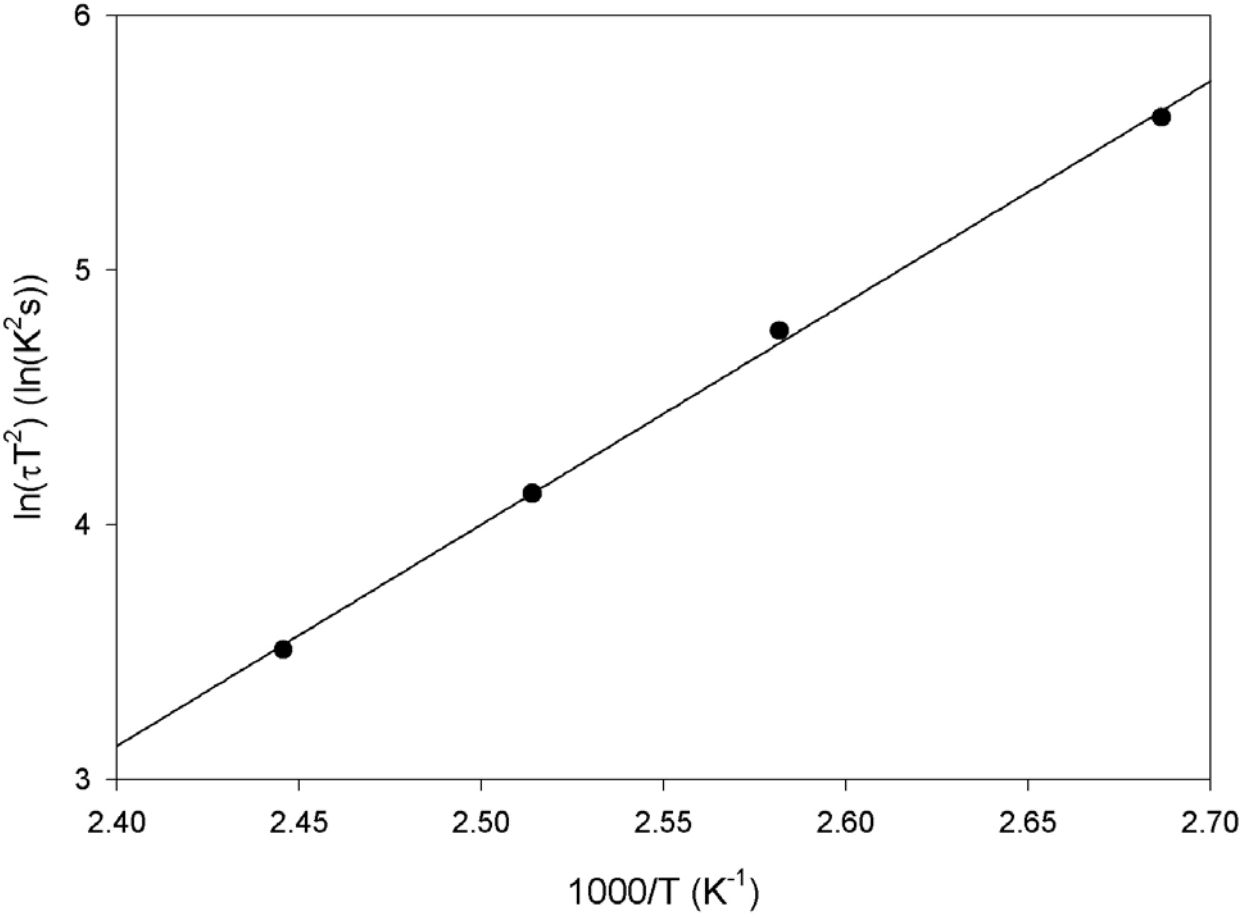

Figure A.6 Plot of $\ln(\tau_e T^2)$ as a function of 1000/T. The round dots are experimental data from the above table. The straight line is a polynomial fitting**.**

Figure A.6 shows the plot of $\ln(\tau_e T^2)$ versus 1000/*T*. The straight line fitting gives the equation $y = 8.700 \cdot x - 17.75$.

The slope is $\frac{E_C - E_T}{1000k} = 8.700$, where k = 8.617x10^{-5} eV/K is the Boltzmann constant. Therefore the energy level is given by $E_C - E_T = 0.75$ eV. This is consistent with the value 0.76 eV D.V. Lang got in his paper. The slight difference comes from my rough estimate of the peak positions from Figure A.5.

In n-type GaAs, γ has an accepted value of 2.3x10^{20} cm^{-2}s^{-1}K^{-2}. From the value of the intercept, we can get the capture cross section $\sigma_n = 2.22 \times 10^{-13}\ cm^2$.

To summarize this section, I have explained the theory behind the DLTS technique and showed how to extract the valuable information from the experimental data. The actual DLTS system used for our investigations on the deep defect centers is described in Ref. [48].

APPENDIX B

MONTE CARLO SIMULATION OF ELECTRON TRAJECTORIES IN SILICON CARBIDE USING THE CASINO PROGRAM

We used the CASINO program [37] as a Monte Carlo simulation of electron trajectories in the SiC material, but crystal structure is not taken into account. The name CASINO is derived from the word "monte CArlo SImulation of electroN trajectory in sOlids". It is widely used to calculate the irradiation electron distribution inside the sample, which is quite useful if we want to know how the irradiation electron travels inside the material and the damage caused by that. We fully appreciate that this program is strictly applicable for electrons with energy less than 50 keV under non-relativistic conditions! When the electron has a kinetic energy above 50 keV, the relativistic effect has to be considered but the simulation gets very complicated. We can do a comparison between the non-relativistic and relativistic conditions and find out the error between these two.

For the non-relativistic case, the classical equation for the kinetic energy of the electron is

$$E_k = \frac{1}{2} m_0 v^2 \tag{B.1}$$

where $m_0 = 9.11 \times 10^{-31} kg$ is the rest mass of the electron.

So the velocity is

$$v = \sqrt{\frac{2E_k}{m_0}} = \sqrt{\frac{2e \cdot U}{m_0}} \tag{B.2}$$

where $e = 1.60 \times 10^{-19} C$ is the charge on electron. U is the voltage applied to the electron. Put in different values for U and we get the following Table B.1.

Table B.1 Velocities of electron with different energies using the non-relativistic expression.

U (V)	*v (m/s)*
15 *kV*	7.26 x 10^7
170 *kV*	2.45 x 10^8
300 *kV*	3.25 x 10^8
1 *MV*	5.93 x 10^8

The velocities for 300 kV and 1 MV electrons are greater than the speed of light 3.00 x 10^8 *m/s*, which can't be right. That tells us we can't use the classical equations to calculate the velocity of electrons. We have to use the theory of relativity.

For the relativistic case, the mass of an electron increases as its speed increases according to the following formula

$$m = \frac{m_0}{\sqrt{1-\beta^2}}, \tag{B.3}$$

where $\beta = \frac{v}{c}$ and c = 3.00 x 10^8 *m/s* is the speed of light.

The momentum of the electron is given by $p = mv$, which is just like the classical formula for momentum, except that the mass m of the electron is a function of its speed v.

From the theory of relativity, we know the relationship between the total energy and the kinetic energy of the electron is

$$E_k = E - E_0 \tag{B.4}$$

where $E = mc^2$ is the total energy of the electron while $E_0 = m_0 c^2$ is the rest energy of the electron.

The relationship between the total energy and the momentum of the electron is

$$E^2 = c^2 p^2 + E_0^2 . \tag{B.5}$$

Therefore

$$\begin{aligned} E_k = E - E_0 &= \sqrt{{E_0}^2 + c^2 p^2} - E_0 \\ &= \sqrt{{E_0}^2 + c^2 m^2 v^2} - E_0 \\ &= \sqrt{{E_0}^2 + c^2 \frac{m_0^2}{1-\beta^2} v^2} - E_0 \\ &= \sqrt{{E_0}^2 + m_0^2 c^4 \frac{v^2}{c^2 - v^2}} - E_0 \\ &= E_0 \sqrt{1 + \frac{1}{\left(\frac{c}{v}\right)^2 - 1}} - E_0 \end{aligned}$$

Rearrange the equation and we get

$$\left(\frac{c}{v}\right)^2 = 1 + \frac{1}{\left[1 + \left(\frac{E_k}{E_0}\right)^2\right] - 1} \tag{B.6}$$

We can calculate the value of E_0 first.

$$E_0 = m_0 c^2 = 9.11 \times 10^{-30} \times \left(3.00 \times 10^8\right)^2 \times \frac{1}{1.60 \times 10^{-19}} eV = 5.11 \times 10^5 \ eV = 511 \ keV = 0.511 \ MeV$$

When $\frac{E_k}{E_0} << 1$, we can do an expansion on Eq. (B.6) and get the following

$$\left(\frac{c}{v}\right)^2 \approx 1 + \frac{1}{\left[1 + 2\left(\frac{E_k}{E_0}\right)\right] - 1} = 1 + \frac{1}{2}\left(\frac{E_0}{E_k}\right) \approx \frac{1}{2}\left(\frac{E_0}{E_k}\right) \tag{B.7}$$

Put $E_0 = m_0 c^2$ back in and we get

$$\left(\frac{c}{v}\right)^2 = \frac{1}{2}\frac{m_0 c^2}{E_k}, \tag{B.8}$$

which can be written as $E_k = \frac{1}{2} m_0 v^2$ and is the kinetic energy of the electrons in the non-relativistic limit. Note that the condition for this equation to hold is $\frac{E_k}{E_0} << 1$. That means $E_k << E_0 = 511\ keV$. Therefore, we can only use the non-relativistic conditions for electrons with energy less than 50 keV.

If E_k is large enough so that the non-relativistic mechanics doesn't hold, we have to use Eq. (B.6) to calculate the electron velocity. Table B.2 shows the velocities of electron with different energies in this case.

Table B.2 Velocities of electron with different energies under relativistic conditions.

E_k	*v/c*	*v (m/s)*
15 *keV*	0.237	7.11 x 10^7
170 *keV*	0.661	1.98 x 10^8
300 *keV*	0.777	2.33 x 10^8
1 *MeV*	0.941	2.82 x 10^8

We can compare the two tables for the relativistic and non-relativistic results and see that the velocity is almost the same for a 15 *keV* electron. This is the voltage usually used for scanning electron microscope (SEM). For the higher energy electrons which people use for irradiation, there is a big error between these two cases. The error is 24% for the 170 *keV*

electron and 110% for the 1 *MeV* electron. We believe it is still useful to use the CASINO program to simulate 170 keV electrons since the error is not excessive.

Another thing we have to keep in mind is the electron energy threshold to kick out a carbon atom. This program, by default, simulates the electron trajectory until the electron energy is less than 50 eV. What we are interested in for these experiments are the electrons which have an energy greater than 100 keV so that they can create a carbon vacancy and a carbon interstitial. Hence in our calculations we stop the simulation when the energy drops from 170 keV to 100 keV. Figure B.1 is the simulated penetration depth of the 170 keV electrons. Most of the electrons stop near a depth of 90 μm. Therefore, since the FreD and He-Cd laser penetration is far smaller than 90 μm [38], the LTPL signal we get is entirely from the irradiated part of the material.

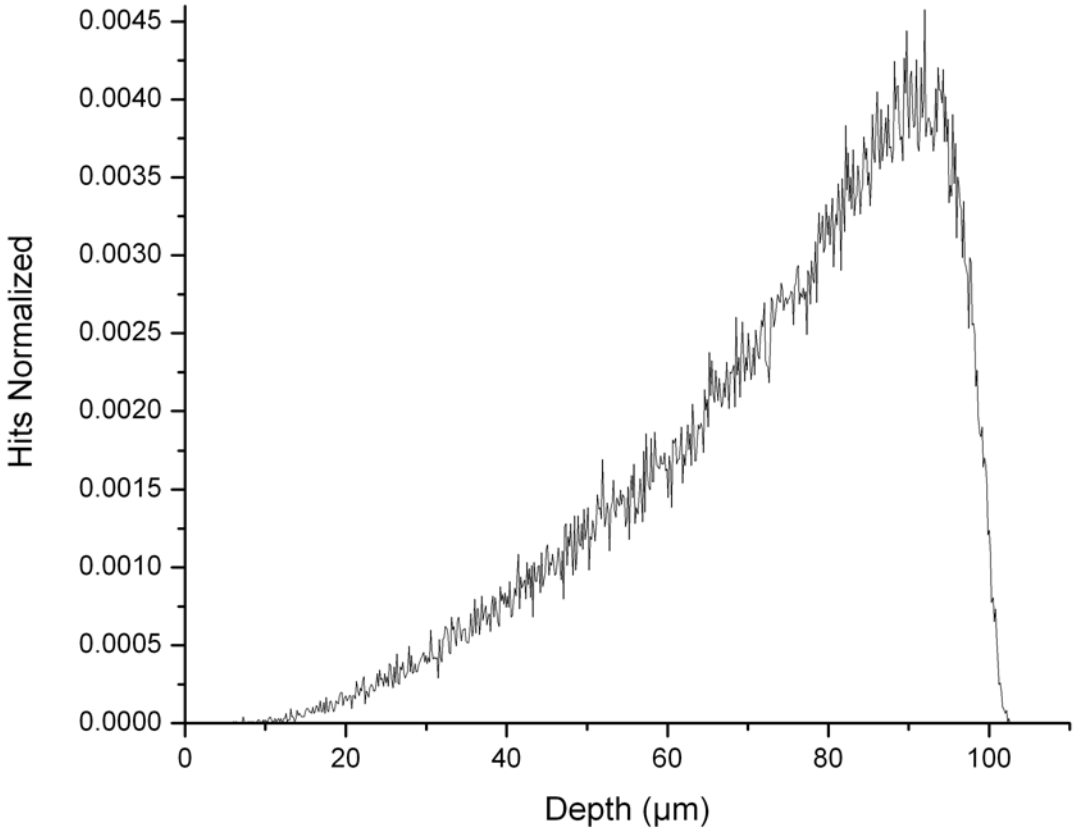

Figure B.1 Simulated electron penetration depth profile of 170 keV electrons stopping at 100 keV.

APPENDIX C

D_{II} DEEP DEFECT IN 3C SILICON CARBIDE

C.1 ATOMIC MODEL OF D_{II} DEFECT CENTER IN SILICON CARBIDE

As I have mentioned in Chapter 2, the D_{II} center is usually observed in ion-implanted SiC regardless of the polytype [15, 21]. The spectrum of D_{II} consists of the no-phonon line(s) with vibrational replicas. It also has some gap modes and localized modes. These localized modes have energy higher than the lattice limit of 120 meV in SiC. The highest energy is near 165 meV, which is the highest lattice frequency in diamond [16]. Therefore a model of a carbon di-interstitial (two carbon atoms sharing an interstitial site) was first proposed in Ref. [20], based on the argument that a di-interstitial is one of the simplest defect complexes and the interstitials can stiffen the lattice. The strong carbon-carbon bonds account for the high energy localized modes above the 120 meV lattice limit. The D_{II} center in 6H and 4H SiC was re-visited by S.G. Sridhara et al. and these authors used the original carbon di-interstitial model to describe the D_{II} center [21].

Recently, theorists have done many calculations on the vibrational spectra for different defect complexes. In a paper published by A. Mattausch et al., the carbon di-interstitial model was ruled out and a new model of a carbon antisites cluster was proposed [15]. An *ab initio*

density-functional theory calculation was done using the software package FHI96SPIN [49]. The authors used large supercells with 216 lattice sites for 3C SiC and 128 sites for 4H SiC for all calculations of the defect energetics. They found that the formation energy of the carbon di-interstitial is about 12 eV, which is extremely high and rules out this model. They also calculated the carbon split interstitial, which is a pair of carbon atoms sharing the same (carbon) site. Calculation shows that the carbon split interstitial defects are very mobile and therefore do not agree with the thermal stability of the D_{II} center. The number of the local vibrational mode energies they calculated beyond the bulk lattice spectrum from this model does not match the number from the experimental D_{II} spectrum. Therefore, they ruled out this model as well. The next model they calculated is the carbon antisite C_{Si}, which is a carbon atom sitting on the silicon lattice site. This model only shows vibrational resonances in the bulk phonon spectrum and has no local vibrational modes. Carbon clusters based on the dicarbon antisite model have been proposed to be an appropriate model for the D_{II} center. For example, more carbon atoms can be bound together and form a cluster of four carbon atoms at a silicon site $(C_4)_{Si}$. Two dicarbon antisites can be created next to each other and form a pair of dicarbon antisites $((C_2)_{Si})_2$. These carbon clusters have a much richer phonon spectrum. However, the authors pointed out the difficulty with this model in that none of the considered defect complexes can explain all features of the D_{II} center. The model of the dicarbon antisites and carbon clusters generated by the dicarbon antisites is an attractive possibility. This same model of a pair of dicarbon antisites $((C_2)_{Si})_2$ has also been calculated and assigned as the origin of the D_{II} center in another theoretical paper by A. Gali et al. [13] by comparing the calculated local vibrational modes with the experimental values.

C.2 EXPERIMENT AND RESULTS

C.2.1 Experiment

The sample we used for this study is a homo-epitaxial 3C SiC thin film grown in the [001] direction. The nitrogen concentration is on the order of 10^{16} cm^{-3}. Aluminum implantation was done at room temperature at the University of Erlangen. The aluminum concentration is $1x10^{18}$ cm^{-3} and penetrates 1 μm deep. The sample was annealed at 1500 °C for 30 min.

Figure C.1 shows the X-ray transmission Laue pattern from this sample. A Philips X-ray generator was used at 40 kV and 15 mA. A crystal-to-film distance of 3 cm was used and a Polaroid type-57 (ASA 3000) black and white film was used to record the Laue pattern. The exposure time was 5 min. All the directions are marked on the picture based on the review paper published by Choyke et al. [50].

Since the company Polaroid stopped making the instant films in 2008, we are going to replace the instant film cassette with a Photonic Science Laue X-ray Imaging camera system from Micro Photonics Inc. This system has an active input area of 143.52 mm x 96.04 mm with a 1913 x 1280 pixel resolution. Pictures will be captured on a PC with FireWire interface card installed.

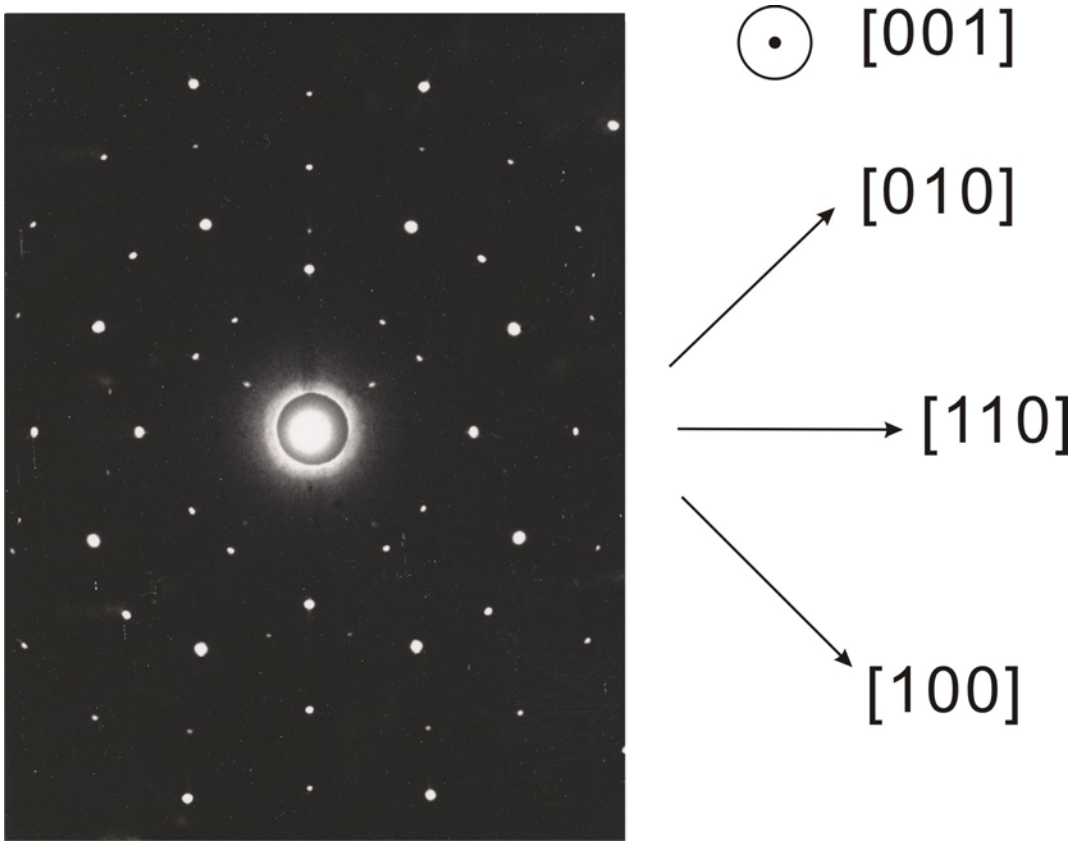

Figure C.1 Transmission Laue pattern photograph of the aluminum implanted 3C/3C SiC (40 kV, 15 mA, 5 min exposure, crystal to film distance 3 cm).

Photoluminescence measurements were made at different temperatures between 2 K and 50 K by mounting the sample in a Janis SuperVariTemp cryostat (Model 8DT) and flowing He vapor over it. We also have a Janis split coil superconducting magnet cryostat (Model 12CNDT) which can operate up to seven Tesla. We run the magneto optics LTPL from 0 to 6 Tesla in 0.5 Tesla steps. The FreD laser (244 nm) was used for the excitation source since the implanted layer is only 1 μm thick. The luminescence from the sample was imaged onto a liquid nitrogen cooled CCD array mounted on the focal plane of a two-meter Baird-Atomic high-resolution (0.05 Å) spectrometer.

In the magneto optics study on 4H or 6H SiC grown along the c direction, people usually use two different configurations with the magnetic field either perpendicular or parallel to the c

axis. In our case, we are studying 3C SiC, which is isotropic. But since we are all set up to run the experiment, we used the similar configurations with the magnetic field either perpendicular or parallel to the sample surface, which are shown in Figure C.2.

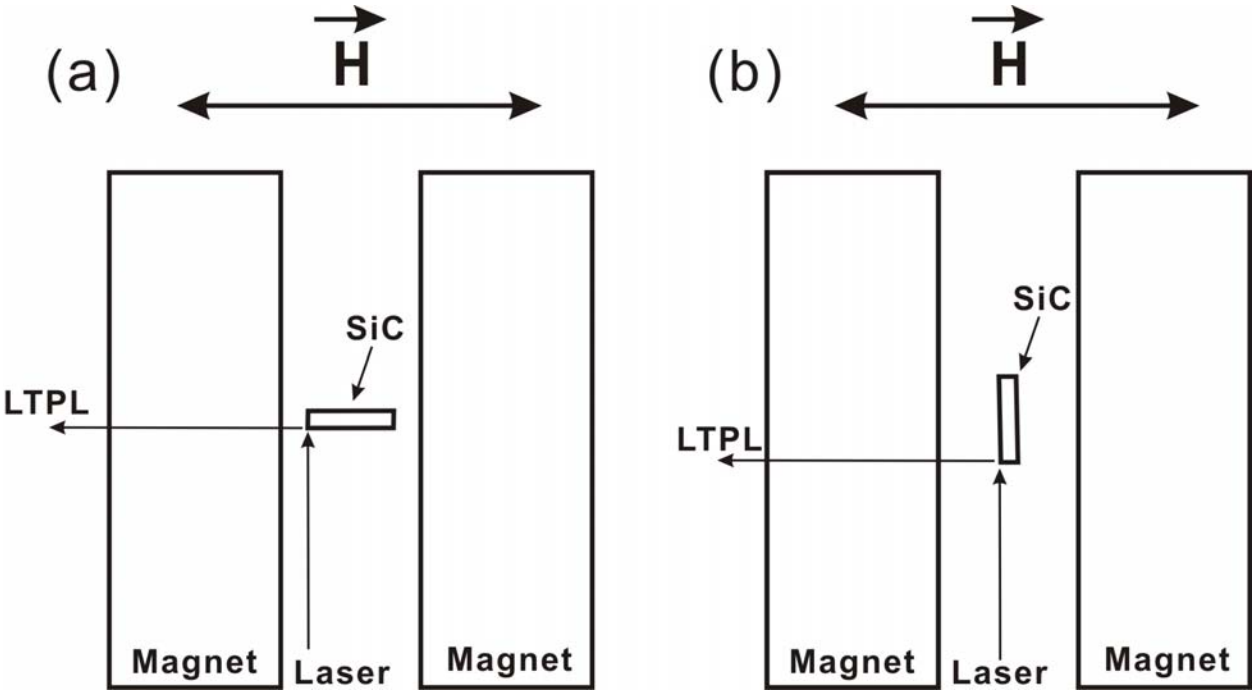

Figure C.2 Two different configurations we used for the magneto optics study on 3C SiC (a) H parallel to the sample surface of [001] plane; (b) H perpendicular to the sample surface of [001] plane.

C.2.2 High-Resolution LTPL Spectra from the D_{II} Defect Center in 3C SiC at Different Temperatures

The photoluminescence of the D_{II} defect center in aluminum implanted 3C/3C SiC is collected at different temperatures between 2 K and 50 K. Figure C.3 shows the temperature dependence of the no phonon lines of the D_{II} center. When the D_{II} center in 3C was first reported by Choyke et al. in 1973 [20], only one no phonon line was reported. In that paper the photoluminescence was collected at 1.3 K. As can be seen in our results in Figure C.3, we observed two no phonon lines

at 5372.36 Å (2.3072 eV) and 5370.31 Å (2.3081 eV) and labeled them as D_{II}^{1} and D_{II}^{0}, respectively. They are the no phonon lines from an excited state and the ground state of the D_{II} center. Using the experimental bulk excitonic band gap value of 3C SiC E_{GX} = 2.390 eV at 2 K [51], we obtain the binding energies of these two states are 82.8 meV and 81.9 meV with respect to E_{GX}. At the temperature of 1.3 K, the no phonon line of the excited state is probably too weak to be observed. That might be the reason why it was not reported in Ref. [20].

At low temperatures, the ground state no phonon line D_{II}^{0} dominates the spectrum. At intermediate temperatures, the intensity of the ground state line D_{II}^{0} decreases and the intensity of the excited state line D_{II}^{1} increases. At relatively high temperatures, the D_{II}^{1} line dominates the spectrum. Further increasing of the temperature leads to the quenching of these two peaks and the slight shift of less than 0.5 Å to the high wavelength direction due to the lowering of the band gap as the temperature goes up [52, 53]. When the temperature goes above 20 K, we start to see a really small peak at around 5362 Å. It is always very weak between 20 K and 54 K but it is definitely not seen at temperatures below 20 K. This peak also quenches when the temperature goes above 54 K. An example of this peak at 40 K is shown in Figure C.4 and marked with an arrow.

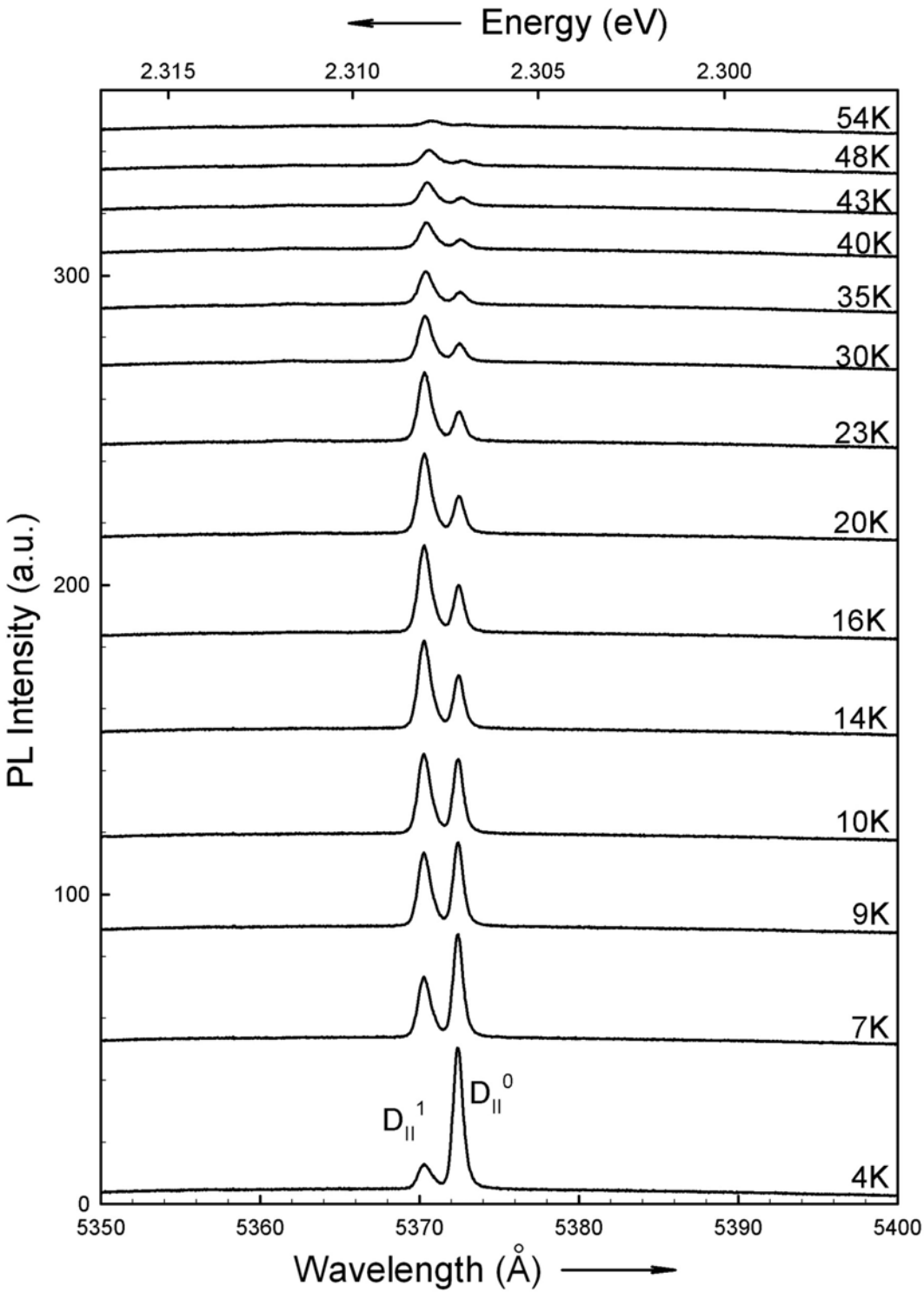

Figure C.3 High resolution LTPL spectra at different temperatures from the aluminum implanted 3C/3C SiC. The temperature is indicated on the right side of the figure. D_{II}^{1} and D_{II}^{0} are the no phonon lines from the excited state and ground state of the D_{II} center.

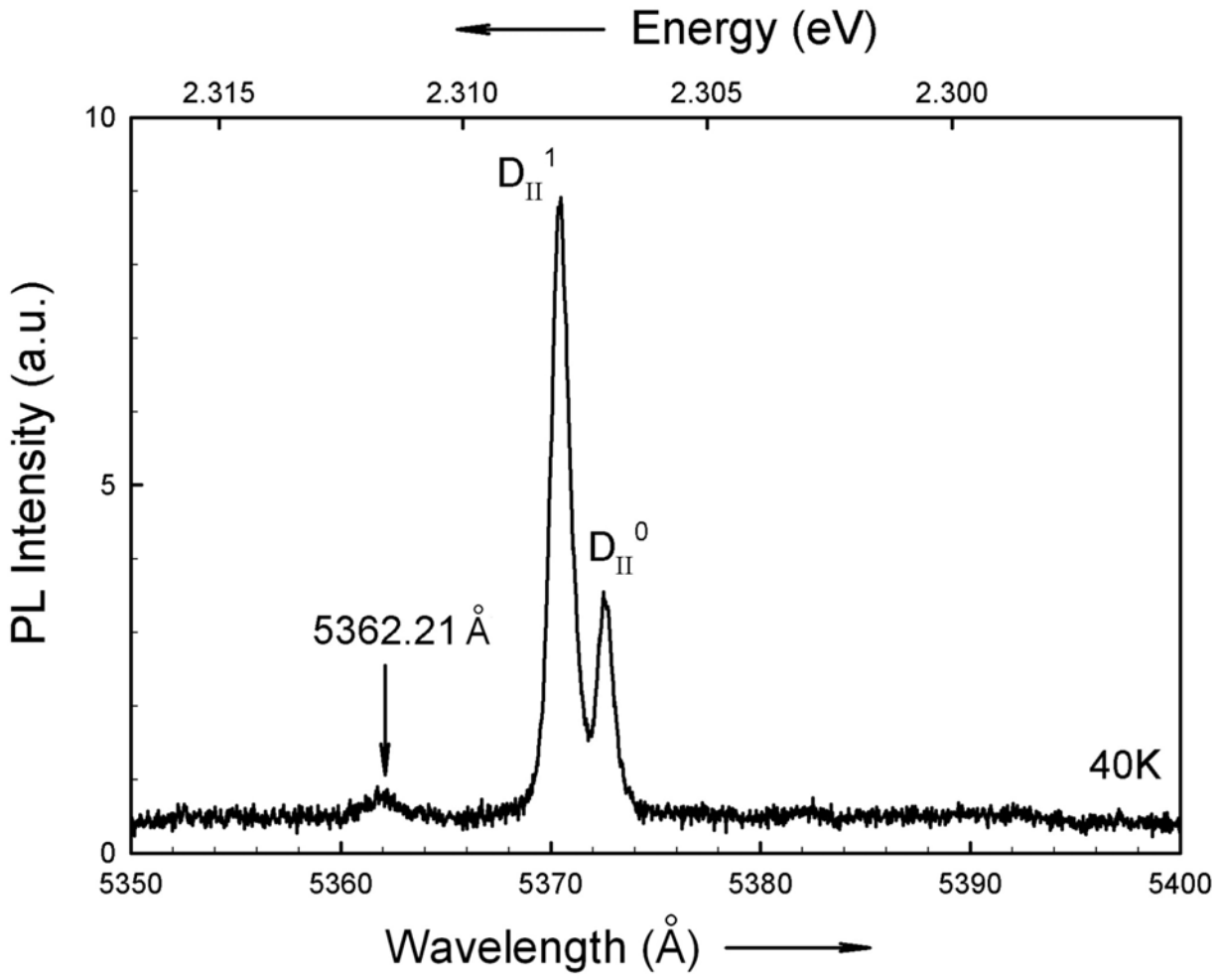

Figure C.4 High resolution LTPL spectra at 40 K from the aluminum implanted 3C/3C SiC. D_{II}^{1} and D_{II}^{0} are the no phonon lines from the excited state and ground state of the D_{II} center. The peak at 5362.21 Å is marked with arrow and is only observed at temperature higher than 20 K and quenches at 54 K.

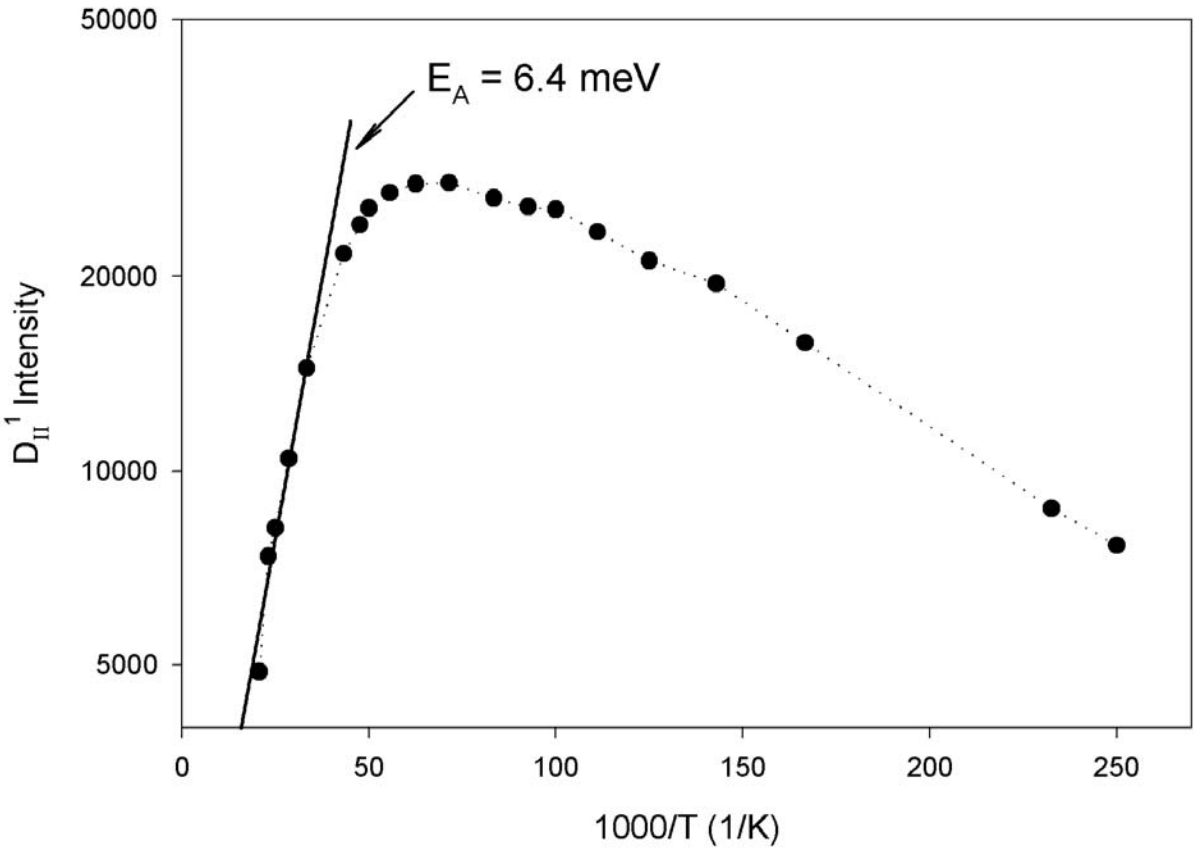

Figure C.5 Arrhenius plot of the temperature dependence of the intensities of the excited state no phonon line D_{II}^1 from 4 K to 54 K. The thermal activation energy E_A = 6.4 meV is calculated from the slope of the linear fit to the five leftmost points.

Figure C.5 shows an Arrhenius plot of the temperature dependence of the excited state no phonon line D_{II}^1 from 4 K to 54 K. The five leftmost data points are used for the linear fit and the thermal activation energy E_A = 6.4 meV is calculated from the slope. We have calculated the binding energies of the excited state and the ground state as 82.8 meV and 81.9 meV. In order to compare with the thermal activation energy, we have to consider the free exciton binding energy, which has been calculated and has a value of 26.7 meV [54]. The thermal activation energy is significantly smaller than the localization energy of the D_{II} bound exciton. A possible explanation is that the D_{II} defect center is an isoelectronic center. Either the hole or the electron in the exciton is weakly bound to the D_{II} center and the other one is tightly bound. The

quenching of the spectral lines is caused by the loose binding of the weakly bound particle when the temperature increases. This is consistent with the theoretical paper published by Gali et al. [13], in which they proposed that the D_{II} center is an isoelectronic center and the hole is more localized than the electron which is in an effective-mass state around the hole. Sridhara et. al also proposed that the D_{II} spectrum is from bound exciton recombination at isoelectronic centers from the photoluminescence study on the ion-implanted 6H SiC [55].

Figure C.6 is the Arrhenius plot of the intensity ratio of D_{II}^{1}/ D_{II}^{0} at temperatures between 4K and 54K. The intensity ratio follows the Boltzmann statistics and should follow the equation $\frac{I^1}{I^0} \propto \exp(-\frac{\Delta E}{kT})$, where ΔE is the activation energy of the excited state. On a semi-log plot of $\mathrm{Log}(\frac{I^1}{I^0})$ as a function of $1000/T$, the slope from the linear fit is $\frac{\Delta E}{k \cdot 1000}$. From the fitting results, we get ΔE = 1.1 meV. The measured spectrum shows a separation of 1 meV between the excited state and the ground state, which agrees well with the linear fitting result. We can use the fitting results to do a quick calculation of the intensity ratio at 1.3 K. Our result shows that at 1.3 K, the intensity of the D_{II}^{1} is 1/10000 of the intensity of D_{II}^{0}. This explains why the excited state is not observed in Ref. [20].

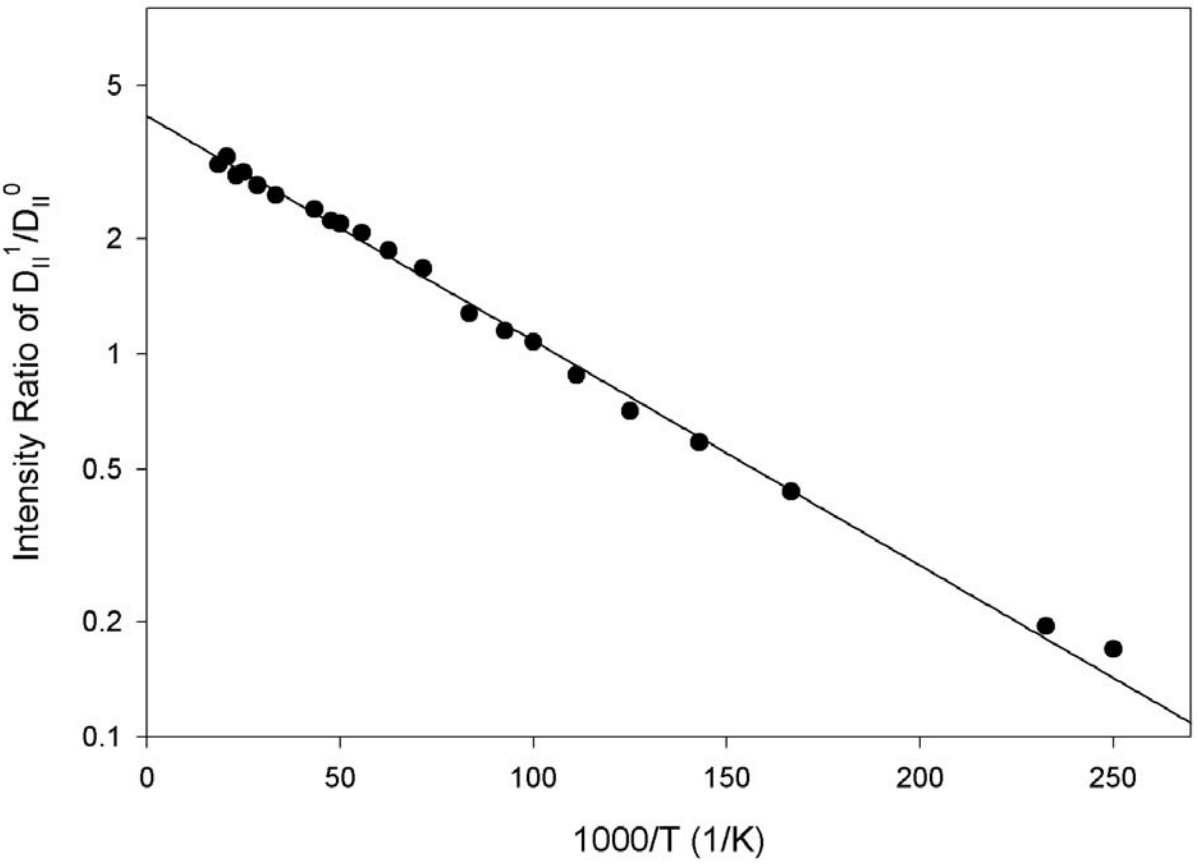

Figure C.6 Arrhenius plot for the intensity ratio of D_{II}^{1}/ D_{II}^{0} at temperatures between 4K and 54K. The activation energy from the slope of the linear fit agrees well with the energy separation of the no phonon lines in the LTPL spectrum.

C.2.3 High-Resolution Zeeman Spectra from D_{II} Defect Center in 3C SiC

Figure C.7 and Figure C.8 show the Zeeman splitting of the excited state and ground state of the D_{II} center in 3C SiC for both H parallel to the sample surface and H perpendicular to the sample surface. It is obvious that the excited state line D_{II}^{1} does not split, while the ground state line D_{II}^{0} shows clear splitting into two lines, which are about the same intensity.

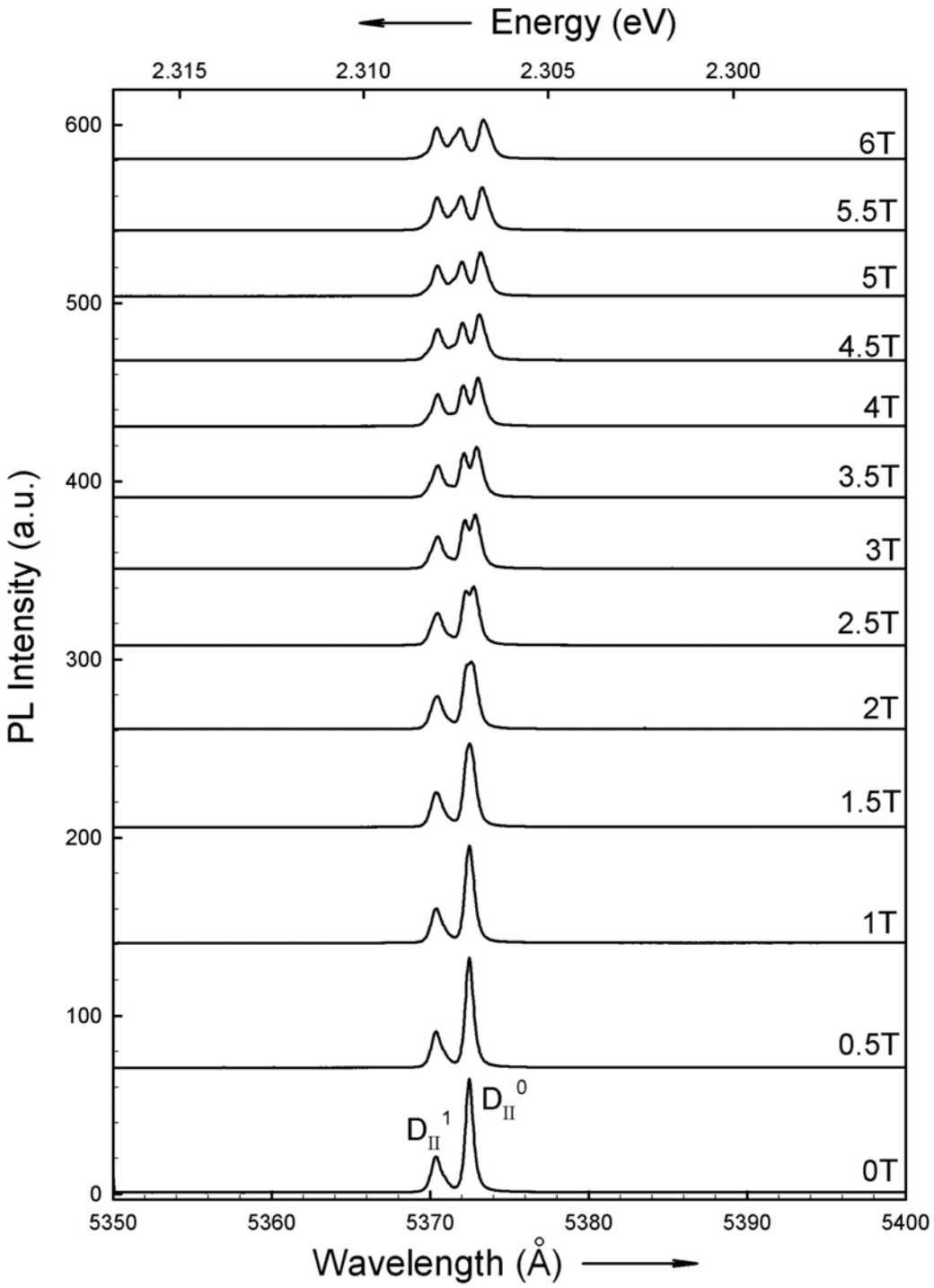

Figure C.7 High resolution LTPL spectra at different magnetic fields from the aluminum implanted 3C/3C SiC with $\vec{H}$ parallel to the sample surface. The magnetic field is indicated on the right side of the figure. D_{II}^{1} and D_{II}^{0} are the no phonon lines from the excited state and ground state of the D_{II} center.

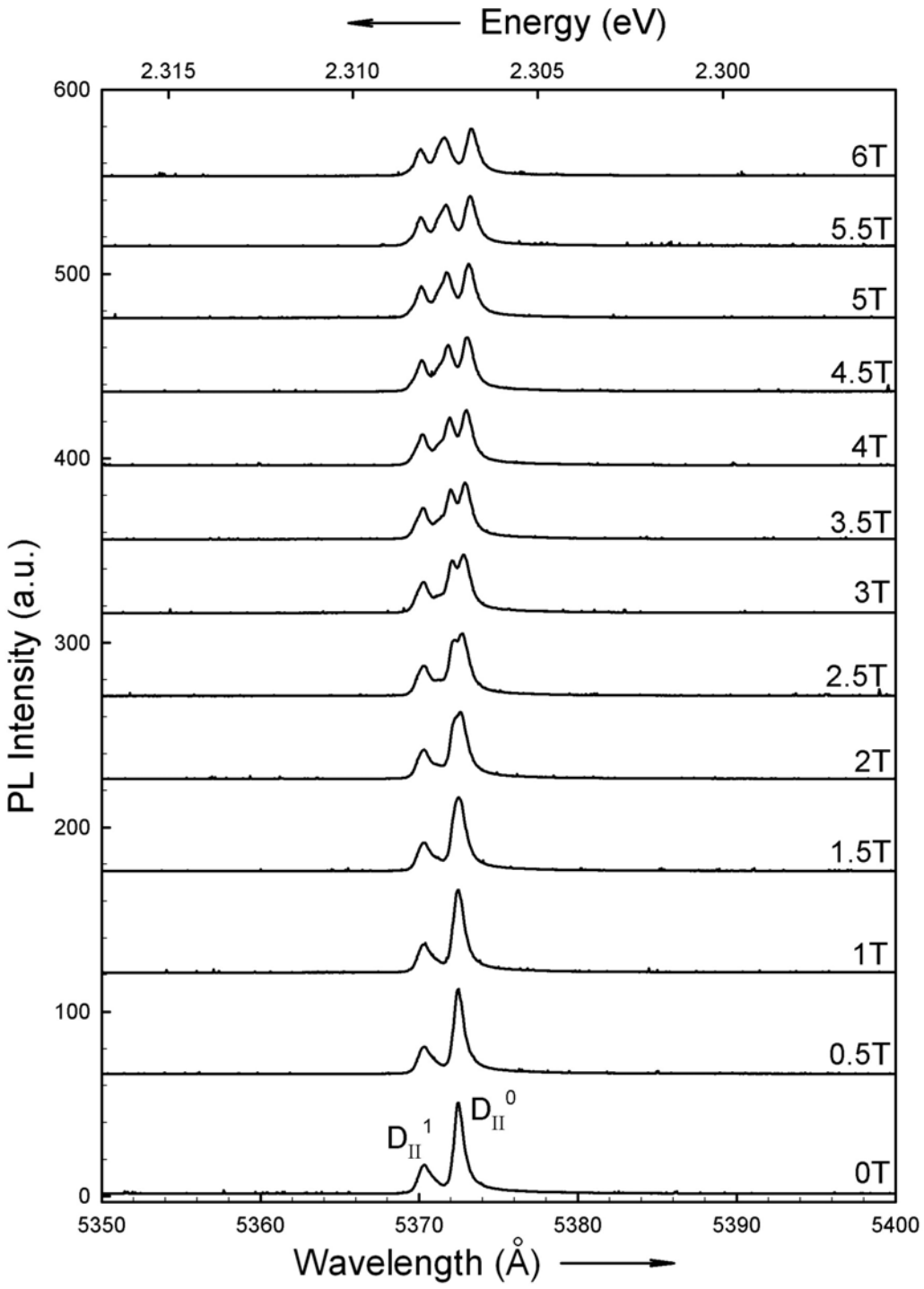

Figure C.8 High resolution LTPL spectra at different magnetic fields from the aluminum implanted 3C/3C SiC with $\vec{H}$ perpendicular to the sample surface. The magnetic field is indicated on the right side of the figure. D_{II}^{1} and D_{II}^{0} are the no phonon lines from the excited state and ground state of the D_{II} center.

Figure C.9 and Figure C.10 are the fan diagrams obtained from the Zeeman spectra shown in Figure C.7 and Figure C.8, respectively. They show the energies of the peaks versus the magnetic fields. Assuming a linear Zeeman effect, we can find the values for the magnetic g-factor from the formula:

$$g = \frac{\Delta E}{\mu_B \cdot \Delta H}$$

where μ_B = 5.79 x 10^{-5} eV/T is the Bohr magneton and ΔE is the splitting of each peak. The magnetic g-factor is 2.20 for H parallel to the sample surface and 2.63 for H perpendicular to the sample surface. It is unclear at this time why these two values are different. 3C SiC has an isotropic crystal structure. It shouldn't make a difference whether H is parallel or perpendicular to the sample surface. The other interesting phenomenon in these two fan diagrams is the splitting from 2 T to 6 T is somewhat linear. But if we draw two lines through these data points, they intersect each other at 1.5 T. So the Zeeman splitting only starts happening from 1.5 T, which can also been seen in Figure C.7 and Figure C.8. However, if we look at the Zeeman spectra with weak magnetic fields carefully, we can see that at 0.5 T, 1.5 T and 2.0 T, the ground state no phonon line is actually getting broader as the magnetic field goes up. The splitting is just not big enough to be separated even by our high resolution spectrometer. Therefore, the splitting does not seem to be linear at the small magnetic field and the magnetic g-factors calculated from the fan diagrams using the above linear equation may not mean anything. The D_{II} center is probably too complicated to use the simple equation to calculate the g-factor.

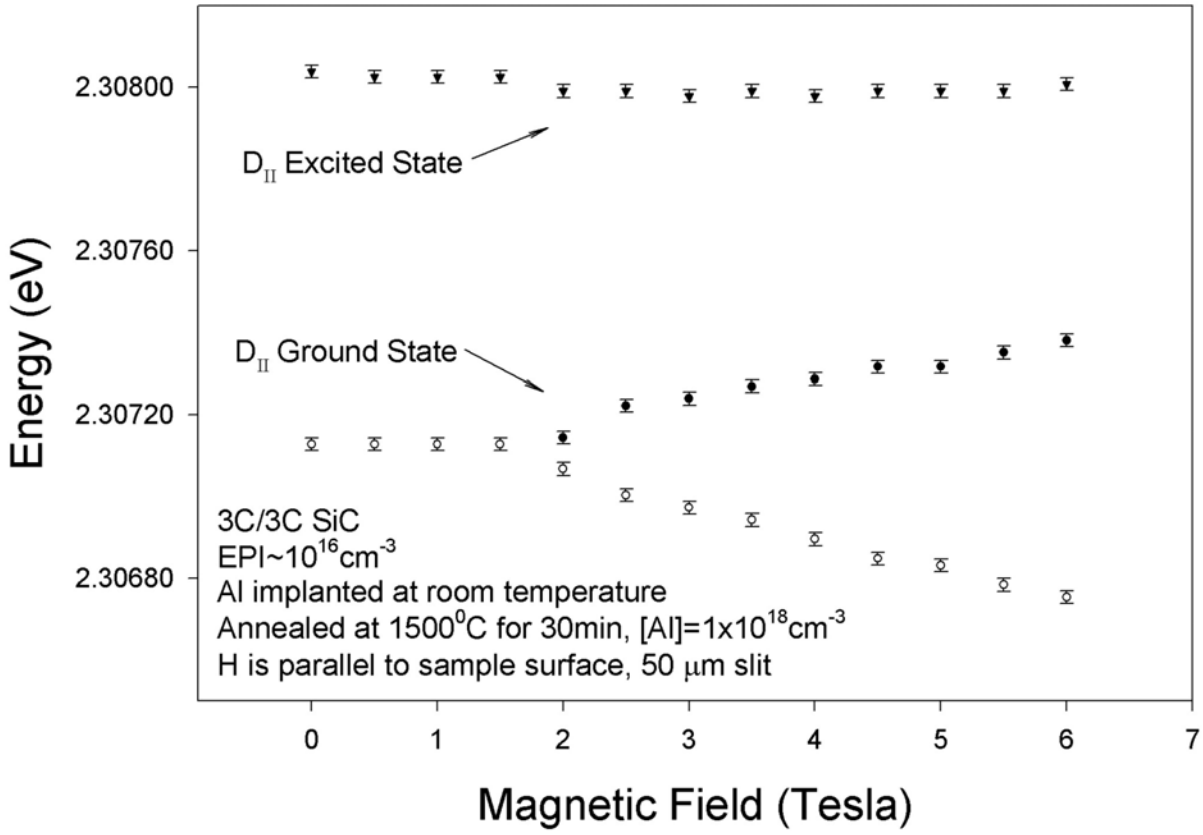

Figure C.9 Fan diagram obtained from the Magneto-Optics spectra for the D_{II} center from the aluminum implanted 3C/3C SiC with $\vec{H}$ parallel to the sample surface.

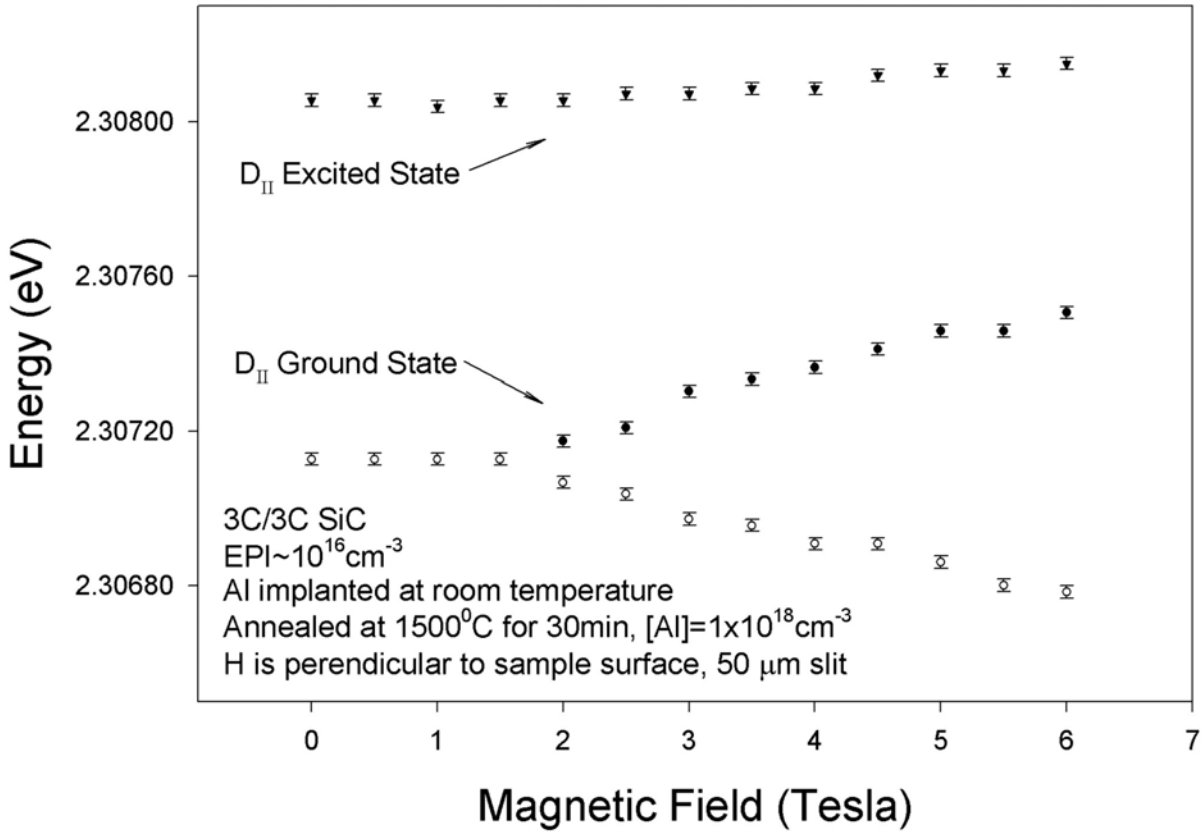

Figure C.10 Fan diagram obtained from the Magneto-Optics spectra for the D_{II} center from the aluminum implanted 3C/3C SiC with the $\vec{H}$ perpendicular to the sample surface.

We also measured the dependence of the Zeeman spectra on the angle θ between the magnetic field H and the direction normal to the crystal surface. Figure C.11 shows the diagram of the angle dependence we used in the setup. θ is the angle between the direction in which the luminescence was detected and the sample surface normal direction. Figure C.12 shows the angle dependence of the three peaks at H = 6 T. Each of them stays at the same energy position from 0 T to 6 T. This is what we should expect because 3C SiC has an isotropic crystal structure.

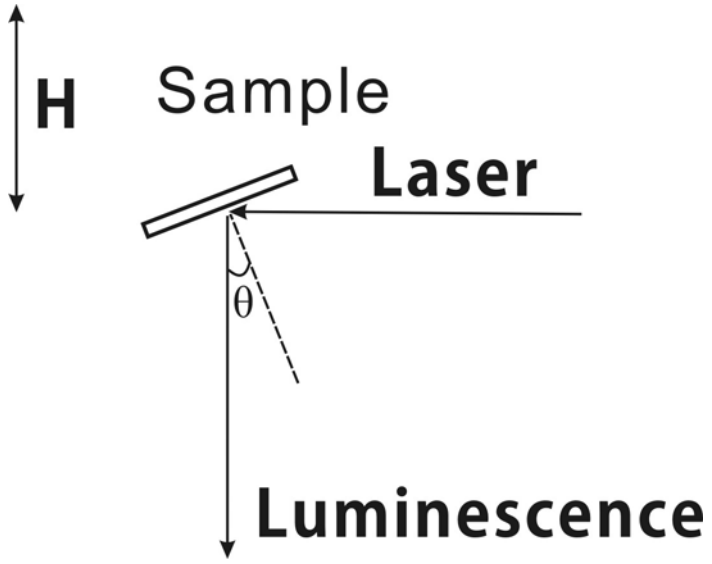

Figure C.11 Schematic diagram of the setup for the angle dependence.

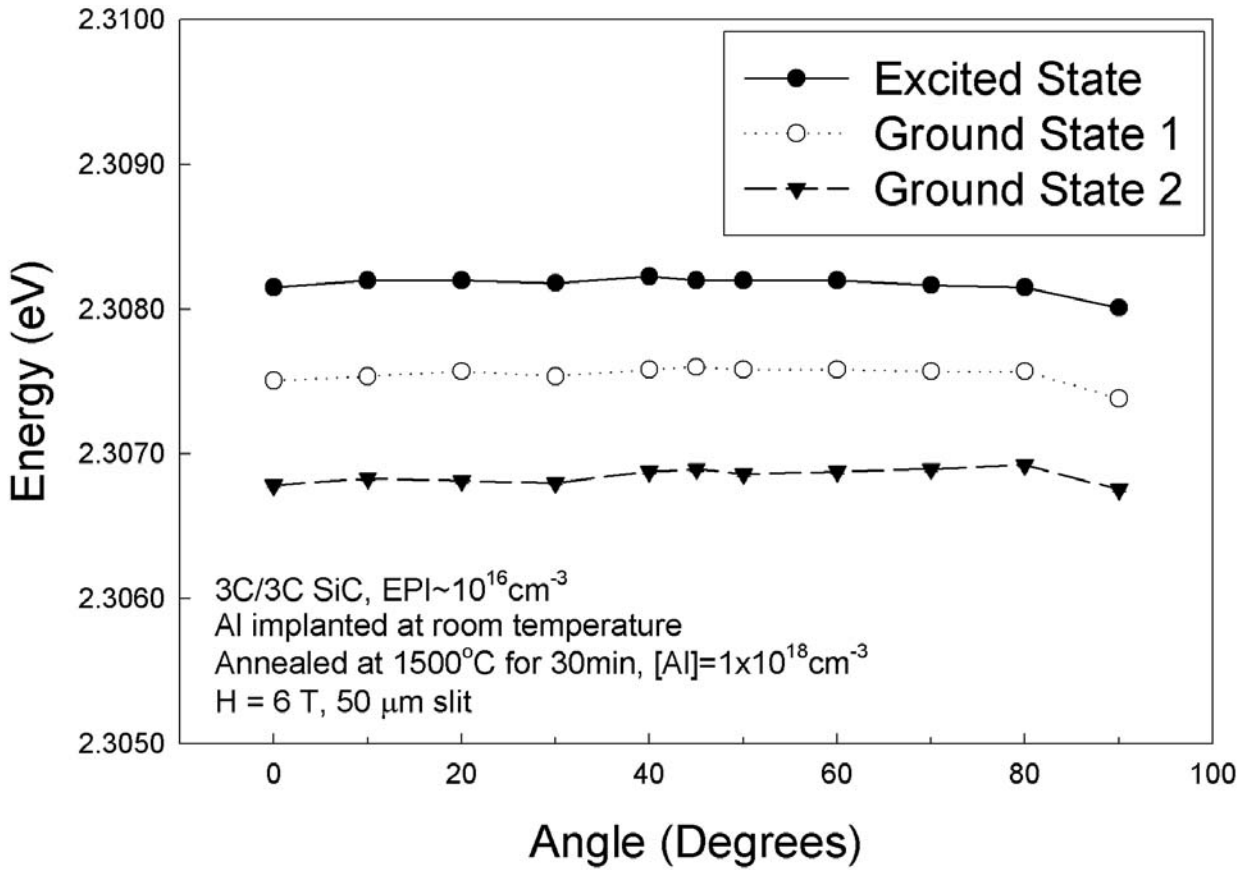

Figure C.12 Angle dependence of the H = 6 T Zeeman spectrum on the angle between the magnetic field and the direction normal to the crystal surface.

S. G. Sridhara et al. has done the Zeeman spectroscopic measurements on the D_{II} defect center in 6H SiC [55]. They didn't observe any splitting on all the four no phonon lines from D_{II}^{6H} at a magnetic field up to 5 T. A. Henry et al. reported that no splitting was seen in the case of the D_{II} spectrum in 4H SiC [56]. Our work represents the first systematic study of the D_{II} defect center in 3C SiC. As far as we know, the splitting of the D_{II} defect line is seen for the first time in any of the SiC polytypes.

Since the D_I center and the D_{II} center are two persistent intrinsic defect centers in SiC after ion implantation and high temperature annealing, it is instructive to compare the Zeeman spectra of these two. W. J. Choyke et al. did the first work on the D_I center in 6H SiC in 1979

[57]. T. Egilsson *et al.* studied the D_I center in 3C and 4H SiC in 1999 [29]. In those two papers, the authors didn't see any splitting of the high temperature (excited state) lines. They did observe the splitting of the low temperature L_i lines. For the case of D_I in 3C SiC, the authors did not observe any angular dependence and concluded that it is isotropic [29]. All these observations are similar to our results for the D_{II} in 3C SiC. Combining the results with our variable temperature experiments, we conclude that the D_{II} defect is also an isoelectronic center, even though he atomic structures of the D_I and D_{II} defects are different from the theoretical models. In the fan diagram in Figure 3 in Ref. [57], it is shown that the splitting of L_1^0 in 6H SiC is linear from 2 T up to 10 T. At the weak magnetic field end, the authors didn't show any data point, which is probably because they didn't observe any clear splitting. This is also similar to our experimental results from D_{II} in 3C SiC. However, a lot of work has been down on the shallow donors and shallow acceptors in SiC and the Zeeman splitting is always linear for the shallow dopants. P. J. Dean et al. studied the magneto-optical properties of the three no phonon lines of nitrogen shallow donors in 6H SiC and the splitting is linear between 0 T and 3 T [58]. R. P. Devaty et al. studied the Zeeman spectra of the aluminum and gallium shallow acceptors in 6H SiC and observed linear splitting between 0 T and 6 T [59]. Therefore, we can speculate that the Zeeman splitting is linear for the shallow donors and acceptors. For the deep defect centers like D_I and D_{II} in SiC, it only shows linear splitting with a magnetic field stronger than 2 T and above.

APPENDIX D

LOW TEMPERATURE PHOTOLUMINESCENCE STUDY OF PHOSPHORUS DOPING IN SILICON CARBIDE

D.1 INTRODUCTION

As has been introduced in the first chapter, SiC is believed to be suitable for electronic and optical use under high temperature, high frequency and high power conditions. In order to improve its performance in devices, good material quality and doping properties must be achieved. However, the doping incorporation in SiC is far more difficult than that in the silicon industry. Nitrogen is the most commonly used n-type dopant in SiC. People have extensively studied the mechanism of nitrogen incorporation in SiC during chemical vapor deposition (CVD) growth and proposed the site-competition theory to control the nitrogen incorporation [60-62]. Phosphorus is another possible dopant for n-type doping SiC material. But people haven't made it clear how phosphorus is incorporated into SiC lattice. Larkin reported that phosphorus should mainly occupy the silicon sites because its atomic size is much bigger than the carbon atom. The CVD growth of 6H SiC showed that the incorporation of phosphorus is consistent with the site competition effect by varying the Si/C ratio and assuming that phosphorus atoms occupy the Si-sites [62]. Sridhara *et. al.* reported LTPL spectra of phosphorus doped 6H-SiC and proposed that

phosphorus does substitute on the silicon site and does form neutral donor four particle bound exciton complexes [63]. However, recent research shows that there is a finite chance that phosphorus also substitutes for carbon sites. Electron paramagnetic resonance (EPR) studies have been performed on 6H SiC after high energy phosphorus ion implantation and post-implantation high temperature annealing [64]. EPR signals of phosphorus shallow donors at both carbon and silicon sites were observed, with the former with much stronger intensity. Wang *et. al.* studied the phosphorus incorporation behaviors in CVD growth using techniques of mercury probe *C-V* measurements and secondary ion mass spectrometry (SIMS) [65]. They proposed that phosphorus could incorporate into both carbon and silicon sites depending on the C/Si ratio during growth. In certain range of C/Si ratio, phosphorus might occupy the carbon sites, too. Meanwhile, according to a recent theoretical finding the second most abundant phosphorus-related defect is phosphorus substituting on the carbon site (P_C) in CVD SiC samples [66, 67]. In this chapter I will give low temperature photoluminescence results on 6H and 4H SiC, which indicate that, contrary to nitrogen which substitutes only on the carbon sublattice, phosphorus can substitute on both the silicon and carbon sites. I will also present some LTPL results from 15R and 3C SiC doped with phosphorus.

D.2 EXPERIMENT AND RESULTS

D.2.1 Growth of Phosphorus Doped SiC

The epilayers used for these experiments have been grown over a number of years by Dr. D. J. Larkin at the NASA Glenn Research Center and by Prof. I.B. Bhat at the Rensselaer Polytechnic

Institute (RPI). The NASA samples were phosphorus doped epitaxial layers grown on 4H, 6H, 15R and 3C boule substrates in an atmospheric pressure, cold-wall chemical vapor deposition (CVD) system and doped with phosphorus by the addition of phosphine into the reactor during growth. The phosphorus doping was controlled via the site competition effect. The RPI 4H and 6H SiC samples were also grown in a horizontal water-cooled CVD reactor. The SiC substrates were placed on TaC-coated high purity graphite susceptors. Pd-diffused hydrogen was used for carrier gas. SiH_4 (2% in H_2), C_3H_8 (2% in H_2) and PH_3 (0.1% in H_2) were used as the sources of Si, C and P respectively. Further growth details can be found in Ref. [65]. Mercury probe capacitance-voltage (*C-V*) measurements show the doping concentration N_D-N_A varies from $7.5x10^{15}$ cm^{-3} to $2.7x10^{16}$ cm^{-3}. Phosphorus concentration profiles were also measured by SIMS and they are in the order of 10^{16} cm^{-3}. Figure D.1 shows the SIMS depth profile of the nitrogen and phosphorus concentrations in one of the 6H SiC samples provided by the RPI group. It shows that the phosphorus doping concentration is on the order of 10^{16} cm^{-3} and the nitrogen doping concentration is on the order of 10^{15} cm^{-3}. The epilayer is primarily doped by phosphorus.

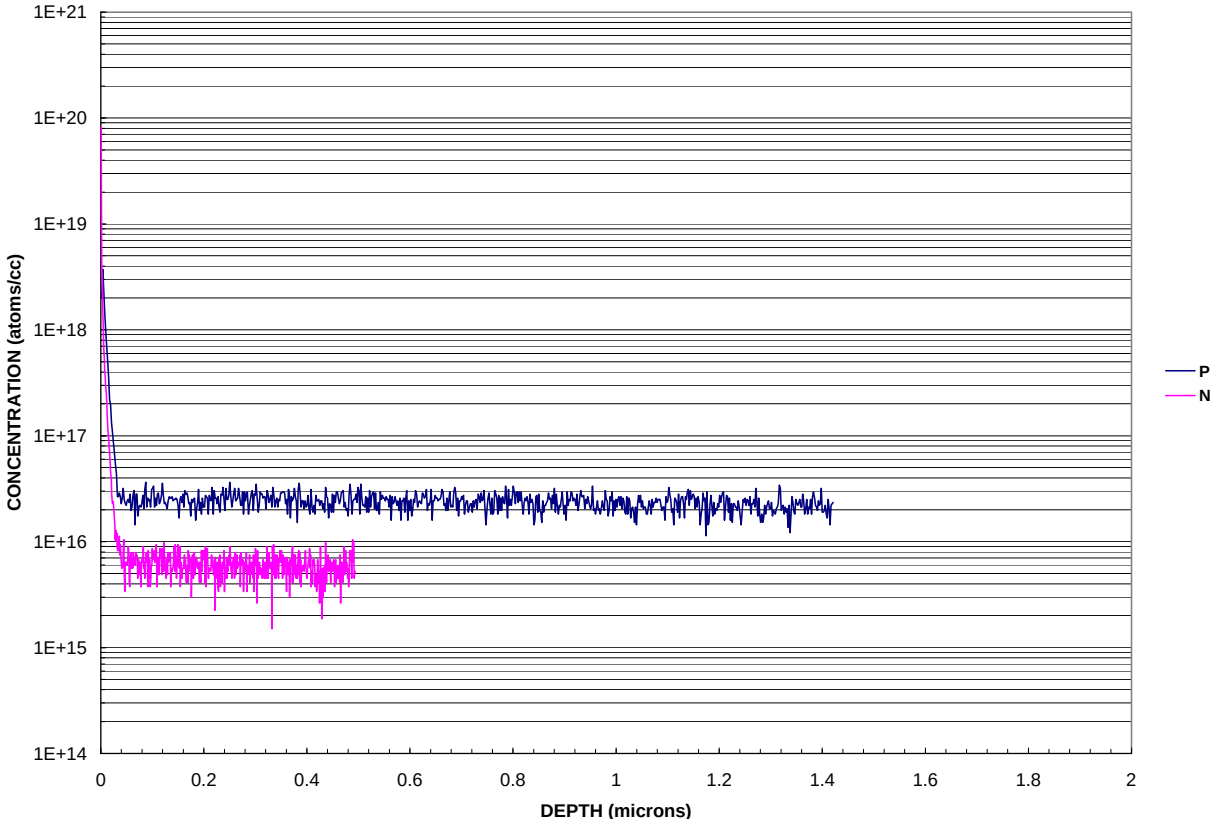

Figure D.1 SIMS depth profile of a phosphorus-doped 6H-SiC epilayer. It shows that phosphorus doping concentration is on the order of 10^{16} cm^{-3} while the nitrogen doping concentration is in the order of 10^{15} cm^{-3}.

D.2.2 Low Temperature Photoluminescence Experiment

For the phosphorus doping study, the low temperature photoluminescence measurements were carried out from 1.5 K to 2 K. For the study of the phosphorus doped samples, we always use the 244 nm FreD laser because we want to avoid the possible background signal coming from the nitrogen doped substrate. We tune the laser power as high as 60 mW so that we can see the relatively low intensity peaks which are of great interest in this project.

D.2.3 Phosphorus Doping in 6H SiC

Figure D.2 shows the full scale low temperature spectrum of a 6H SiC epitaxial film doped with phosphorus. It is dominated by the no-phonon and phonon replica lines from phosphorus on Si sites and looks similar to what has been published before in Ref. [63]. The letter h stands for the hexagonal site in the 6H SiC lattice. The letters k_1 and k_2 stand for the two quasi-cubic sites in the 6H SiC lattice. The superscript P stands for Phosphorus substituting as a donor in the 6H SiC lattice. We can also see two of the three nitrogen related no-phonon lines, R_0 and S_0. They are very small and buried underneath the phosphorus related spectrum, in agreement with the statement we made from the SIMS concentration depth profile that the sample is primarily doped with phosphorus.

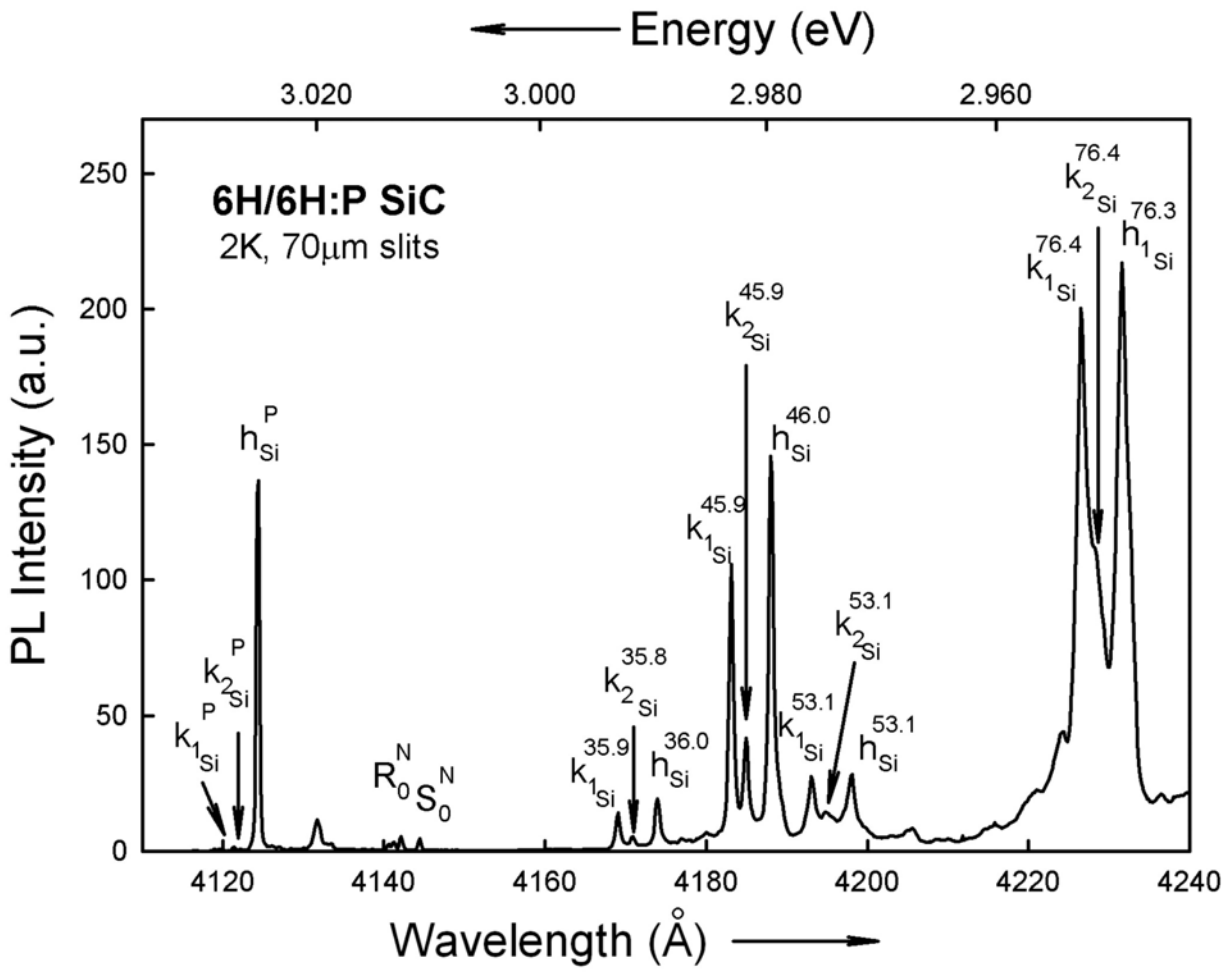

Figure D.2 LTPL spectra of 6H/6H SiC doped with phosphorus at 2K measured using the 244 nm line, at 60 mW, from a FreD laser.

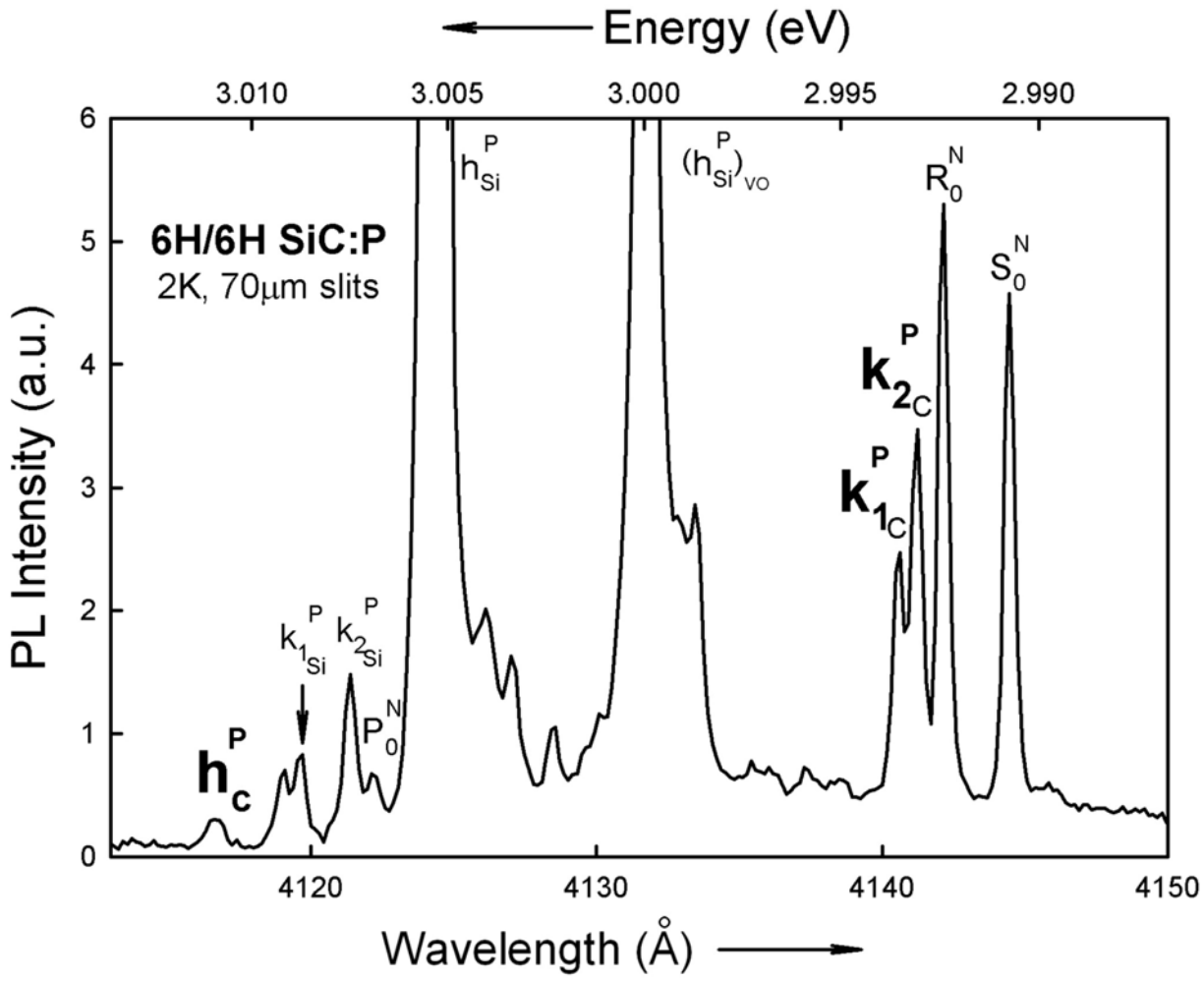

Figure D.3 No-phonon lines of 6H/6H SiC doped with phosphorus at 2K measured using the 244 nm line, at 60 mW, from a FreD laser.

In order to see more details we are going to check the spectrum in different wavelength ranges and blow them up to look at amplified scales. In Figure D.3, we can clearly see the lines associated with phosphorus substituting on the C sites. P_0^N, R_0^N and S_0^N are the no-phonon lines of the nitrogen donor bound exciton four particle complexes. The superscript N is used to make nitrogen-related lines distinguishable from the phosphorus-related lines. The spectrum, as expected from theory, is dominated by phosphorus substituting on the Si sites. A subscript Si is used to indicate the Si sublattice upon which the phosphorus donor is located. The important

thing is that there are some new lines that were not understood very well but we have known about them for some time. These new lines h_C^P, $k_{1C}^P$and k_{2C}^P are located at 4116 Å (3.0114 eV), 4140 Å (2.9940 eV) and 4141 Å (2.9932 eV). We assign them to the phosphorus donor substituting on the C sublattice. The exciton binding energies to the three new no-phonon lines are 12.1 meV, 29.4 meV and 29.9 meV. The similarity of the positions of the phosphorus donor lines on carbon sites to those of nitrogen on carbon sites suggests that the 4116 Å line be associated with the hexagonal site (h_C^P) and the 4140 Å and 4141 Å lines be associated with the two cubic sites (k_{1C}^P, k_{2C}^P). An arrow points to the peak we have designated as k_{1Si}^P. The nearby higher energy peak is not seen in some samples and is not as consistent with the phonon replica values of k_{2Si}^P and h_{Si}^P as is the assigned peak k_{1Si}^P. Un-identified peaks between h_{Si}^P and $(h_{Si}^P)_{VO}$ are seen in samples where h_C^P, $k_{1C}^P$and k_{2C}^P are not seen and hence are likely to be associated with phosphorus on Si sites.

In order to verify these assignments we have made a careful study of the momentum conserving phonon replicas associated with the no-phonon line h_C^P and those of k_{1Si}^P, k_{2Si}^P and h_{Si}^P. In the case of the phosphorus on the carbon sites we expect to see phonon replicas primarily from h_C^P in analogy with the situation for nitrogen donors, where P_0^N is the prime source of the phonon replicas at low temperature.

Phonon replicas of the phosphorus no-phonon lines of the carbon and silicon lattice sites are given in Figure D.4. Note that some of them are indicated here with arrows and are barely seen, but once we expand the intensity scale, they turn out to be well resolved peaks. Agreement of the phonon replica energies of the carbon sites with those on the Si sites is on the order of 0.5 meV, giving us a measure of confidence in our assignments.

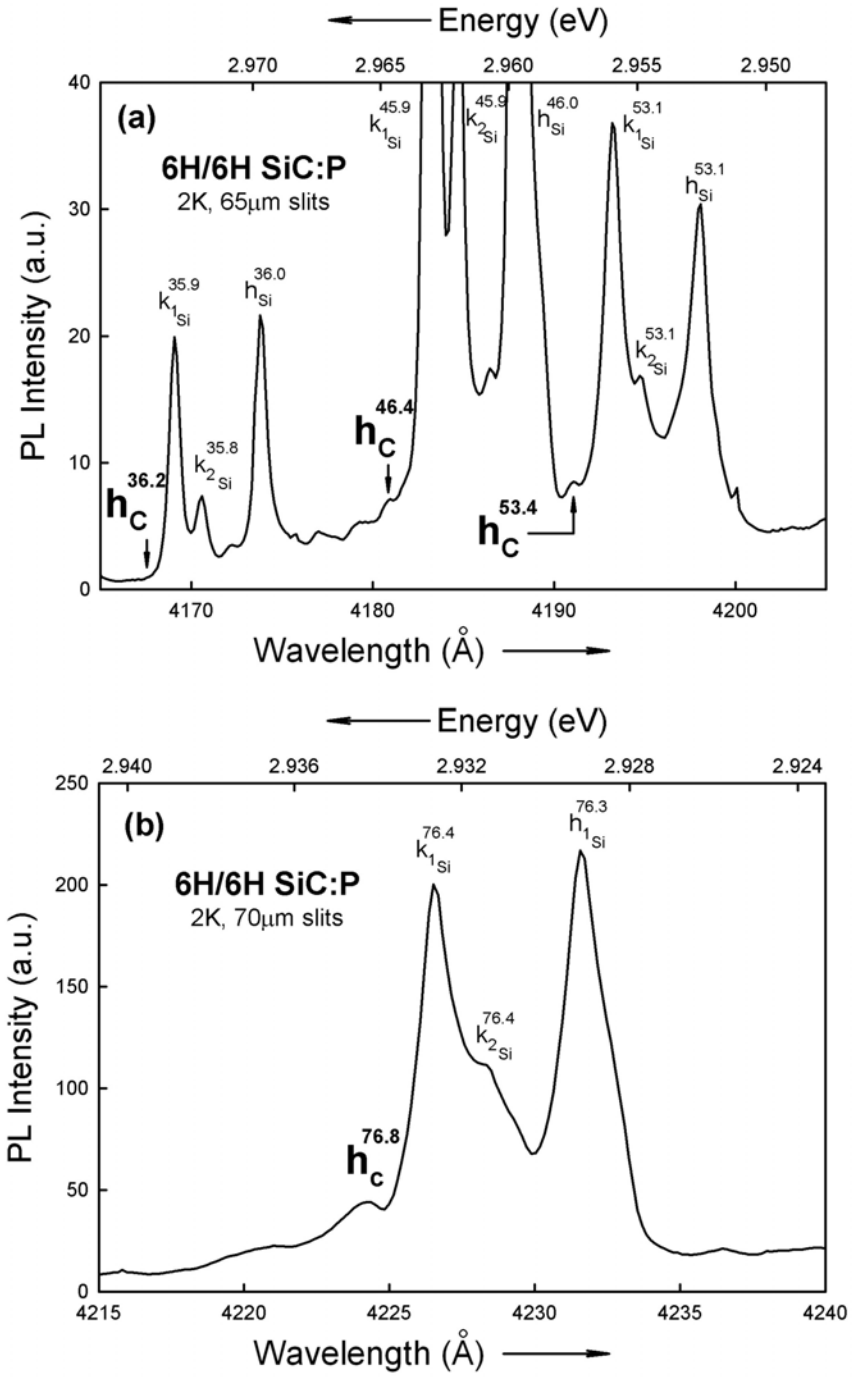

Figure D.4 Phonon replica lines of 6H/6H SiC doped with phosphorus measured at 2K using the 244 nm line, at 60 mW, from a FreD laser. Symbols labeling the lines are marked with superscripts specifying the momentum conserving phonon energies in meV. Subscripts indicate phonon replicas associated with phosphorus substituting on either the Si sublattice or the C sublattice. The phonon replicas attributed to phosphorus on the carbon sublattice is shown in bold type.

In a recently paper published by A. Henry et al. [68], the authors presented their low temperature photoluminescence results in phosphorus doped SiC. They observed the similar fine structures as in Figure D.3 in the region of the no phonon lines. We should notice that they plotted the PL intensity in log scale, which might make it look a little bit different from our spectra in terms of the intensity ratios. The authors assigned some of the new lines as the excited states and did not provide any explanation for the other new lines. We don't agree with this assignment and we believe it actually provided more evidence for our assignment of the phosphorus substituting on C sites.

D.2.4 Phosphorus Doping in 4H SiC

Figure D.5 (a), (b) and (c) are the LTPL spectra of a 4H SiC epitaxial film doped with phosphorus. Figure D.5 (a) shows the no-phonon lines due to the phosphorus donor bound exciton four particle complexes as well as the nitrogen donor. The P_0^N line of nitrogen is hidden under the phosphorus h_{Si}^0 line. This is understandable since normally P_0^N is observed to have 1/10th the amplitude of Q_0^N. Considering the intensity of Q_0^N, we can expect P_0^N to be relatively small. A careful study of the phonon replicas due to the phosphorus on Si and C sites has been carried out and is shown on Figure D.5 (b) and (c). This supports the assignments of the h_{Si}^0 and k_{Si}^0 lines. Unfortunately, the phonon replicas attributable to h_C^0 are too weak to be distinguished from those of h_{Si}^0 and hence our assignment of h_C^0 and k_C^0 must be taken as possible but not proven. For comparison, we include a nitrogen doped 4H SiC spectrum in Figure D.5 (d) with a doping concentration of $1x10^{16}$ cm^{-3}. It is seen that the phonon replicas due to nitrogen in Figure D.5 (b) are negligible compared to those of phosphorus. This rules out the impact from nitrogen doping.

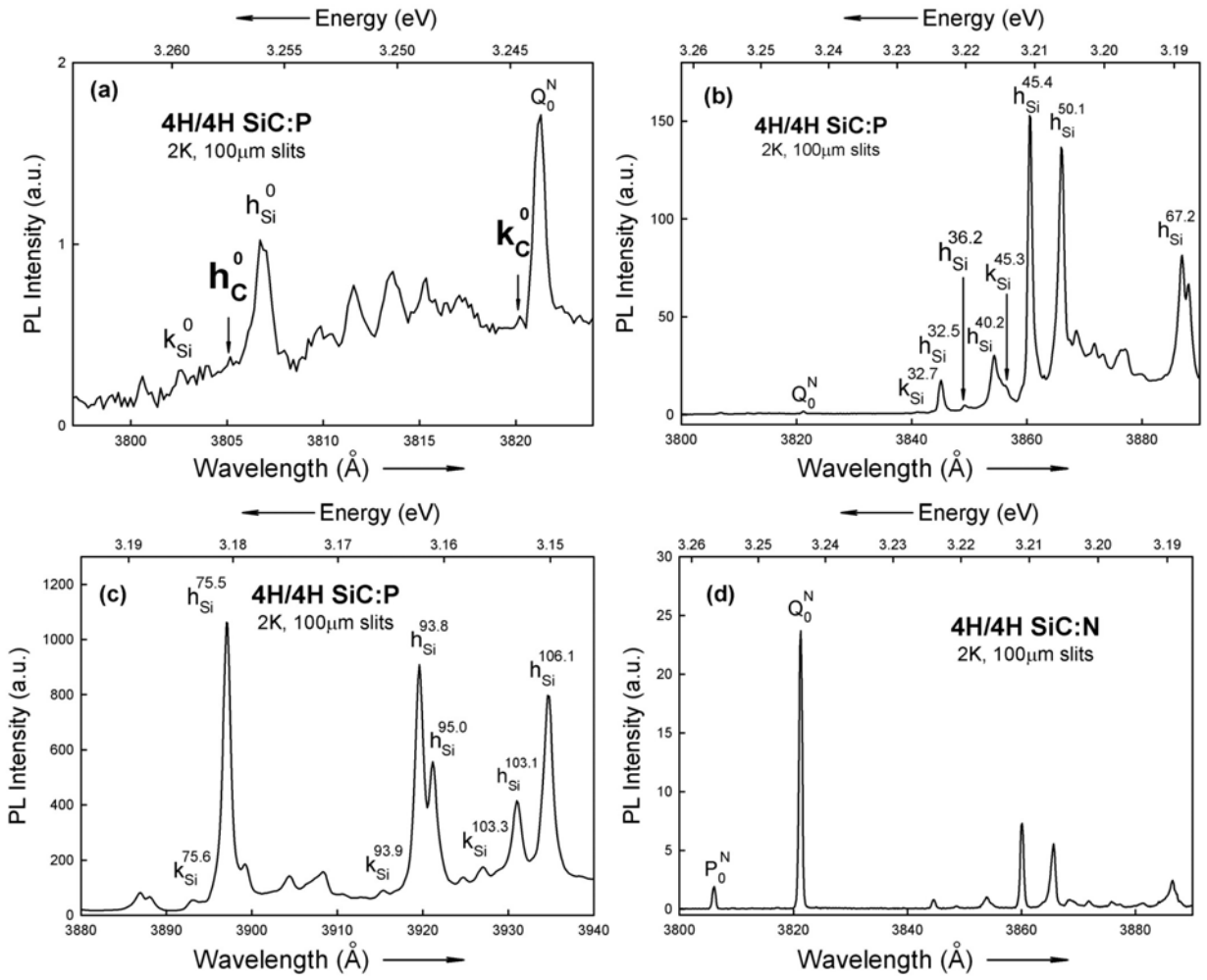

Figure D.5 (a), (b) and (c) LTPL spectra of 4H/4H SiC doped with phosphorus at 2K measured using the 244 nm line, at 60 mW, from a FreD laser. Symbols labeling lines are marked with superscripts specifying the momentum conserving phonon energies in meV. Subscripts indicate phonon replicas associated with phosphorus substituting on either the Si sublattice or the C sublattice. (d) LTPL spectra of 4H/4H SiC doped with nitrogen at 2K for comparison with (b) in the same wavelength region.

D.2.5 Phosphorus Doping in 15R SiC

15R SiC is a more complicated polytype than 4H and 6H SiC. It is very difficult to identify the phosphorus lines in 15R SiC. In Figure D.6 the top spectrum (a) is from a sample doped with

phosphorus. The bottom spectrum (b) is from a regular nitrogen doped sample. They look totally different. We are confident to say that the spectrum (a) is due to phosphorus doping. There are five inequivalent sites in 15R SiC lattice and five no phonon lines are expected. But so far in the literature people have found only four no phonon lines in the nitrogen doped 15R SiC spectrum [69]. The last one is missing. People are not very sure about the nitrogen doping mechanism in 15R SiC. It makes it even more difficult to identify the phosphorus lines. We cannot identify the different substitution sites in this case.

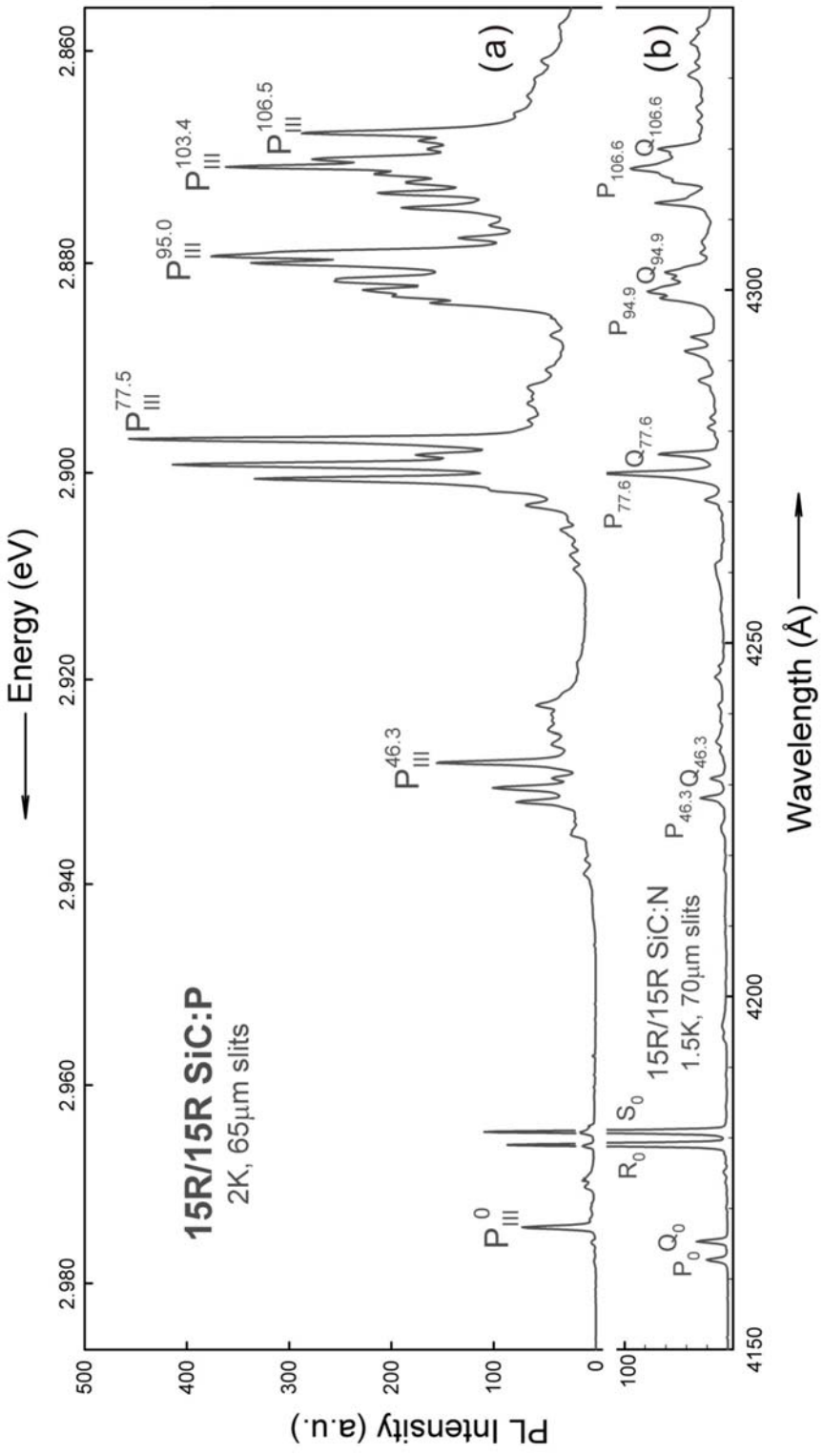

Figure D.6 (a) LTPL spectra of 15R/15R SiC doped with phosphorus at 2K; (b) LTPL spectra of 15R/15R SiC doped with nitrogen at 2K in the same wavelength region.

D.2.6 Phosphorus Doping in 3C SiC

Our collaborator Dr. Larkin at the NASA Glen Research Center was able to put high quality phosphorus doped 3C-SiC epilayers on 3C-SiC substrates. We haven't done any SIMS doping concentration profile on the 3C-SiC samples, but we can definitely see some new lines in the LTPL spectra, which are shown in Figure D.7. Figure D.7 (a) is the near band-edge part of the spectrum. Besides some well-known nitrogen lines, we can see some new sharp lines right below the nitrogen lines in wavelength. The line labelled as N_0 at 5210.81 Å (2.3787 eV) is the no phonon line from recombination of excitons bound to the nitrogen donors. There is an extra line on the high energy shoulder of the N_0 line, labelled as X_0 at 5210.13 Å (2.3790 eV) and is only 0.3 meV above the N_0 line. We think it might come from recombination of excitons bound to the phosphorus donors. But it is not proven to be absolutely true because there is a controversy about these sharp lines. During our study of some other samples from two other different growth groups, we have also seen these features. However those samples were not intentionally doped with phosphorus and we don't have any evidence that there could be any phosphorus contamination in the reactors. One grower is IKZ in Germany. They tried to grow an epitaxial layer on a porous 6H SiC substrate and got yellow 3C thin films instead. The other grower is HOYA in Japan. That was 3C epitaxial layer on regular 3C substrate. Therefore we cannot mark these lines Phosphorus related. Instead, we mark them X in the figures.

In order to see the detail of the new lines, we can zoom in and check the wavelength region around the new lines, as shown in Figure D.8. The energy shift of these two lines matches the typical nitrogen momentum conserving phonon replica energy of 3C SiC. Unfortunately we cannot see the new lines coming out on the next three nitrogen phonon replicas in Figure D.7 (b).

However if we look carefully we can see that there are shoulders on the left side of those nitrogen phonon replica lines, especially on the left side of the N-LO(X) peak. The phonon replica lines from the possible phosphorus bound exciton may be just buried under the nitrogen phonon replica lines.

In a paper published by A. Henry et al. [68], the authors studied the phosphorus doping in SiC and one of the samples was a 3C SiC epitaxial film on 6H SiC substrate. They observed very sharp LTPL no phonon line and phonon replica lines which are shifted to the low energy side by 1 meV from the well-studied nitrogen lines. The authors did not give the doping concentration of the sample they measured.

From all the work done on the other SiC polytypes, we have found that phosphorus is a shallower donor than nitrogen. The no phonon line(s) from the phosphorus dopant should appear at the higher energy side of the nitrogen no phonon line(s), which is exactly what we observed in our experiments, as shown in Figure D.7. Therefore, our understanding of the spectrum published in the Ref. [68] is those PL lines are probably still from nitrogen bound excitons, not from the phosphorus bound excitons. The fact that it is shifted to the lower energy side instead of the higher energy side makes us believe that that is from the stress between the 3C SiC epitaxial film and the 6H SiC substrate. S. Bai et al. has done a systematic study on the LTPL dependence on the stress between the 3C SiC epitaxial film and the Si (001) substrate and found out that the stress shift is towards the lower energy [70]. Similar work on the stress shift was done earlier by W. J. Choyke et al. and showed the similar shift towards the low energy direction [71].

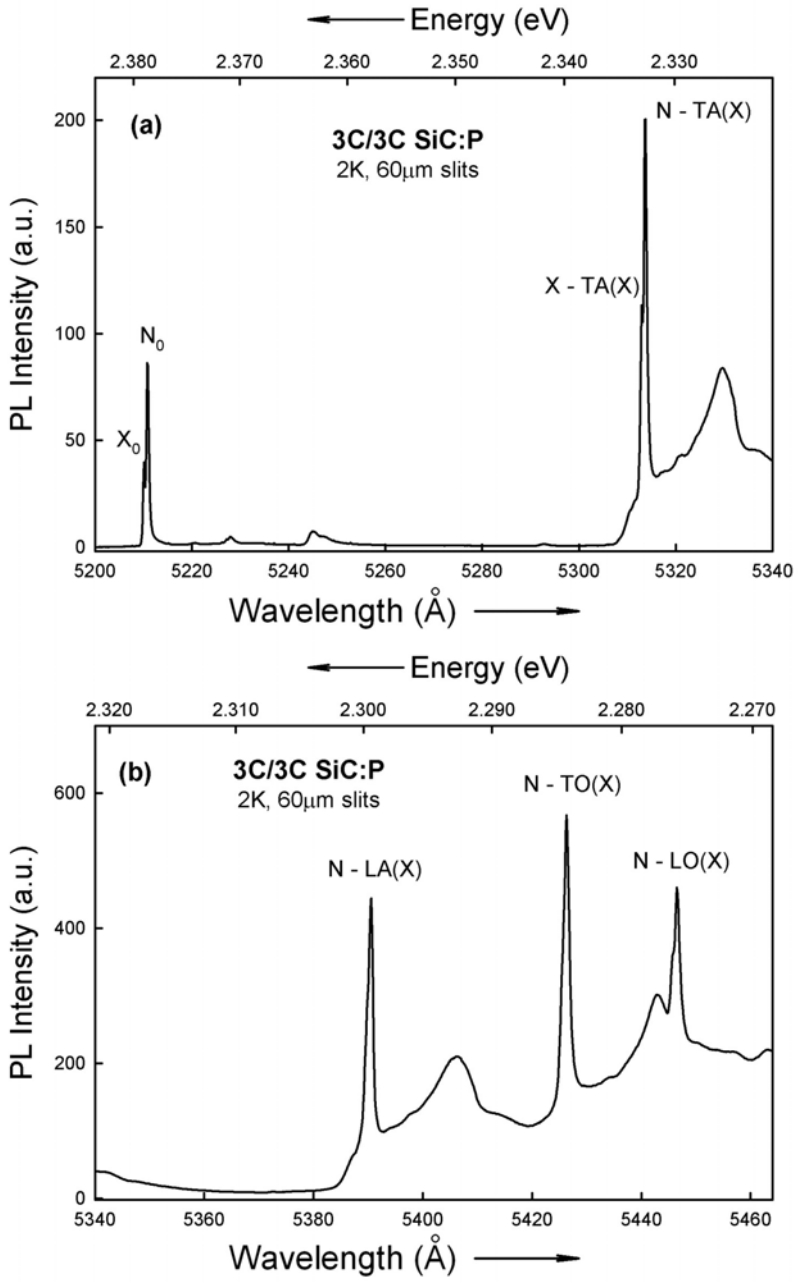

Figure D.7 LTPL spectra of 3C/3C SiC doped with phosphorus and nitrogen at 2K. (a) N_0 and N_0 – TA(X) are the no-phonon line and one of the phonon replicas line from the nitrogen bound exciton. X_0 and X_0 – TA(X) are the no-phonon line and one of the phonon replicas line possibly from the phosphorus bound exciton. (b) The other three of the four major phonon replicas from the nitrogen bound exciton are clearly seen here. But those possibly from phosphorus turn out to be shoulders on the left side of the nitrogen phonon replica lines.

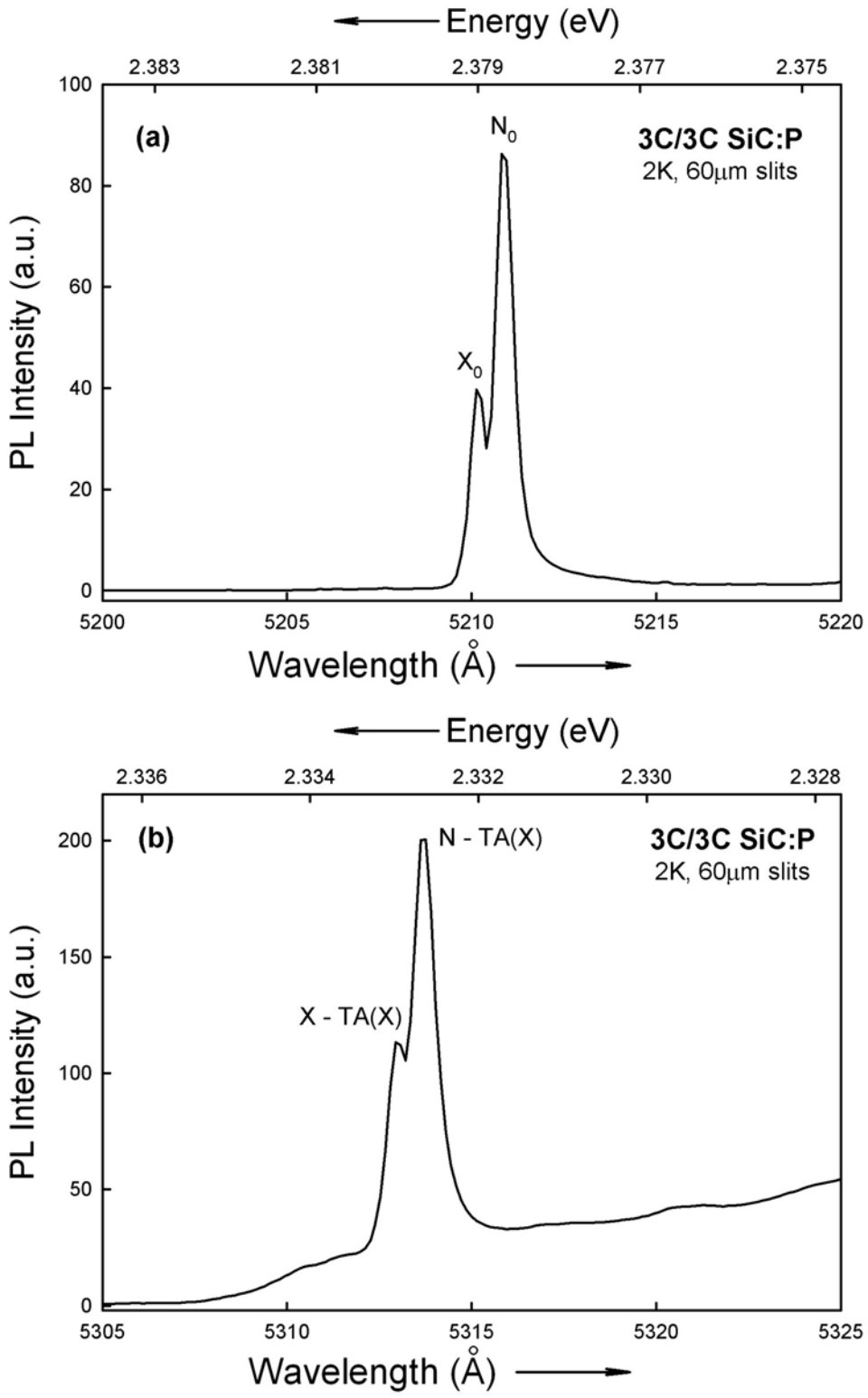

Figure D.8 Expanded view of two of the putative phosphorus lines in Figure 2.8. (a) Region around the X_0 line. (b) Region around the line X_0 – TA(X).

APPENDIX E

ULTRA-PRECISION MACHINING OF STAINLESS STEEL AND NICKEL WITH SINGLE CRYSTAL 4H AND 6H BOULE SILICON CARBIDE

E.1 INTRODUCTION

Ultra-precision machining has advanced significantly over the last several decades with improvements in design, computer control, and precision measurements, but the cutting tool of choice has remained unchanged; it is single-crystal natural diamond. Despite the exceptional mechanical properties of diamond, its chemical properties have inhibited the extension of ultra-precision machining to iron-containing (ferrous) or nickel alloys.

The workhorse of ultra-precision machining is the ultra-precision lathe (UPL). When used with a single-crystal diamond cutting tool, the machining process is known as single point diamond turning (SPDT). We use a Moore Nanotech 250 UPL, which uses hydrostatic oil-bearing slides and an air-bearing spindle to eliminate mechanical contact between its moving parts (see Figure E.1). The spindle motor is brushless and the slides are coupled magnetically with linear motors to avoid mechanical drive mechanisms which could introduce jitter. This UPL can be programmed with a resolution of 1 nm, can routinely cut surfaces to a local surface roughness of 1 to 2 nm in select materials, and can cut a large area to within tens of nm of the

programmed dimensions. This remarkable precision is a result of constant measurement of the slide positions by glass scales (resolution 34 pm) and feedback to the linear motors. Single crystal diamonds are used as cutting tools because of their hardness, strength, and high thermal conductivity. These properties contribute to the ability of a diamond to hold a precision, polished cutting edge and to carry away the heat generated during the cutting process.

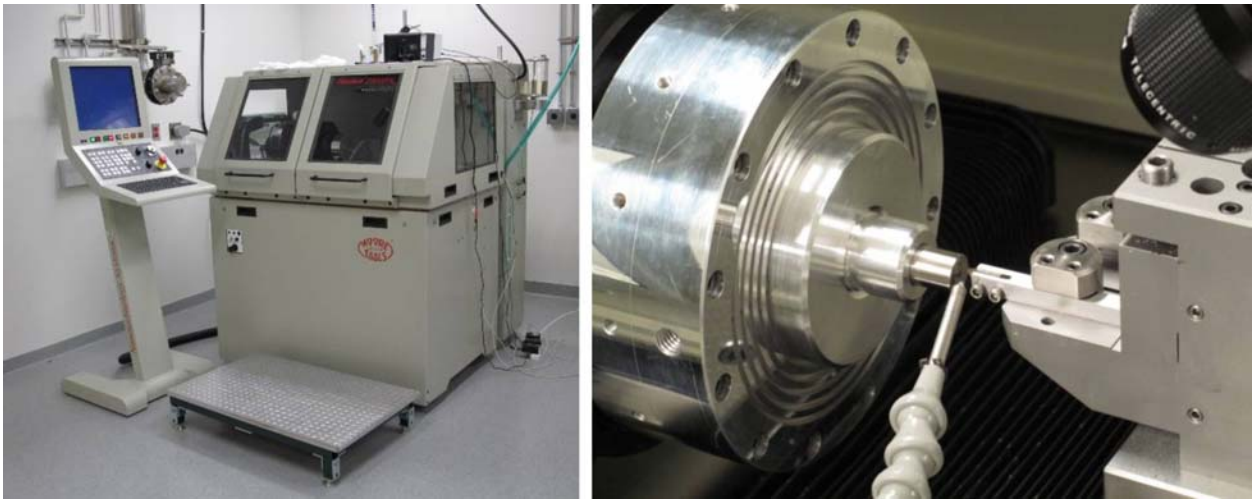

Figure E.1 (left) Moore Nanotech 250 UPL, an ultra-precision, computer-controlled lathe. (right) The SiC cutting tool in the ultra-precision lathe with a stainless steel sample mounted on the spindle and a nozzle for spraying a coolant mist.

Materials that are commonly cut with SPDT include non-ferrous metals (e.g. aluminum, copper, brass, silver), polymers (e.g. polymethylmethacrylate, polystyrene), and even some hard crystals (e.g. zinc sulfide, zinc selenide, germanium, silicon). For low surface roughness, the cutting must occur in the ductile regime. This may require very careful choices of cutting parameters, but it has been shown that it is even possible to cut SiC with SPDT [72]. Some materials cause unacceptably rapid diamond tool wear due to their hardness (mechanical wear) or due to chemical reactions involving the diamond tip and the surface being cut at the tip of the

tool (chemical wear). Wear on the cutting edge is exacerbated by the possibility of large forces and high temperatures at the cutting edge.

Ferrous alloys include some of the highest-performance metals available, but they are particularly problematic for SPDT. Chemical reactions involving the diamond tool and iron rapidly wear the cutting edge, making SPDT of steels and other ferrous alloys impractical. Many potential solutions to this problem have been explored, including cooling with liquid nitrogen, coating the diamond with wear-resistant layers, ultrasonic vibration of the tool tip, or cutting in an inert atmosphere. While some of these techniques help to decrease tool wear, none has yet proven practical [73]. Nickel alloys have similar problems. While electroless nickel can be successfully cut with SPDT, standard nickel alloys lead to unacceptably fast diamond tool wear.

E.2 EXPERIMENTS

Motivated by the similarities of single-crystal SiC to diamond in hardness and thermal conductivity, but noting the increased chemical stability compared to diamond, we sharpened ultra-pure single-crystal boule SiC into cutting tools for ultra-precision machining. High quality, low doped, boule grown SiC is expected to have an equivalent thermal conductivity to that of the type of diamonds currently used for ultra-precision machining. In addition, low defect single crystal SiC should be superior to any of the varieties of polycrystalline SiC materials currently available.

We fabricated the first SiC tool (shown in Figure E.2) from a 2.5 x 2.9 mm^2 strip of single crystal 6H SiC cut from a basal plane slice of n-type 6H SiC doped to 5 x 10^{15} cm^{-3}. The front of the 6H SiC tool was cut to about a 10º angle from the vertical axis. Side bevels were

fabricated with a diamond loaded abrasive Dremel Tool prior to polishing. The two surfaces that intersect to make up the cutting edge were polished with 30, 15, 6, 3, 1 and 1/2 μm diamond paste. The back end of the single crystal 6H SiC tool was held in a specially fabricated steel holder. A second tool was made in a similar fashion out of single crystal 4H SiC, but instead of sharp corners, it has a large (20 mm radius of curvature) cutting edge for a wider and potentially smoother cut (also shown in Figure E.2). A cutting tool with this shape is known as a radius tool.

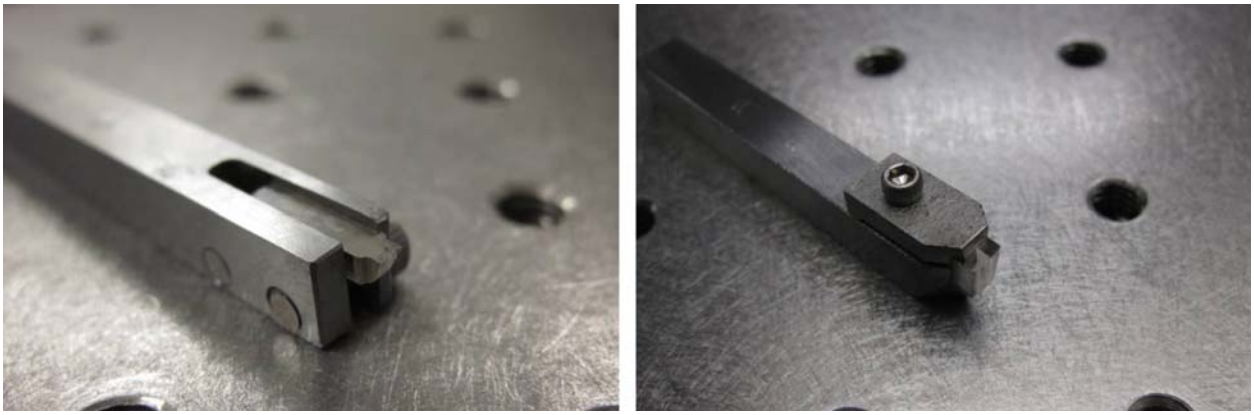

Figure E.2 (left) A sharp-cornered SiC cutting tool utilizing a single crystal of 6H SiC polished to a sharp cutting edge, mounted in a steel holder and shank. (right) A similar tool using single crystal 4H SiC polished to a sharp edge with a large circular radius, also mechanically mounted in a steel holder.

As a first test, we cut a flat surface on the end of a 12.7 mm diameter, 316 stainless steel rod in our UPL with our sharp-cornered 6H SiC cutting tool. The spindle speed was 2000 rpm, with a feed rate of 1 μm per revolution and a 4 μm depth of cut. The SiC crystal and stainless steel surface were cooled with a sprayed mist of odorless mineral spirits (OMS) and compressed air, which also serves to clear off the chips of material as it is cut. We then changed to our large radius 4H SiC cutting tool, and cut several more surfaces on 316 stainless steel rods. The cuts were generally lighter to keep the cutting forces low despite the much larger cutting surface of

the large radius tool. We started with a surface cut at a spindle speed of 2000 rpm, a feed rate of 1 μm per revolution and a 1 μm depth of cut. We then cut additional surfaces while tripling the feed rate to 3 μm per revolution and maintaining a 1 μm depth of cut, or tripling the depth of cut to 3 μm and maintaining a feed rate of 1 μm per revolution. We then repeated the last cut, with a depth of cut of 3 μm and a feed rate of 1 μm per revolution on a nickel rod.

E.3 RESULTS AND DISCUSSION

From the first attempts to cut 316 stainless steel with the sharp-cornered 6H SiC tool, we found that the sharp single-crystal 6H SiC tool could cut a smooth, mirror like finish on a 316 stainless steel rod. Compared to the finish from cutting with a high-speed steel tool on a conventional lathe, the SiC tool on the UPL gave impressive results (see Figure E.3), with no indication of wear after several cuts across the surface. Furthermore, we saw no significant difference in the quality of finish on stainless steel compared to aluminum with the 6H SiC tool. We do not have a direct comparison to a diamond tool because the test would almost surely destroy the costly diamond tool.

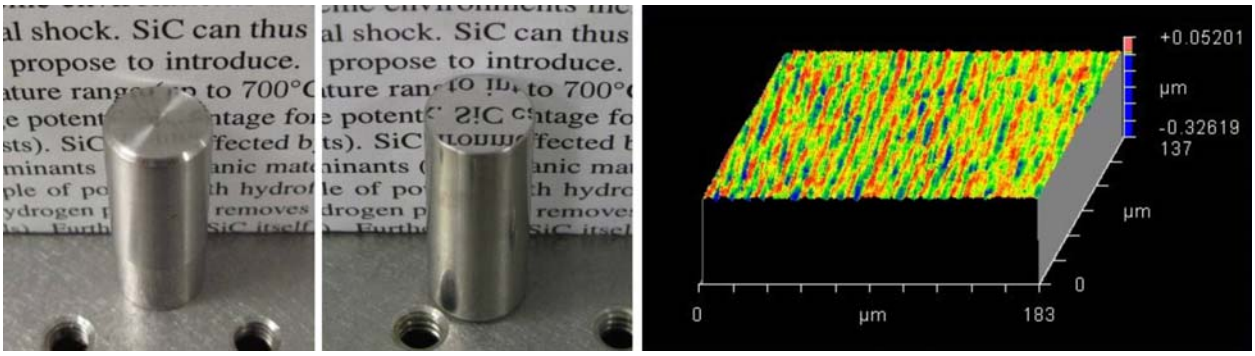

Figure E.3 (left) 316 stainless steel cylinder end cut with a high-speed steel tool on a conventional lathe. (center) 316 stainless steel cylinder end cut with the sharp-cornered single-crystal 6H SiC tool on an ultra-precision lathe. The difference in reflectivity as a result of the difference in surface roughness is clearly visible. (right) Surface map of the sample shown in the center measured with a Zygo interferometer.

The most common metric for quantifying surface roughness is the average surface roughness (Ra), defined to be the average distance between the measured surface and the mean plane. A quantitative analysis of the 6H SiC-cut 316 stainless steel surface with a Zygo interferometer shows why the surface is so reflective: the Ra is approximately 3 nm in the smoothest areas. A map of a small region of the surface is shown in Figure E.3. The grooves from the spiral cutting pattern, while very low in amplitude, are clearly visible as slightly curved lines.

An analysis of the roughness of the surfaces cut with the large radius single-crystal 4H SiC tool showed similar, although slightly rougher, results. The surfaces cut at 2000 rpm with a feed rate of 1 µm per revolution and a depth of cut of 1 µm or 3 µm had Ra of 5 nm to 6 nm in the smoothest regions, while the surface cut with a feed rate of 3 µm per revolution and a depth of cut of 1 µm had Ra of 8 nm in the smoothest regions. The surface of the nickel rod, cut with a feed rate of 1 µm per revolution and a depth of cut of 3 µm also had Ra of 6 nm in the smoothest

regions. The maps of small regions of two of the surfaces cut with the large radius 4H SiC tool are shown in Figure E.4.

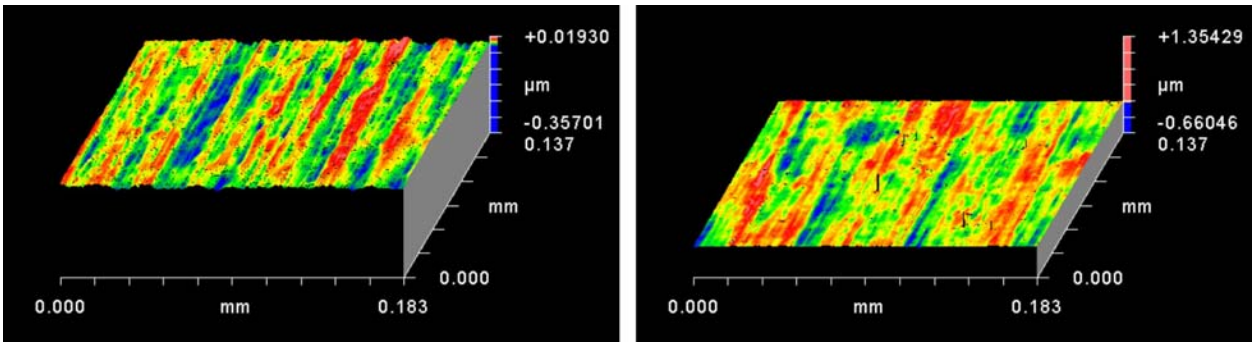

Figure E.4 (left) Surface map of a portion of the end of a 316 stainless steel cylinder cut with the large radius single-crystal 4H SiC cutting tool. (right) Surface map of a portion of the end of a nickel cylinder cut with the large radius 4H SiC single-crystal cutting tool.

The surfaces cut with the large radius tool show less defined grooves, as expected with a much rounder ended tool. However, there is notable increased roughness, likely due to vibrations of the tool or sample induced by the larger cutting forces produced while cutting a wider band on each pass with the large radius tool. It may be possible to reduce these vibrations with careful choice of cutting speeds and feed rates, as is commonly needed in conventional machining of stainless steel. Alternatively, a smaller radius tool should decrease the cutting forces, although a smaller radius tool generally requires a slower feed rate to avoid excessive grooving of the surface.

E.4 CONCLUSION

We have shown that high purity 4H and 6H single-crystal boule SiC ground and polished to a sharp edge has the potential to be an alternative cutting tool for ultra-precision machining, particularly for materials such as stainless steel and nickel, where diamond wears excessively rapidly. We showed that surfaces with average roughness down to 3 nm can be achieved on 316 stainless steel with a single-crystal 6H SiC cutting tool in an ultra-precision lathe. Furthermore, the potential advantages of single-crystal SiC cutting tools over diamond extend beyond ferrous and nickel alloys. If the cutting performance on other materials is even comparable to natural diamond, the cost, available crystal size, and purity of synthetic single-crystal SiC could make it the preferred cutting tool material of the future for ultra-precision machining of a wide range of materials.

Acknowledgments. For this particular project, we wish to thank Dr. Brian D'Urso for his collaboration on his diamond turning machine, and G. Davis, J. Odenski and A. P. Hedges of the II-VI Corp. for very helpful discussions and performing the Zygo interferometer measurements. We also wish to express our gratitude to K. Petrocelly of our Physics Department for mechanical designs and expert machining.

BIBLIOGRAPHY

[1] Y. S. Park, R. K. Willardson, and E. R. Weber, *SiC Materials and Devices* (Academic Press, 1998), Vol. 52.

[2] L. L. Clemen, M. Yoganathan, W. J. Choyke, R. P. Devaty, H. S. Kong, J. A. Edmond, D. J. Larkin, J. A. Powell, and A. A. Burk, Jr., Inst. Phys. Conf. Ser. No. **137**, 251 (1994).

[3] A. Henry, O. Kordina, C. Hallin, C. Hemmingsson, and E. Janzén, Appl. Phys. Lett. **65**, 2457 (1994).

[4] I. G. Ivanov, C. Hallin, A. Henry, O. Kordina, and E. Janzén, J. Appl. Phys. **80**, 3504 (1996).

[5] A. Henry, U. Forsberg, M. K. Linnarsson, and E. Janzén, Phys. Scr. **72**, 254 (2005).

[6] J. Camassel, S. Juillaguet, M. Zielinski, and C. Balloud, Chem. Vap. Deposition **12**, 549 (2006).

[7] L. L. Clemen, R. P. Devaty, M. F. Macmillan, M. Yoganathan, W. J. Choyke, D. J. Larkin, J. A. Powell, J. A. Edmond, and H. S. Kong, Appl. Phys. Lett. **62**, 2953 (1993).

[8] W. J. Choyke and L. Patrick, Phys. Rev. B **2**, 4959 (1970).

[9] I. G. Ivanov, B. Magnusson, and E. Janzén, Phys. Rev. B **67**, 165211 (2003).

[10] M. Bockstedte, A. Gali, A. Mattausch, O. Pankratov, and J. W. Steeds, phys. stat. sol. (b) **245**, 1281 (2008).

[11] J. W. Steeds, W. Sullivan, S. A. Furkert, G. A. Evans, and P. J. Wellmann, Phys. Rev. B **77**, 195203 (2008).

[12] J. W. Steeds and W. Sullivan, Phys. Rev. B **77**, 195204 (2008).

[13] A. Gali, P. Deák, P. Ordejón, N. T. Son, E. Janzén, and W. J. Choyke, Phys. Rev. B **68**, 125201 (2003).

[14] A. Mattausch, M. Bockstedte, and O. Pankratov, Phys. Rev. B **70**, 235211 (2004).

[15] A. Mattausch, M. Bockstedte, and O. Pankratov, Phys. Rev. B **69**, 045322 (2004).

[16] S. A. Solin and A. K. Ramdas, Phys. Rev. B **1**, 1687 (1970).

[17] W. J. Choyke and L. Patrick, Phys. Rev. B **4**, 1843 (1971).

[18] L. Patrick and W. J. Choyke, Phys. Rev. B **5**, 3253 (1972).

[19] W. J. Choyke and L. Patrick, Inst. Phys. Conf. Ser. No. **16**, 218 (1972).

[20] L. Patrick and W. J. Choyke, J. Phys. Chem. Solids **34**, 565 (1973).

[21] S. G. Sridhara, D. G. Nizhner, R. P. Devaty, W. J. Choyke, T. Dalibor, G. Pensl, and T. Kimoto, Mater. Sci. Forum **264-268**, 493 (1998).

[22] A. Gali, P. Deák, E. Rauls, N. T. Son, I. G. Ivanov, F. H. C. Carlsson, E. Janzén, and W. J. Choyke, Phys. Rev. B **67**, 155203 (2003).

[23] A. Gali, P. Deák, E. Rauls, N. T. Son, I. G. Ivanov, F. H. C. Carlsson, E. Janzén, and W. J. Choyke, Physica B **340**, 175 (2003).

[24] G. Pensl and W. J. Choyke, Physica B **185**, 264 (1993).

[25] T. Kimoto, A. Itoh, H. Matsunami, S. Sridhara, L. L. Clemen, R. P. Devaty, W. J. Choyke, T. Dalibor, C. Peppermuller, and G. Pensl, Appl. Phys. Lett. **67**, 2833 (1995).

[26] T. Dalibor, C. Peppermüller, G. Pensl, S. Sridhara, R. P. Devaty, W. J. Choyke, A. Itoh, T. Kimoto, and H. Matsunami, Inst. Phys. Conf. Ser. No. **142**, 517 (1996).

[27] T. Dalibor, G. Pensl, H. Matsunami, T. Kimoto, W. J. Choyke, A. Schöner, and N. Nordell, phys. stat. sol. (a) **162**, 199 (1997).

[28] T. Dalibor, G. Pensl, T. Kimoto, H. Matsunami, S. Sridhara, R. P. Devaty, and W. J. Choyke, Diam. Relat. Mat. **6**, 1333 (1997).

[29] T. Egilsson, J. P. Bergman, I. G. Ivanov, A. Henry, and E. Janzén, Phys. Rev. B **59**, 1956 (1999).

[30] L. Storasta, F. H. C. Carlsson, S. G. Sridhara, J. P. Bergman, A. Henry, T. Egilsson, A. Hallén, and E. Janzén, Appl. Phys. Lett. **78**, 46 (2001).

[31] T. A. G. Eberlein, C. J. Fall, R. Jones, P. R. Briddon, and S. Öberg, Phys. Rev. B **65**, 184108 (2002).

[32] J. Zhang, L. Storasta, J. P. Bergman, N. T. Son, and E. Janzen, J. Appl. Phys. **93**, 4708 (2003).

[33] M. V. B. Pinheiro, E. Rauls, U. Gerstmann, S. Greulich-Weber, H. Overhof, and J. M. Spaeth, Phys. Rev. B **70**, 245204 (2004).

[34] T. A. G. Eberlein, R. Jones, S. Oberg, and P. R. Briddon, Phys. Rev. B **74**, 144106 (2006).

[35] J. W. Steeds, F. Carosella, G. A. Evans, M. M. Ismail, L. R. Danks, and W. Voegeli, Mater. Sci. Forum **353-356**, 381 (2001).

[36] H. J. von Bardeleben, J. L. Cantin, L. Henry, and M. F. Barthe, Phys. Rev. B **62**, 10841 (2000).

[37] D. Drouin, A. R. Couture, D. Joly, X. Tastet, V. Aimez, and R. Gauvin, Scanning **29**, 92 (2007).

[38] S. G. Sridhara, T. J. Eperjesi, R. P. Devaty, and W. J. Choyke, Mater. Sci. Eng., B **61-62**, 229 (1999).

[39] M. Yoganathan, W. Suttrop, R. P. Devaty, and W. J. Choyke, J. Appl. Cryst. **27**, 497 (1994).

[40] D. V. Lang, J. Appl. Phys. **45**, 3023 (1974).

[41] D. K. Schroder, *Semiconductor Material and Device Characterization* (Wiley-IEEE Press, 2006).

[42] P. M. Morse, Phys. Rev. **34**, 57 (1929).

[43] W. B. Fowler, R. Capelletti, and E. Colombi, Phys. Rev. B **44**, 2961 (1991).

[44] W. J. Choyke, R. P. Devaty, S. Bai, A. Gali, P. Deák, and G. Pensl, Mater. Sci. Forum **389-393**, 585 (2002).

[45] S. Bai, F. Yan, R. P. Devaty, W. J. Choyke, R. Grotzschel, G. Wagner, and M. F. MacMillan, Mater. Sci. Forum **457-460**, 589 (2004).

[46] T. Pang, *An Introduction to Computational Physics, 2nd Edition* (Cambridge University Press, 2006).

[47] N. Zettili, *Quantum Mechanics: Concepts and Applications, 2nd Edition* (John Wiley & Sons, Inc., 2009).

[48] K. Hölzlein, G. Pensl, M. Schulz, and P. Stolz, Review of Scientific Instruments **57**, 1373 (1986).

[49] M. Bockstedte, A. Kley, J. Neugebauer, and M. Scheffler, Comput. Phys. Commun. **107**, 187 (1997).

[50] W. J. Choyke, M. Yoganathan, and C. Carter, Jr., in *Amorphous and Crystalline Silicon Carbide III and Other Group IV-IV materials, ICACSC'90*, edited by G. Harris, M. C. Spencer, and C. Y.-W. Yang (Springer, New York, 1993), pp. 165.

[51] W. J. Choyke, D. R. Hamilton, and L. Patrick, Phys. Rev. **133**, A1163 (1964).

[52] Y. P. Varshni, Physica **34**, 149 (1967).

[53] K. P. O' Donnell and X. Chen, Appl. Phys. Lett. **58**, 2924 (1991).

[54] D. Bimberg, M. Altarelli, and N. O. Lipari, Solid State Communications **40**, 437 (1981).

[55] S. G. Sridhara, F. H. C. Carlsson, J. P. Bergman, A. Henry, and E. Janzén, Mater. Sci. Forum **353-356**, 377 (2001).

[56] A. Henry, T. Egilsson, I. G. Ivanov, C. I. Harris, S. Savage, and E. Janzén, Mater. Sci. Forum **264-268**, 497 (1998).

[57] P. J. Dean, D. Bimberg, and W. J. Choyke, Inst. Phys. Conf. Ser. No. **46**, 447 (1979).

[58] P. J. Dean and R. L. Hartman, Phys. Rev. B **5**, 4911 (1972).

[59] R. P. Devaty, W. J. Choyke, S. G. Sridhara, and L. L. Clemen, Mater. Sci. Eng. B **61-62**, 187 (1999).

[60] D. J. Larkin, P. G. Neudeck, J. A. Powell, and L. G. Matus, Appl. Phys. Lett. **65**, 1659 (1994).

[61] D. J. Larkin, P. G. Neudeck, J. A. Powell, and L. G. Matus, Inst. Phys. Conf. Ser. No. **137**, 51 (1994).

[62] D. J. Larkin, phys. stat. sol. (b) **202**, 305 (1997).

[63] S. G. Sridhara, L. L. Clemen, D. G. Nizhner, R. P. Devaty, W. J. Choyke, and D. J. Larkin, Mater. Sci. Forum **264-268**, 465 (1998).

[64] J. Isoya, M. Katagiri, T. Umeda, N. T. Son, A. Henry, A. Gali, N. Morishita, T. Ohshima, H. Itoh, and E. Janzén, Mater. Sci. Forum **527-529** (2006).

[65] R. Wang, I. B. Bhat, and T. P. Chow, J. Appl. Phys. **92**, 7587 (2002).

[66] T. Hornos, A. Gali, R. P. Devaty, and W. J. Choyke, Appl. Phys. Lett. **87**, 212114 (2005).

[67] T. Hornos, A. Gali, R. P. Devaty, and W. J. Choyke, Mater. Sci. Forum **527-529**, 605 (2006).

[68] A. Henry and E. Janzén, Mater. Sci. Forum **527-529** (2006).

[69] L. Patrick, D. R. Hamilton, and W. J. Choyke, Phys. Rev. **132**, 2023 (1963).

[70] S. Bai, Y. Ke, Y. Shishkin, O. Shigiltchoff, R. P. Devaty, W. J. Choyke, D. Strauch, B. Stojetz, B. Dorner, D. Hobgood, J. Serrano, M. Cardona, H. Nagasawa, T. Kimoto, and L. M. Porter, Mater. Res. Soc. Symp. Proc. **742**, 151 (2003).

[71] W. J. Choyke, Z. C. Feng, and J. A. Powell, J. Appl. Phys. **64**, 3163 (1988).

[72] J. Patten, W. Gao, and K. Yasuto, J. Manuf. Sci. Eng. **127**, 522 (2005).

[73] E. Brinksmeier and R. Gläbe, CIRP Annals - Manufacturing Technology **50**, 385 (2001).